Average Heat Flux Measurements in an Additively Manufactured Rotating Detonation Rocket Engine Calorimeter

Matthew Aaron Maybee

A THESIS

Submitted in partial fulfillment of the requirements
for the degree of Master of Science
in
The Department of Mechanical and Aerospace Engineering
to
The Graduate School
of
The University of Alabama in Huntsville

May 2025

Approved by:

Dr. John W. Bennewitz, Research Advisor
Dr. John W. Bennewitz, Committee Chair
Dr. John W. Bennewitz, Committee Member
Dr. Kunning G. Xu, Committee Member
Dr. David M. Lineberry, Committee Member
Dr. George Nelson, Department Chair
Dr. Shankar Mahalingam, College Dean
Dr. Michael D. Anderson, Graduate Dean

Abstract

Average Heat Flux Measurements in an Additively Manufactured Rotating Detonation Rocket Engine Calorimeter

Matthew Aaron Maybee

A thesis submitted in partial fulfillment of the requirements for the degree of Master of Science

Mechanical and Aerospace Engineering

The University of Alabama in Huntsville
May 2025

Rotating detonation rocket engines (RDREs) offer benefits over traditional deflagrative engines, including increased engine performance, compact combustion and negligible detrimental thermoacoustic instabilities due to mode-locking. Realizing the benefits of a detonation-based propulsion system will be accompanied by increased thermal loads due to a combination of heat release at elevated pressure and temperature, as well as compact heat release due to detonation. Managing these heat loads necessitates the development of thermal management strategies. As a first step towards establishing the requirements for detonation-based engine thermal management strategies, this work develops an additively manufactured (AM) water-based, axially resolved calorimeter for integration in an existing 76.8 mm outer diameter (OD) RDRE to measure average chamber heat flux. In particular, the calorimetry outer body provides average heat flux data via circumferential channels at nine axial stations to axially resolve the heat flux distribution on the chamber outer wall. The average heat flux is found to be $6.6 - 16.3$ MW/m^2 for a straight annulus and $11.4 - 20.5$ MW/m^2 for a constricted annular configuration which exhibited maximum

heat flux at the throat. By quantifying the axial distribution of heat flux, this work seeks to support the development of thermal management systems for long duration firing of detonation-based devices.

Acknowledgements

The decision to get a graduate degree has proven to be more valuable than I could have possibly been aware of at the time of making that decision. This is due in large part to the many individuals to whom I am indebted to for their investment in not only this work, but in me as an engineer, a student, and a person.

No greater investment across all of these areas has been made than that of my advisor, Dr. John Bennewitz. From the time when the laboratory was a storage closet until now, he has continually supported, encouraged, and challenged me. I would like to particularly thank him for being genuinely invested in my development. I greatly appreciate his unrelenting generosity in providing me with opportunities I wouldn't be privileged to otherwise. Without a mentor to push me as hard as he has, there is no doubt in my mind that I wouldn't be the student, engineer, or person that I am today.

I would like to acknowledge the sponsor of this work, the National Aeronautics and Space Administration (NASA) Marshall Spaceflight Center (MSFC) under NASA CAN grant 80NSSC24M0062. In particular, I would like to thank Tom Teasley at NASA Marshall Space Flight Center for his guidance throughout the entirety of this project.

I would like to acknowledge the invaluable support provided by Dr. David Lineberry throughout the entirety of my time at the Propulsion Research Center. Since my time in his senior design class, he has been a consistent mentor. I would like to thank him for his willingness to troubleshoot any and all problems I create with unwavering patience, as well as providing the necessary experimental support to complete this work.

I would like to thank my committee member, Dr. Xu, for his recommendations on this work. Likewise, I would like to acknowledge Micheala Hemming for the original design of the RDRE used for this work as well as her willingness to help and provide pertinent information throughout this project.

I would like to express gratitude for the work done by Tony Hall at the PRC. I would like to thank him not only for the wide range of help he provides but also for being willing to teach me the ins and outs of propulsion testing. Tony has generously supplied me with everything from a bicycle to garden hoses, which I greatly appreciate.

I would also like to acknowledge Joseph Hernandez-McCloskey at the University of Texas San Antonio for his assistance with familiarizing me with both additive manufacturing and RDRE calorimetry. This work wouldn't have been completed without the experience he so willingly shared with me.

Acknowledgments would be incomplete if only mentioning those who helped with this particular thesis work. I also want to relay my thankfulness for those who have invested in my development throughout my time as a graduate student. I would like to thank the members of the combustion devices branch at the Air Force Research Laboratory for their support of our research group. I would like to give a special thanks to Dr. Jason Burr for his support, not only the time I spent interning under his mentorship, but also through his continual collaboration with our research group. Dr. Burr has never withheld encouragement, advice, or intuitive explanations of complex ideas, for which I am greatly appreciative of.

Also, much thanks to the graduate members of APECSLab, Justin Byers, Raj Dave, and Garrett Cobb, as well as the undergraduates, Khlood Yafai, Angelou Panettieri., Noah Hudson, McClellen Buckhalter, and Hunter Wilson. The environment of constant learning and support, as well as being a fun group to work with, is appreciated. I would like to acknowledge the large portion of this work that has had

the hands of Kaito Durkee involved in some capacity. Despite being a fellow student, I have learned greatly from him and am thankful for his constant willingness to help.

I would like to thank my family for their support and patience throughout my time as a graduate student. I wouldn't have been able to do any of this without the love and values instilled in me from my mom and dad. I would also like to thank my two sisters, Sarah Marlin and Ally Maybee for their support. I would like to thank Georgia Ivy Maybee for the numerous times she allowed me to practice presentations despite not always being thrilled about it.

Lastly, it is necessary to show gratitude to my fiancé, Anna Fay Renshaw. It is because of her that I am able to have the patience and determination required to complete this work. I would like to thank her for actively listening, asking questions, and offering solutions whenever I complain to her about challenges I faced. Thank you for helping me to become the best person I can be. I love you Anna, and can't wait to see what challenges we can overcome together in the future.

Table of Contents

Abstract . . . . . **ii**

Acknowledgements . . . . . **v**

Table of Contents . . . . . **xi**

List of Figures . . . . . **xii**

List of Tables . . . . . **xviii**

List of Symbols . . . . . **xix**

1 Introduction **1**

1.1 Forward 1

1.2 Detonation For Propulsion 1

1.3 Heat Transfer Measurements in RDRE 5

2 Background Concepts **8**

2.1 Chapman-Jouguet Theory 8

2.2 ZND Model 13

2.3 Cycle Analysis 13

2.4 Calorimetry 17

2.5 Constant Pressure Engine Heat Transfer 19

2.6 Additive Manufacturing 21

3 Engine Design 23

3.1 Heat-Sink Hardware 24

3.1.1 Outer Body 25

3.1.2 Inner Body 25

3.1.3 Propellant Manifold 26

3.2 Calorimetry Outer Body 26

3.2.1 Channel Sizing 28

3.2.2 Internal Channel Geometry 32

3.2.3 CTAP Routing 33

3.3 Flow System Design 34

4 Experimental Setup and Testing 38

4.1 Water Calibration 38

4.1.1 Experimental Setup 38

4.1.2 Calibration Flow System 39

4.1.3 Flow Calibration Results 41

4.2 Engine Hot Fire 44
4.2.1 Experimental Setup 45
4.2.2 Propellant Flow System 46
4.2.3 Coolant Flow System 47
4.2.4 Optics 49

5 Data Reduction 51

5.1 Propellant Mass Flow Rate 51
5.2 Coolant Mass Flow Rate 53
5.3 Heat Flux 54
5.4 Wave Dynamics 57
5.5 Uncertainty Analysis 59
5.5.1 Pressure Measurement Uncertainty 62
5.5.2 Temperature Uncertainty 64
5.5.3 Propellant Discharge Coefficient Uncertainty 65
5.5.4 Propellant Mass Flow Rate Uncertainty 67
5.5.5 Equivalence Ratio and Total Mass Flux Uncertainty . . 68
5.5.6 Coolant Discharge Coefficient Uncertainty 69
5.5.7 Coolant Mass Flow Rate Uncertainty 72
5.5.8 Heat Flux Uncertainty 74

6 Results **76**

6.1 Heat Flux 79

6.1.1 Straight Center Body Configuration 80

6.1.2 Constricted Center Body Configuration 81

6.1.3 Heat Flux Scaling 83

6.2 Chamber Pressure 86

6.3 Wave Dynamics 86

7 Conclusions **90**

References **91**

Appendix A: Test Data **107**

Appendix B: Heat Flux Varying Mass Flux **124**

Appendix C: Water Flow Calibration Data **126**

Appendix D: Test Conditions Summary **129**

List of Figures

1.1 Schematic of a detonation driven ramjet. 3

1.2 (a) PDE operation stages and (b) PDE demonstration flight. . . . 3

1.3 Schematic of RDRE with (a) cut view of RDRE revealing detonation front and (b) unwrapped detonation structure. 4

2.1 An idealized 1-D Chapman-Jouguet Detonation. 9

2.2 Rayleigh Lines and Hugoniot curves plotted in $p - \nu$ space. 12

2.3 Structure of the detonation wave as described in the ZND model. 14

2.4 Brayton cycle diagrams, (a) $T-s$ and (b) $p-\nu$. 15

2.5 Fickett-Jacobs model for detonation. 16

2.6 Fickett-Jacobs cycle comparison to the Brayton Cycle for methane-oxygen at $\phi = 1$. 17

2.7 Cup calorimetry experiment where water undergoes a process that results in a temperature difference between states (i) and (ii). . . 18

2.8 Rocket engine calorimetry experiment where water travels circumferentially around the combustion chamber to measure temperature difference between states (i) and (ii). 19

2.9 Schematic of L-PBF process. 22

3.1 Schematic of 76.8 mm RDRE configurations: (a) heat-sink straight channel, (b) water-cooled straight channel, and (c) water-cooled constricted geometry. 24

3.2 Exploded view of modular 76.8 mm RDRE with heat-sink outer body. 24

3.3 Center body configurations tested: (a) straight puck, (b) straight cone, and (c) constricted. 26

3.4 Propellant manifold cut view showing propellant plenums. 27

3.5 Calorimetry outer body axial stations in relation to the (a) straight center body and (b) constricted center body. 27

3.6 Propellant manifold cut view showing propellant plenums. 28

3.7 Coolant flow path with inlet (a) 180°, (b) 160°, and (c) 200° from coolant exit. 28

3.8 Schematic of internal channel dimensions. 32

3.9 Schematic of the internal cooling channels fluid volume for (a) whole device, and (b)-(d) detail view of CTAP channel routing viewed from each plane. 33

3.10 Initial GFSSP model of coolant flow path used for initial orifice sizing (Model 1). 35

3.11 Second GFSSP model to incorporate experimentally measured resistances (Model 2). 36

3.12 Pressure throughout coolant delivery system at (1) tank, (2) downstream of hardware, and (3) atmosphere. 37

4.1 Simplified plumbing and instrumentation diagram for the water calibration flow system. 39

4.2 Image of (a) calibration water supply plumbing and (b) calibration testing setup. 40

4.3 Full flow test of calorimeter during calibration testing. 41

4.4 Mass flow rate data for station 1. 43

4.5 Experimental test cell setup with RDRE mounted to thrust stand and coolant water tank. 45

4.6 Generalized Plumbing and Instrumentation Diagram of propellant flow system. 46

4.7 Propellant plumbing (a) downstream of fire valves going into hardware and (b) mass flow metering plumbing upstream of fire valves. 47

4.8 Schematic of (a) generalized Plumbing and Instrumentation Diagram of coolant flow system and (b) detailed view of downstream plumbing and instrumentation. 48

4.9 RDRE, plumbing, and instrumentation for hot fire testing with (a) top-down view of oxygen (green), fuel (red), and coolant (blue) plumbing and (b) isometric view of hardware on test stand. 49

4.10 Optical diagnostics setup. 50

5.1 Coolant mass flow rate at each of the nine stations. 55

5.2 Schematic of (a) channel geometry control volume and (b) heat transfer model for determining chamber heat flux. 56

5.3 Image processing procedure with (a) raw image, (b) background subtraction, (c) cartesian mesh, (d) annulus circle fit, and (e) polar mesh. 58

5.4 Corresponding detonation surface. 58

6.1 Images of (a) RDRE hot-fire side view and (b) RDRE hot-fire top-down view. 76

6.2 Operational map for hot fire testing. 77

6.3 Coolant outlet (a) pressure response and (b) temperature response for $\psi = 241$ kg/m^2-s, $\phi = 1.1$ test. 78

6.4 Axial heat flux distribution for (a) $\phi = 1.1$ and $\psi = 103$ kg/m^2-s and (b) $\phi = 1.1$ and $\psi = 240$ kg/m^2-s for both straight and constricted center bodies. 80

6.5 Axial heat flux distributions for the mass flux sensitivity study using the straight center body geometry. 82

6.6 Axial heat flux distributions for the mass flux sensitivity study using the constricted center body geometries. 83

6.7 Heat flux with varying total mass flux for axial stations (a) two and (b) five. 84

6.8 Scaled heat flux for (a) $\alpha = 0.8$ and (b) $\alpha = 0.38$. 85

6.9 CTAP pressures for (a) all straight center body configuration tests and (b) a $\boldsymbol{\psi} = 241$ kg/m$^{\mathbf{2}}$-s, $\boldsymbol{\phi} = 1.1$ test. 86

6.10 Detonation surface plots for (a) +2/-2 wave mode observed at $\psi = 100 - 150$ kg/m^2-s and (b) +3/-3 wave mode observed at $\psi = 200 - 240$ kg/m^2-s. 87

6.11 Detonation surface plots for the -1 wave mode observed at $\psi = 100 - 240$ kg/m^2-s with the constricted center body geometry. . . 88

6.12 Constricted geometry test case at $\boldsymbol{\psi}$ = 279 kg/m$^{\mathbf{2}}$-s, exhibiting (a) temperature rise associated with a change in engine operating mode and (b) accompanying high speed images of wave dynamics. 89

A.1 Test 20241025-012 (a) axial heat flux, (b) thrust, (c) outlet pressure, (d) outlet temperature, (e) oxygen pressures, and (f) fuel pressures. 108

A.2 Test 20241028-006 (a) axial heat flux, (b) thrust, (c) outlet pressure, (d) outlet temperature, (e) oxygen pressures, and (f) fuel pressures. 109

A.3 Test 20241028-009 (a) axial heat flux, (b) thrust, (c) outlet pressure, (d) outlet temperature, (e) oxygen pressures, and (f) fuel pressures. 110

A.4 Test 20241028-010 (a) axial heat flux, (b) thrust, (c) outlet pressure, (d) outlet temperature, (e) oxygen pressures, and (f) fuel pressures. 111

A.5 Test 20241028-011 (a) axial heat flux, (b) thrust, (c) outlet pressure, (d) outlet temperature, (e) oxygen pressures, and (f) fuel pressures. 112

A.6 Test 20241029-015 (a) axial heat flux, (b) thrust, (c) outlet pressure, (d) outlet temperature, (e) oxygen pressures, and (f) fuel pressures. 113

A.7 Test 20241029-016 (a) axial heat flux, (b) thrust, (c) outlet pressure, (d) outlet temperature, (e) oxygen pressures, and (f) fuel pressures. 114

A.8 Test 20241029-017 (a) axial heat flux, (b) thrust, (c) outlet pressure, (d) outlet temperature, (e) oxygen pressures, and (f) fuel pressures. 115

A.9 Test 20241029-018 (a) axial heat flux, (b) thrust, (c) outlet pressure, (d) outlet temperature, (e) oxygen pressures, and (f) fuel pressures. 116

A.10 Test 20241029-019 (a) axial heat flux, (b) thrust, (c) outlet pressure, (d) outlet temperature, (e) oxygen pressures, and (f) fuel pressures. 117

A.11 Test 20241029-020 (a) axial heat flux, (b) thrust, (c) outlet pressure, (d) outlet temperature, (e) oxygen pressures, and (f) fuel pressures. 118

A.12 Test 20241029-021 (a) axial heat flux, (b) thrust, (c) outlet pressure, (d) outlet temperature, (e) oxygen pressures, and (f) fuel pressures. 119

A.13 Test 20241031-005 (a) axial heat flux, (b) thrust, (c) outlet pressure, (d) outlet temperature, (e) oxygen pressures, and (f) fuel pressures. 120

A.14 Test 20241031-006 (a) axial heat flux, (b) thrust, (c) outlet pressure, (d) outlet temperature, (e) oxygen pressures, and (f) fuel pressures. 121

A.15 Test 20241031-007 (a) axial heat flux, (b) thrust, (c) outlet pressure, (d) outlet temperature, (e) oxygen pressures, and (f) fuel pressures. 122

A.16 Test 20241031-009 (a) axial heat flux, (b) thrust, (c) outlet pressure, (d) outlet temperature, (e) oxygen pressures, and (f) fuel pressures. 123

B.17 Heat flux varying mass flux for (a) station 2 and (b) station 3 . . 124

B.18 Heat flux varying mass flux for (a) station 4 and (b) station 5 . . 124

B.19 Heat flux varying mass flux for (a) station 6 and (b) station 7 . . 125

B.20 Heat flux varying mass flux for (a) station 8 125

C.21 Water flow calibration data for (a) station 1 and (b) station 2. . . 126

C.22 Water flow calibration data for (a) station 3 and (b) station 4. . . 126

C.23 Water flow calibration data for (a) station 5 and (b) station 6. . . 127
C.24 Water flow calibration data for (a) station 7 and (b) station 8. . . 127
C.25 Water flow calibration data for (a) station 9. 128

List of Tables

4.1 Calibrated Discharge Coefficients 44

1 Experimentally Tested Set Conditions 130

List of Symbols

Symbol	Description
A	Area, m^2
A_n	Orifice Throat Area for Station n, m^2
A_{chamber}	Combustion Chamber Cross-Sectional Area, m^2
A_{cool}	Cooling Channel Cross-Sectional Area, m^2
A_{hot}	Cooling Channel Hot Side Area, m^2
A_{outer}	Combustion Chamber Outer Wall Area, m^2
A_{side}	Cooling Channel Side Wall Area, m^2
A_{t}	Throat Area, m^2
C^*	Critical Flow Factor
C_{d_n}	Discharge Coefficient for Station n
D_{h}	Hydraulic Diameter, m
D_{2_n}	Orifice Throat Diameter for Station n, m
D_{t}	Throat Diameter, m
I	Measured Current, A
L	Combustion Chamber Length, m
MW	Molecular Weight, kg/kmol

Symbol	Description
R	Specific Gas Constant, kJ/kg-K
R_c	Radius of Curvature, m
R_{u}	Universal Gas Constant, kJ/kmol-K
T	Temperature of a Fluid, K
T_0	Stagnation Temperature, K
T_{bulk}	Coolant Bulk Temperature, K
T_{in}	Inlet Temperature, K
T_{out}	Outlet Temperature, K
T_{wall}	Cooling Channel Hot Wall Temperature, K
$U_{95\%}$	95% Expanded Uncertainty
V	Velocity of a Fluid, m/s
ΔT	Temperature Difference, K
ΔT_n	Temperature Difference Between Inlet and Outlet Temperatures for Station n, K
$\Delta T_{n,n\pm1}$	Temperature Difference Between Adjacent Stations, K
α	Mass Flux Scaling Factor
β_n	Ratio of Diameters for Station n
$\dot{m}$	Mass Flow Rate, kg/s

Symbol	Description
$\dot{m}''$	Mass Flux kg/m^2-s
$\dot{m}_n$	Coolant Mass Flow Rate for Station n, kg/s
$\dot{m}_{\text{actual}}$	Actual Mass Flow Rate, kg/s
$\dot{m}_{\text{fuel}}$	Fuel Mass Flow Rate, kg/s
$\dot{m}_{\text{ideal}}$	Ideal Mass Flow Rate, kg/s
$\dot{m}_{\text{ox}}$	Oxidizer Mass Flow Rate, kg/s
$\dot{m}_{\text{ref}}$	Reference Total Mass Flow Rate, kg/s
$\dot{q}$	Heat Transfer Rate, W
$\dot{q}''$	Heat Flux, MW/m^2
$\dot{q}''_{n,s}$	Scaled Heat Flux for Station n, MW/m^2
$\dot{q}''_n$	Heat Flux for Station n, MW/m^2
$\dot{q}_{\text{h}_n}$	Cooling Channel Hot Wall Heat Transfer Rate for Station n, W
$\dot{q}_{\text{tot}_n}$	Total Heat Transfer Rate for Station n, MW
γ	Ratio of Specific Heats of a Fluid
κ	Thermal Conductivity, W/m-K
μ	Viscosity, kg/m-s
ν	Specific Volume of a Fluid, m^3/kg

Symbol	Description
ν_1	Chapman-Jouguet Reactant Specific Volume of a Fluid, m^3/kg
ν_2	Chapman-Jouguet Product Specific Volume of a Fluid, m^3/kg
ν_{eff}	Effective Degrees of Freedom
ϕ	Equivalance Ratio
ψ	Total Mass Flux, kg/m^2-s
ρ	Density of a Fluid, kg/m^3
ρ_1	Chapman-Jouguet Reactant Density, kg/m^2
ρ_2	Chapman-Jouguet Product Density, kg/m^2
ρ_n	Coolant Density for Station n, kg/m^2
σ	Dimensionless Boundary Layer Correction Factor
$\widehat{\mu}_y$	Uncertainty Weighted Average of Measurement y
c	Specific Heat Capacity, kJ/kg-K
c^*	Characteristic Velocity, m/s
c_{p}	Specific Heat Capacity at Constant Pressure, kJ/kmol-K
c_{v}	Specific Heat Capacity at Constant Volume, kJ/kmol-K
d	Channel Rib Thickness, m
d_1	Upstream Diameter, m

Symbol	Description
h_1	Chapman-Jouguet Reactant Enthalpy, kJ/kmol
h_2	Chapman-Jouguet Product Enthalpy, kJ/kmol
$h_{\mathrm{c,req}}$	Required Heat Transfer Coefficient, W/m^2-K
h_{c}	Liquid Film Heat Transfer Coefficient, W/m^2-K
$k_{95\%}$	95% Expanded Uncertainty Coverage Factor
m	Mass Collected, kg
p	Pressure of a Fluid, Pa
p_0	Stagnation Pressure, Pa
p_1	Chapman-Jouguet Reactant Pressure, Pa
p_2	Chapman-Jouguet Product Pressure, Pa
p_c	Chamber Pressure, Pa
p_{1_n}	Upstream Pressure for Station n, m^2
p_{abs}	Absolute Pressure, Pa
p_{abs}	Guage Pressure, Pa
p_{atm}	Atomospheric Pressure, Pa
q	Heat, kJ
s	Entropy of a Fluid, kJ/K
s_y	Standard Deviation of the Mean

Symbol	Description
t	Time, s
t_b	Firing Time, s
u_1	Chapman-Jouguet Reactant Velocity, m/s^2
u_2	Chapman-Jouguet Product Velocity, m/s^2
u_p	Velocity of Piston in Fickett-Jacobs Cycle, m/s
u_y	Standard Unceartainty of Measured Quantity y
v_cool	Coolant Velocity, m/s
x	Axial Distance, m
y	Average Measurement
ϵ_c	Contraction Ratio
Pr	Prandtl Number

Chapter 1. Introduction

1.1 Forward

Chemical rocket engines convert the chemical potential of propellants into thermal energy through combustion which is in turn transformed into to kinetic energy by expansion through a nozzle. Combustion can take place through two modes: deflagration or detonation. Deflagration is characterized by constant pressure subsonic combustion. A detonation is a supersonic combustion driven shock wave in which the shock wave compresses and heats the gas before it is combusted, further driving the detonation wave. Whether employing deflagrative or detonative combustion, a rocket engine combustion chamber wall experiences extreme heat loading. Although heat transfer methodology exists for deflagrative rocket engines, significantly less work has been done to understand the heat loads experienced by detonation-based propulsion. Specifically, this work seeks to further the understanding of heat flux loadings experienced by rotating detonation rocket engines (RDREs).

1.2 Detonation For Propulsion

The detonation phenomenon has been studied since the late 19^{th} century. Specifically, Bertholot and Veielle [1] conducted early work investigating the force

produced by the propagation of detonations in gaseous mixtures. Likewise, Mallard and Le Chatelier [2] conducted detonation tube studies focused on the mechanics behind the transition from deflagration to detonation. These early works laid the groundwork for the simple one-dimensional theory to be developed by Chapman [3] and Jouguet [4]. This was followed by the work of Berets, Greene, and Kistiakowsky [5], who compared the Chapman-Jouguet theory with experimental measurements of gaseous detonations with various hydrogen-oxygen mixtures. The fundamental understanding provided by these works lay the groundwork for the application of detonation to propulsion.

There have been many different concepts on the utilization of detonations for practical propulsion systems. Namely, concepts such as standing wave detonation engines, pulse detonation engines, and rotating detonation engines have all been investigated to potentially utilize the increased thermodynamic efficiency of detonation [6, 7].

A standing detonation wave engine, originally proposed by Nicholls [8], operates by injecting fuel into supersonic flow and creating a stabilized detonation as the flow goes over a wedge (see Fig. 1.1). This use of detonation for propulsion has potential applications in hypersonic flight despite being able to practically operate over a limited range of flight velocities [6]. This concept is currently being investigated in the form of an oblique detonation engine by The University of Central Florida [9].

The concept of a pulse detonation engine (PDE) was also investigated by Nicholls [11]. The PDE operates cyclically through the filling of a long tube with

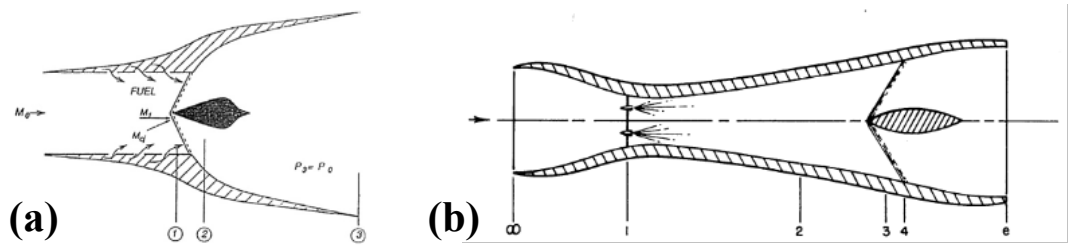


Figure 1.1: Schematic of a detonation driven ramjet (reproduced and edited from (a) [6] and (b) [10]).

a detonable gaseous mixture. The mixture is then ignited, detonated, exhausted to produce thrust, and then purged from the tube (see Fig. 1.2). The cycle then restarts with the filling of the tube. This cyclic process is not ideal as the detonation is not instantaneous, rather requiring time for the deflagration to detonation transition (DDT) process to take place [6]. Despite non-ideal processes, the PDE has been subject to much research [7, 12] and successfully implemented in demonstration flights [6, 13].

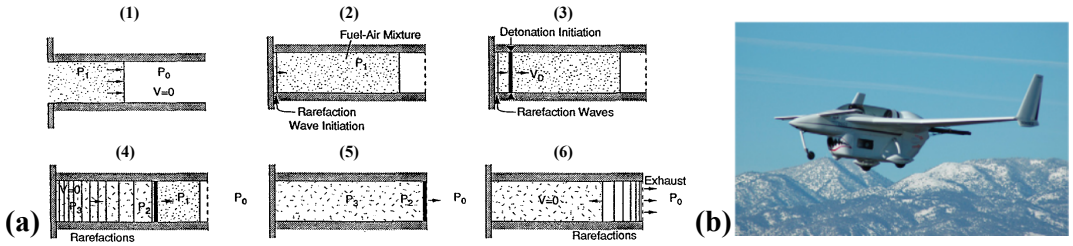


Figure 1.2: (a) PDE operation stages (reproduced and edited from [14]) and (b) PDE demonstration flight (Reproduced and edited from [6]).

Prior to the intentional implementation of rotating detonation waves for propulsion applications, Voitsekhovskii [15] observed spinning detonation waves with gaseous acetylene and oxygen. Nicholls observed transverse combustion in-

stabilities in conventional deflagrative engines [16], work stemming from a desire to understand the infamous thermoacoustic instabilities that plagued the development of the F-1 rocket engine during the Apollo program [17]. While early work sought to suppress these instabilities, rotating detonation engines (RDEs) are designed to intentionally promote these instabilities and amplify them to nonlinear saturation to achieve performance gains.

The rotating detonation rocket engine (RDRE) is characterized by a continuous detonation wave that travels around an annular combustion chamber. The RDRE avoids issues arising from the cyclic nature of the PDE by continuously feeding the detonation with fresh propellants. The RDRE consists of an annular chamber where fuel and oxidizer are continuously injected axially into the combustion chamber (Fig. 1.3 (a)). This results in one or more detonation waves traveling circumferentially around the annulus at supersonic speeds.

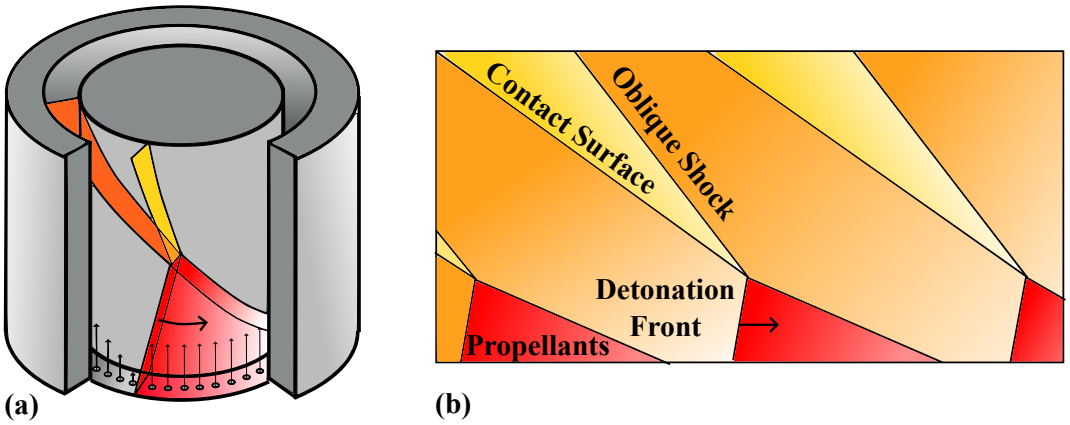


Figure 1.3: Schematic of RDRE with (a) cut view of RDRE revealing detonation front and (b) unwrapped detonation structure.

In recent years, there has been an increase in research to further understand and characterize the RDRE to advance its viability for propulsion applications [6, 18–20]. Many aspects of RDRE development have been experimentally investigated such as the effects of propellent combination [21, 22], chamber geometry [23–25], nozzle geometry [26–28], operability and performance [29–32], and injector scheme [33, 34]. An effort towards verification and validation of propulsion was recently orchestrated by the Air Force Research Laboratory in which multiple propulsion facilities tested the same set of hardware and produced results with consistent agreement [35]. There has also been an effort to investigate the operability and performance of both small-scale hardware for in-space applications [36–43], as well as large scale 20,000 N thrust class engine [44]. More recently, short duration demonstrator flights were performed by JAXA [45] on a sounding rocket, and Łukasiewicz Institute of Aviation [46]. Throughout all of these studies, a vast majority of the work for laboratory scale engines involve the use of short duration testing. As the technology matures and an effort is made to move towards more regular in-flight applications of RDREs, this will inevitably involve long duration operation, where technological challenges such as increased heat flux in these engines will need to be further understood.

1.3 Heat Transfer Measurements in RDRE

Currently, a majority of RDRE experimental work incorporates heat-sink geometries for short duration operation to avoid damage caused by these increased heat loads [43, 47]. However, to integrate these engines into practical

long-duration flight hardware, the combustion chamber wall will need to be cooled due to the increased heat flux in RDRE compared to equivalent deflagrative engines. To properly design actively-cooled hardware, the heat flux need to be experimentally measured. There has been work in this area, however, not enough has been done to fully understand and characterize the thermal loadings seen in an RDRE.

One heat-sink hardware study performed measurements of wall heat flux for a 76.2 mm OD in Micka et al. [48], finding the maximum heat flux in the detonation region near the injector to be 23.6 MW/m^2. Additionally, heat flux near the injection plane did not follow the traditional mass flux scaling of the Bartz correlation for equivalent deflagrative devices [48, 49]. High-frequency heat flux measurements taken by Theuerkauf et al. [50, 51] show heat flux ranging from $1 - 9$ MW/m^2 for a 152.4 mm water-cooled RDRE. Additively manufactured actively-cooled chambers have also been explored using axial channels to enable long duration testing and calorimetry measurements of detonation-based rocket engines [52, 53]. However, circumferential channels offer the ability to reveal the axial heat flux distribution over the length of the combustor. This approach is implemented by Aliakbara et al. [54] who demonstrated axially resolved water-based calorimetry measurements of a 100 mm mean diameter combustor. Location and magnitude of maximum heat flux is shown to be dependent upon injector design, with the maximum measured heat flux around $8 - 9$ MW/m^2 [54]. More recently, heat flux measurements have been taken by Hernandez-McCloskey et al. [52, 55] for a 50.8 mm diameter engine as well as for a 158.7 mm engine tested at NASA

Marshall [44]. These works reflect a push to understand the underlying scaling parameters associated with RDRE. The aim of this work seeks to add to this body of knowledge with heat flux measurements of heat flux in a 76.8 mm RDRE calorimeter.

Chapter 2. Background Concepts

The simple one-dimensional Chapman-Jouguet theory is presented, followed by the more in depth Zeldovich-von-Nuemann-Döring (ZND) model. Through this analysis, it can be shown that the detonation cycle can produce a theoretical increase in thermodynamic efficiency compared to an equivalent deflagrative cycle. Lastly, an overview on calorimetry experiments, conventional heat flux scaling, and additive manufacturing techniques is presented.

2.1 Chapman-Jouguet Theory

The utilization of detonation as a means for propulsion requires review of basic detonation theory. Although detonations involve an inherently complex three-dimensional flow field, much understanding can be obtained through simple one-dimensional analysis. The simplest theory of a detonation wave is the Chapman-Jouguet (CJ) theory [3, 4]. This thermodynamic model assumes the detonation front can be modeled by an infinitely thin shock wave immediately followed by a region of heat release [56]. This analysis assumes (1) one-dimensional steady flow, (2) constant area, (3) ideal gas behavior, (4) constant and equal specific heats, (5) negligible body forces, and (6) adiabatic conditions [57]. The

analysis is done assuming an infinitely thin shock in the detonation wave-fixed reference frame (Fig. 2.1) propagating into a quiescent medium.

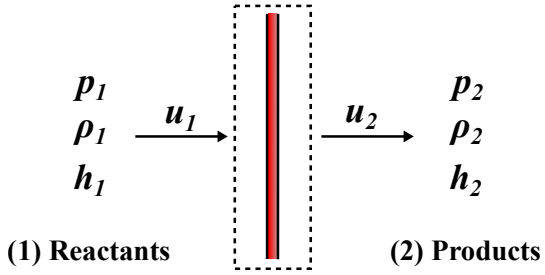


Figure 2.1: An idealized 1-D Chapman-Jouguet Detonation.

From this, simple control volume analysis yields the mass, momentum, and energy conservation equations can be written for the system as the following:

$$\rho_1 u_1 = \rho_2 u_2 \tag{2.1}$$

$$p_1 + \rho_1 u_1^2 = p_2 + \rho_2 u_2^2 \tag{2.2}$$

$$h_1 + \frac{1}{2}\rho_1 u_1^2 = h_2 + \frac{1}{2}\rho_2 u_2^2. \tag{2.3}$$

Here, state 1 corresponds to the reactants upstream of the detonation wave (ρ_1, u_1, p_1, h_1) and state 2 indicates the product gases downstream (ρ_2, u_2, p_2, h_2). Through the definition of enthalpy and assuming a calorically perfect gas mixture, the energy conservation equation can be rearranged to include a heat addition term, q, defined to be the heat of combustion per mass of mixture. This allows the energy conservation equation, Eq. (2.3), to be written as

$$c_{\mathrm{p}}T_1 + \rho_1 u_1^2 + q = c_{\mathrm{p}}T_2 + \rho_2 u_2^2, \tag{2.4}$$

where c_{p} is the specific heat capacity at constant pressure of the fluid.

Through the assumption (3) of ideal gas behavior, a state relationship can be written as,

$$p = \rho RT, \tag{2.5}$$

where R is the specific gas constant ($R = R_{\mathrm{u}}/MW$).

By simultaneously solving the conservation of mass and momentum equations, the Rayleigh line is obtained and is given by:

$$\frac{(p_2 - p_1)}{(\nu_2 - \nu_1)} = -\dot{m}"^2, \tag{2.6}$$

where $\dot{m}''$ is the mass flux, and ν_1 and ν_2 are the reactant and product specific volume.

For a fixed mass flow rate, upstream pressure (p_1), and upstream specific density ($\nu = 1/\rho$), Eq. (2.6) is rearranged into the equation of the Rayleigh line,

$$p_2 = a\nu_2 + b, \tag{2.7}$$

where $a = -\dot{m}"^2$ and $b = p_1 + \dot{m}"^2\nu_1$ Plotting Eq. (2.7) in $p-\nu$ space, it is apparent that the slope of the Rayleigh line is dependent upon the mass flux, $\dot{m}"$.

Next, the Hugoniot curve is defined by solving the mass, momentum, and energy conservation equations to give

$$\frac{\gamma}{\gamma-1}(p_2\nu_2 - p_1\nu_1) - \frac{1}{2}(p_2 - p_1)(\nu_2 - \nu_1) - q = 0, \tag{2.8}$$

where γ is the ratio of specific heat capacities.

Given known conditions for state 1, the Hugoniot curve defines the locus of all points that satisfy the conservation equations (Eq (2.1)-(2.3)). Equations (2.7) and (2.8) can be rearranged such that the pressure ratio between states 1 and 2 is a function of the specific volume ratio across the detonation. The equation for the Rayleigh line becomes

$$\frac{p_2}{p_1} = \left[-\frac{u_1^2}{p_1\nu_1}\right]\frac{\nu_2}{\nu_1} + \left[1 + \frac{u_1^2}{p_1\nu_1}\right], \tag{2.9}$$

and the equation for the Hugoniot curve is given by

$$\frac{p_2}{p_1} = \frac{\left[\frac{\gamma+1}{\gamma-1} + \frac{2\gamma}{\gamma-1}\frac{q}{c_{\mathrm{p}}T_1}\right] - \frac{\nu_2}{\nu_1}}{\left[\frac{\gamma+1}{\gamma-1}\right]\frac{\nu_2}{\nu_1} - 1}. \tag{2.10}$$

The Rayleigh Line and the Hugoniot curve can be plotted in $p - \nu$ space (Fig. 2.2) assuming heat addition ($q = 0.5$ plotted). Plotting a Hugoniot curve such that $q = 0$ corresponds to the solution of the mass, momentum, and energy conservation equations without heat addition; this is equivalent to the solution for an adiabatic shock wave.

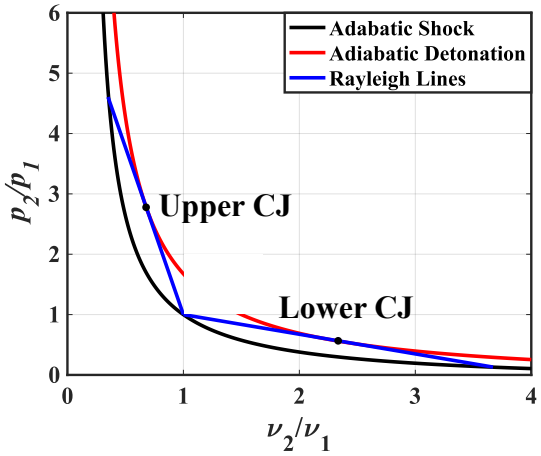


Figure 2.2: Rayleigh Lines and Hugoniot curves plotted in $p - \nu$ space.

Rayleigh lines are only valid solutions within the physical region such that $0 < \dot{m}" < \infty$, creating an upper and lower region in the Hugoniot curve corresponding to a supersonic detonation solution and a sub-sonic deflagration solution, respectively. For both the upper and lower branches, there exists a solution such that the Rayleigh line is tangent to the Hugoniot curve. These points are designated as the upper and lower Chapman-Jouguet (CJ) points. The CJ points correspond to the solution where (1) entropy generation is a minimum, (2) the downstream velocity is subsonic, and (3) the detonation wave speed is determined.

For a detonation wave, the gas follows the adiabatic shock Hugoniot curve until it intersects with the Rayleigh line, designated as the von Neumann (VN) point. Heat is added to the flow along the Rayleigh line until the gas reaches the CJ point. The upper CJ point corresponds to the minimum entropy rise, corresponding to the maximum thermodynamic efficiency, motivating the desire for a detonation based cycle.

2.2 ZND Model

The simple theory outlined by Chapman and Jouguet provide a simplified thermodynamic analysis describing relationships between two equilibrium states separated by an infinitely thin detonation wave. The Zeldovich-von-Neumann-Döring model (ZND) is a non-equilibrium analysis that provides a more detailed description of the internal mechanisms present in the detonation wave [58–60]. Namely, this model does not assume an infinitely thin shock but rather explains the physical processes occurring between state 1 and 2, varying in both space and time, through a shock of finite thickness. The model consists of (1) a shock wave with negligible thickness propagating at the CJ velocity, (2) an induction zone and (3) a reaction zone (Fig. 2.3). The shock wave travelling at the CJ velocity adiabatically compresses the gas along the shock Hugoniot curve to the VN point. In the induction zone thermal dissociation causes the formation of radicals due to shock heating. Finally, within the reaction zone combustion, energy release, and expansion of products occurs [61]. This is represented by following the Rayleigh line from the VN point to the CJ point.

2.3 Cycle Analysis

Historically, the conversion of chemical potential energy into thermal energy is achieved through deflagration in traditional rocket engines. The desire to utilize a detonation-based cycle comes from the potential to extract more useful work compared to a deflagrative cycle. This can be evaluated from a cycle

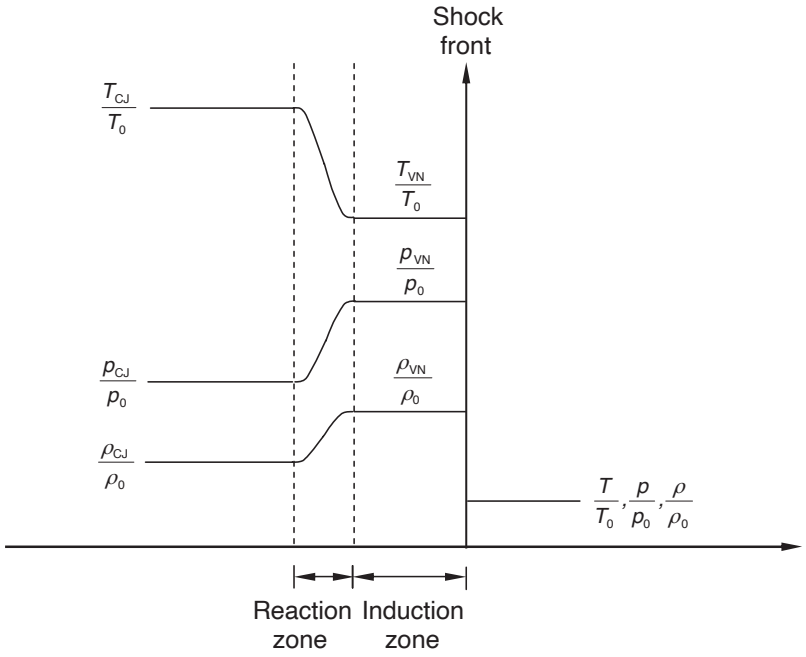


Figure 2.3: Structure of the detonation wave as described in the ZND model (Reproduced from [61]).

perspective using simple thermodynamic modeling to compare the traditional deflagrative cycle to that of a detonative cycle.

A system utilizing deflagrative combustion such as an air-breathing jet engine where air is compressed, combusted, and useful work is extracted via a turbine, can be thermodynamically modeled using the Brayton Cycle. This cycle consists of (1) isentropic compression of a gas, (2) heat addition through combustion of that gas at constant pressure, (3) the heated, pressurized gas undergoing isentropic expansion, work extraction, and (4) isobaric heat rejection to return to the initial state. This thermodynamic cycle can be represented in both the $p-\nu$ (Fig. 2.4 (a)) and $T-s$ space (Fig. 2.4 (b)).

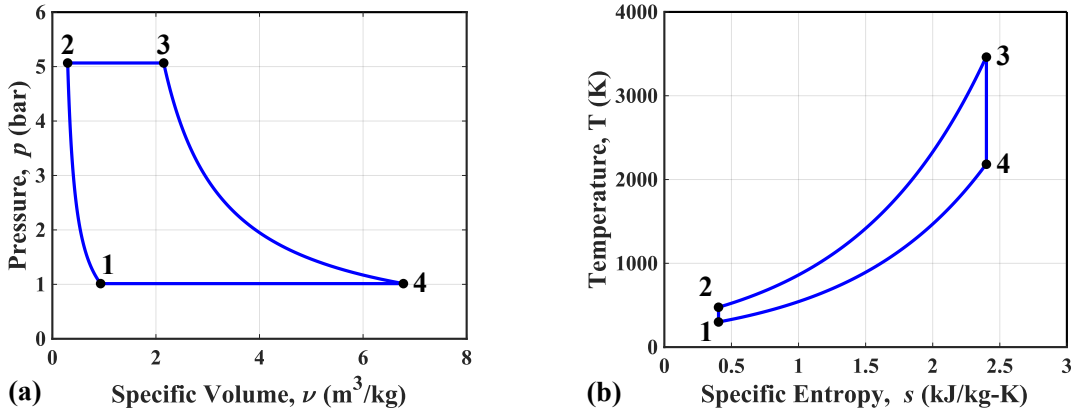


Figure 2.4: Brayton cycle diagrams, (a) $T-s$ and (b) $p-\nu$.

While this analysis is used to describe the thermodynamic process in a constant pressure deflagrative rocket engine, a detonation-based engine requires different treatment. The Fickett-Jacobs (FJ) cycle can be used to describe the idealized detonation cycle, representing an upper bound on the amount of useful work that can be extracted by a detonation-based cycle [56, 62, 63]. This analysis is suitable to represent RDREs as the heat addition process provided by the detonation wave occurs fast enough such that the local fluid can effectively be modeled as an isochoric system. The FJ cycle is modeled using a piston-cylinder system (Fig. 2.5) assumed to be a closed system. In this cycle, at step (a-b) a volume of reactive gas is isentropically compressed between two massless pistons that can move independently. By application of external work (c), the piston on the left is moved toward the right with velocity u_p. This instantaneously initiates a detonation wave at the face of the left piston that propagates through the reactive gas to the right piston (d). The right piston, along with the entire system, then travels to the right at the velocity u_p (e). This motion is converted

to external work after which the products are adiabatically expanded to the initial pressure (f). Heat is then extracted from the gas at constant pressure to return to the initial temperature (g). Finally, the products are converted to reactants at constant pressure and temperature to return the gases back to state 1 (h).

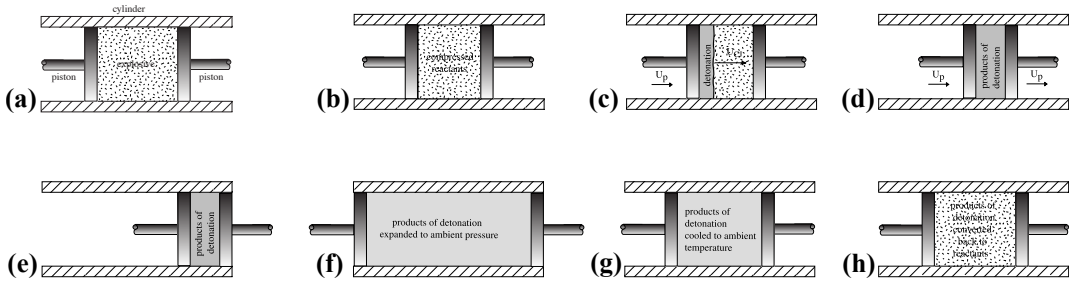


Figure 2.5: Fickett-Jacobs model for detonation (reproduced and edited from [14]).

The work between the FJ and Brayton cycle can be compared by plotting the state points on a $p - \nu$ diagram (Fig. 2.6). Consider a stoichiometric mixture ($\phi = 1$) of methane and oxygen at initial pressure and temperature of $p_1 = 1$ bar and $T_1 = 300$ K. For both the FJ and the Brayton cycles, this mixture undergoes isentropic compression to state 2. For the FJ cycle, the detonation pressure and temperature are evaluated using the state 2 pressure and temperature, p_2 and T_2 to obtain the post-detonation pressure and temperature p_3 and T_3. For the Brayton cycle, heat is added at constant pressure to reach state 3 by assuming the heat into the system to be the heat of combustion of stoichiometric methane oxygen burning at p_2, and T_2. Both cycles are then isentropically expanded back to the initial pressure p_1.

The total work that can be extracted by a cycle is represented by the area inscribed by the state points. The FJ cycle will allow an estimated 20% increase

in cycle efficiency compared to that of the Brayton cycle for a given compression ratio [6] due to this increased area (Fig. 2.6).

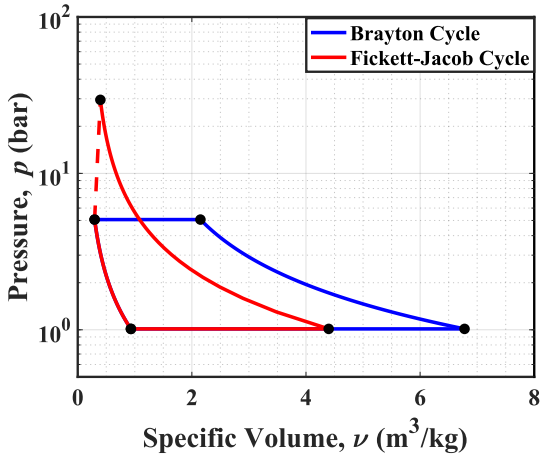


Figure 2.6: Fickett-Jacobs cycle comparison to the Brayton Cycle for methane-oxygen at $\phi = 1$.

2.4 Calorimetry

In chemistry, calorimetry is the practice of measuring changes in state variables to derive the heat transfer associated with the change in state. Through knowledge of the temperature at two states, the amount of heat transferred into (or out of) that system can be determined. A canonical calorimeter experiment is the cup calorimeter (Fig. 2.7). This experiment consists of a known mass m of liquid, typically water, at state (i) where $T = T_1$ and $p = p_{\text{atm}}$. Keeping pressure constant, heat is added to the system either by conduction or a chemical reaction. The temperature is recorded at state (ii), where $T_2 = T_1 + \Delta T$.

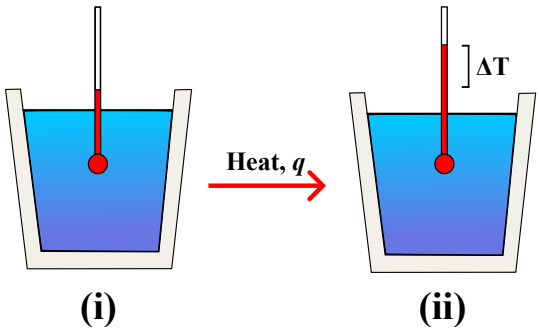


Figure 2.7: Cup calorimetry experiment where water undergoes a process that results in a temperature difference between states (i) and (ii).

Through the rise in temperature, the heat that is transferred to the system q can be determined by

$$q = mc\Delta T, \tag{2.11}$$

where m is the mass of the water in the cup, c is the specific heat of water, and ΔT is the measured temperature rise.

The same concept can be used to determine the heat transferred to the wall of a rocket engine [64–66]. In this experiment type, cooling water flows around a combustion chamber outer wall (Fig. 2.8). In this case, the heat added to the system is a result of combustion occurring in the chamber transferring heat into the chamber wall, which in turn transfers that heat into the cooling water. Similarly to the cup calorimeter, the heat transferred into the system can be determined by measuring the water temperature at the inlet state (i) and outlet state (ii).

In this setup, Eq. (2.11) is divided by time to obtain the heat transfer rate $\dot{q}$ as the coolant mass flow rate $\dot{m}$ is typically a measured quantity. This gives

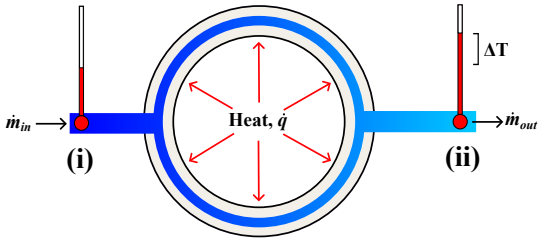


Figure 2.8: Rocket engine calorimetry experiment where water travels circumferentially around the combustion chamber to measure temperature difference between states (i) and (ii).

the heat transfer rate into the combustion chamber walls as

$$\dot{q} = \dot{m}c\Delta T. \tag{2.12}$$

This work utilizes this concept to measure the amount of heat transferred into the combustion chamber wall of an RDRE.

2.5 Constant Pressure Engine Heat Transfer

Whether implementing either detonative or deflagrative combustion, rocket engine combustion chambers must withstand immense heat flux levels. Deflagrative engines often require the implementation of cooling techniques to keep the hot wall below the material melting temperature. Cooling techniques such as film, radiation, ablative, transpiration, and regenerative cooling have been used historically in constant pressure rocket engines [67]. Regenerative cooling involves the routing of one or both propellants through channels around the hot wall. Heat is picked up by the flowing coolant before it is then injected into the combustion

chamber. The flow of coolant helps manage the thermal load experienced by the engine walls while also increasing the injection temperature of the propellants.

To properly design such engines, heat flux correlations are often utilized. Heat flux scaling for traditional constant pressure rocket engines are historically modeled through semi-empirical heat transfer coefficient correlations such as the Bartz correlation [49] (Eq. (2.13)). The Bartz correlation for the gas side heat transfer coefficient is typically represented as

$$h_{\mathrm{g}} = \left[\frac{0.026}{D_{\mathrm{t}}^{0.2}}\left(\frac{\mu^{0.2}c_{\mathrm{p}}}{\mathrm{Pr}^{0.6}}\right)\left(\frac{p_{\mathrm{c}}}{c^*}\right)^{0.8}\left(\frac{D_{\mathrm{t}}}{R_c}\right)\right]\left(\frac{A_{\mathrm{t}}}{A}\right)^{0.9}\sigma, \tag{2.13}$$

where D_{t} is the throat diameter, μ is the viscosity, c_{p} is specific heat at constant pressure, Pr is the Prandtl number, p_c is chamber pressure, c^* is the characteristic velocity. Also, R_c is radius of curvature, A_{t} and A are throat area and area respectively, and σ is the correction factor for property variations across the boundary layer. The driving scaling relationship in this correlation is dominated by local mass flux through the combustors, which tradiationally scales to the power of 0.8.

As RDREs continue to find applications across a wide range of length scales, their design will require the development of scaling parameters similar to Eq. (2.13). Due to the underlying constant pressure assumptions in Eq. (2.13), further research is required to facilitate the development of such correlations for detonation-based propulsion.

2.6 Additive Manufacturing

Additive Manufacturing (AM) has been widely adopted in the aerospace industry due to benefits such as a reduction in component lead time, cost, and mass as well as increased design freedom [68]. To date, many metal AM processes have been developed, however, the two most prominent categories are Directed Energy Deposition (DED) and Powder Bed Fusion (PBF). The DED process works by depositing powder from a blown or wire feedstock into a thermal energy source on a specified location on the print. PBF works by spreading a thin layer of metal powder across a print bed in which an energy source is used to melt the powder to form the cross section of the printed part (see Fig. 2.9). This is repeated layer by layer until the full part is completed. For AM processes implementing a laser to melt the powder, the technique is called Laser Powder Bed Fusion (L-PBF).

Actively cooled hardware requires the manufacturing of complex cooling channel geometries, which is made easier by additive manufacturing when compared to traditional subtractive methods. In this current study, recent improvements in AM are leveraged to produce the complex geometries necessary for axially resolved actively cooled calorimetry hardware. AM geometries provide a path forward to more rapidly increase the technological readiness level of RDREs by enabling increased test durations, as well as provide means to collect average heat flux measurements. While several alloys have been developed for use in L-PBF, a high conductivity, specially formulated copper-chrome-niobium alloy, GRCop-42

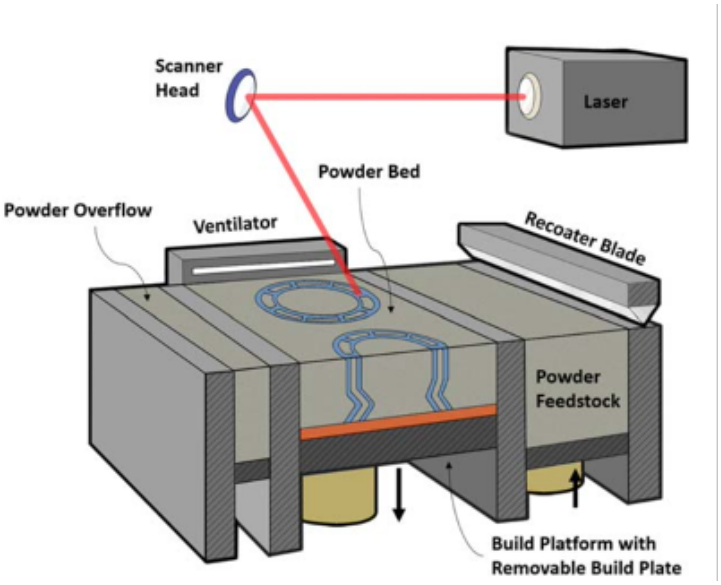


Figure 2.9: Schematic of L-PBF process (Reproduced from [69]).

[70], is best utilized in high heat flux applications. The properties of GRCop-42 make it the ideal candidate for RDRE calorimetry hardware developed in this work using the L-PBF process.

Chapter 3. Engine Design

In the current work, a water-based outer body calorimeter is designed to enable long duration firing times through the implementation of sufficient cooling to the combustor wall while providing finely resolved axial heat flux measurements. The RDRE tested is an AM 76.8 mm OD RDRE that implements a modular design consisting of (1) an outer body, (2) an inner body, (3) an expanding nozzle, and (4) a propellant manifold (see Fig. 3.1(a)). As the hardware is modular, it can be tested with various configurations of different injector, outer body, and inner body designs.

For this study, the RDRE hardware is tested in three different configurations: (1) heat-sink straight channel (Fig. 3.1(a)), (2) water-cooled straight channel (Fig. 2.1(b)), and (3) water-cooled constricted geometry (Fig. 2.1(c)). The heat-sink straight channel configuration consists of the straight center body and the straight heat-sink outer body, while the water-cooled straight channel and constricted geometry configurations utilize the water-cooled calorimetry outer body with the straight and constricted center bodies, respectively.

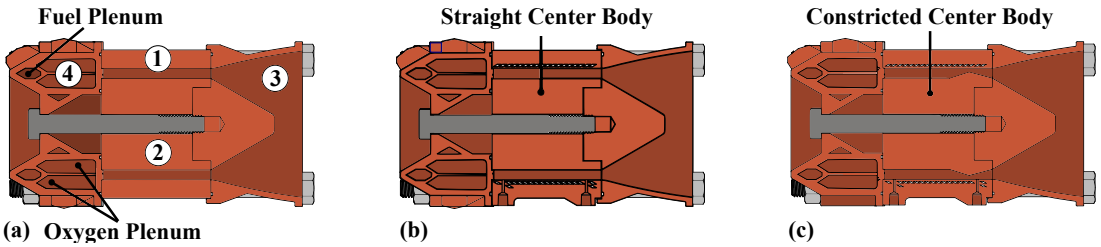


Figure 3.1: Schematic of 76.8 mm RDRE configurations: (a) heat-sink straight channel, (b) water-cooled straight channel, and (c) water-cooled constricted geometry.

3.1 Heat-Sink Hardware

For the heat-sink hardware, the components of the engine are secured via four 12.7 mm stainless steel bolts that pass through the nozzle and propellant manifold, and are secured by nuts on the back side (see Fig. 3.2). The components are held together, as well as secured to the thrust stand, through the compression of these four bolts. O-ring grooves on the propellent manifold and nozzle allow for sealing against the flat surfaces of the inner body and either side of the outer body. The two pieces that comprise the center body are sealed using RTV to prevent the combustion gases from reaching the center bolt that secures the center body to the propellant manifold.

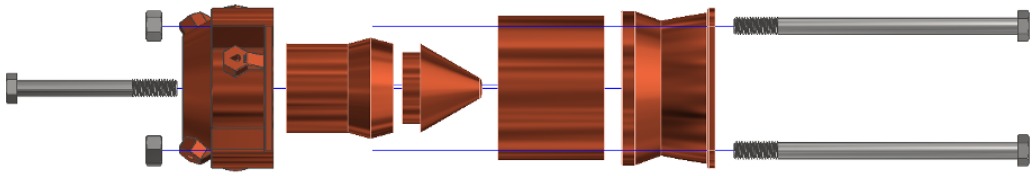


Figure 3.2: Exploded view of modular 76.8 mm RDRE with heat-sink outer body.

3.1.1 Outer Body

The outer body for the heat sink hardware is a straight hollow cylinder with an inner diameter of 76.2 mm and an outer diameter of 102.8 mm. The part is conventionally machined out of GRCop-42 and has a length of 76.2 mm and a wall thickness of 12.7 mm.

3.1.2 Inner Body

Two center body designs are evaluated: a straight center body and a constricted center body. Each of the center body designs consist of a base with a through hole and a threaded tip. Additionally, a third center body configuration (Fig. 3.3 (a)) of a flat cylindrical puck is used during some tests to investigate the sensitivity for the elimination of the conical spike. The constricted center body is conventionally machined with a contraction ratio of $\epsilon_c = 2.34$ where the throat is located at $x/L = 0.77$ (Fig. 3.3(b)). The contraction ratio required to achieve the desired chamber pressure is determined using an in-house RDRE thermodynamic model [71], based on the work of Burr and Paulson [72]. The straight center body has a diameter of 63.5 mm and an annular width of 6.65 mm. The expansion ratio of the nozzle is 5.1 when using the straight center body and 12.7 with the constricted center body. For the straight center body configuration, the outer-diameter-to-length-ratio is unity while it is 0.77 when implementing the constricted center body. Due to spatial constraints, neither of the center body designs are actively-cooled. The center body is secured with a bolt that passes

through the propellant manifold and threads into the 30° conical tip of the center body.

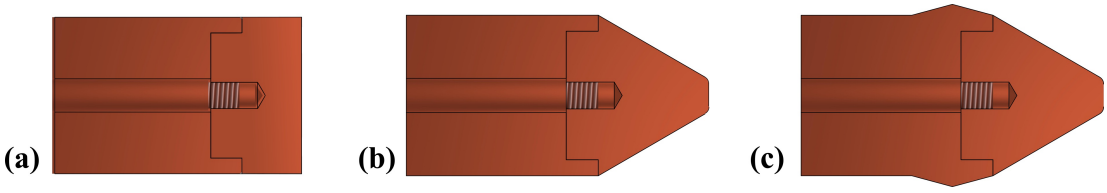


Figure 3.3: Center body configurations tested: (a) straight puck, (b) straight cone, and (c) constricted.

3.1.3 Propellant Manifold

The propellant manifold consists of the oxidizer and fuel plenums that supply uniform propellant flow to the injector face (Fig. 3.4). The injector face and the plenums are additively manufactured in one monolithic piece. The fuel plenum passes fuel through 40 posts arranged in a circular pattern around the manifold to supply fuel to the injector face. These fuel posts pass through the oxygen plenum, which is a larger cavity that supplies oxidizer to the injector. The injector is an impingement style injector with 40 elements spaced evenly about the annulus designed similarly to those outlined by Teasley et al. [73].

3.2 Calorimetry Outer Body

The calorimeter is additively manufactured out of GRCop-42. The hardware consists of 18 total circumferential cooling channels, where water is supplied by three inlets with measurements taken from two channels grouped together, comprising nine total axial stations. Using this configuration, heat flux measure-

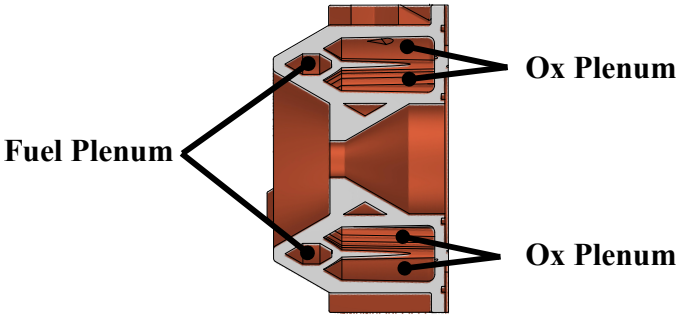


Figure 3.4: Propellant manifold cut view showing propellant plenums.

ments are taken at nine axial locations spaced 7.5 mm apart starting from the injector face to the combustor exit (see Fig. 3.5).

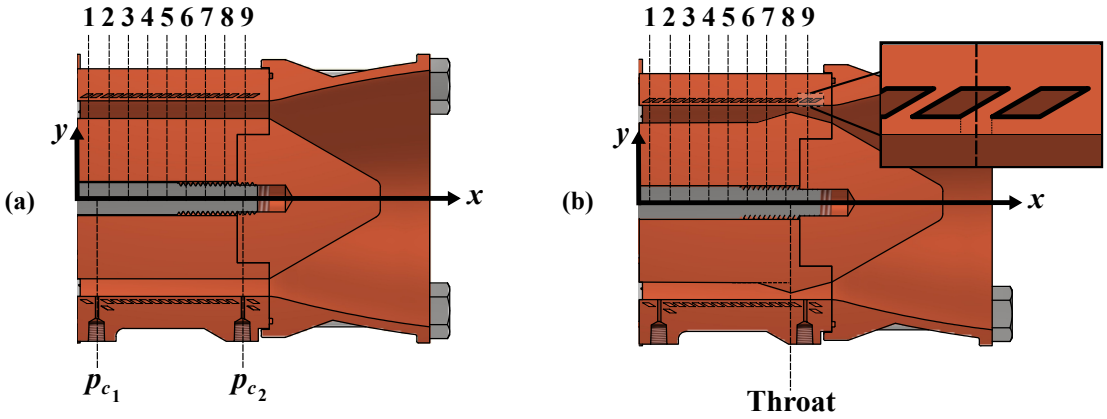


Figure 3.5: Calorimetry outer body axial stations in relation to the (a) straight center body and (b) constricted center body.

Water is supplied to the cooling channels via three inlet manifolds (Fig. 3.6 (a)). Each of these manifolds internally separate the flow into six channels that travel around the outer body circumferentially and recombine into three distinct outlet channels that create a total of three coolant inlets and nine coolant outlets (Fig. 3.6 (b)).

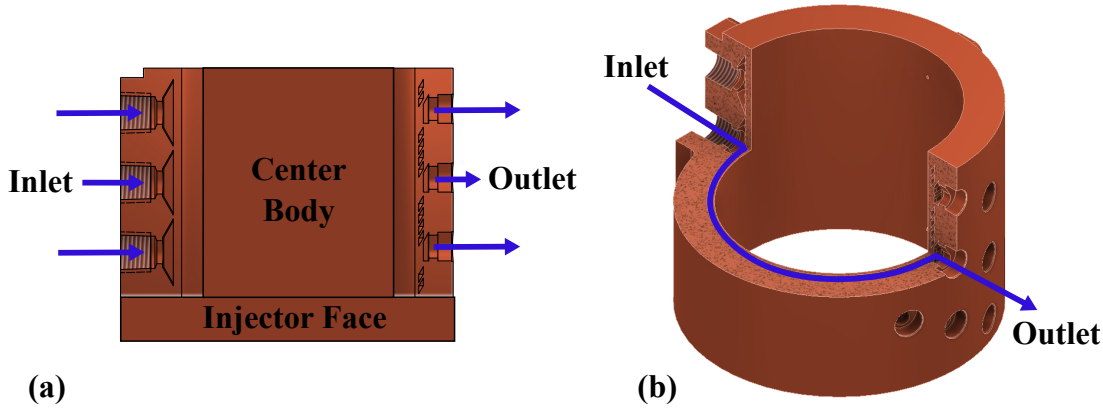


Figure 3.6: Propellant manifold cut view showing propellant plenums.

The channels wrap circumferentially to the exit manifold 180° from the inlet, six of which are staggered at 160° and 200° from the inlet position to provide appropriate clearance for diagnostics (Fig. 3.7(b)-(d)).

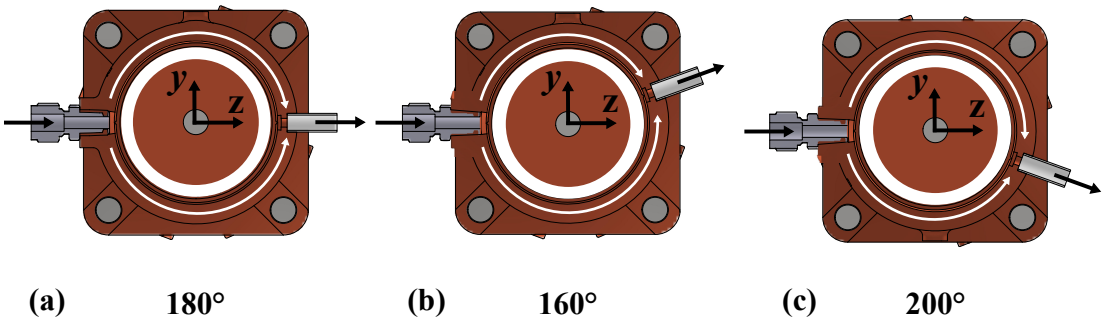


Figure 3.7: Coolant flow path with inlet (a) 180°, (b) 160°, and (c) 200° from coolant exit.

3.2.1 Channel Sizing

To appropriately design the cooling channels, several factors are considered following the methodology developed by Hernandez-McCloskey et al. [52].

First, it is critical to know the maximum coolant flow rate for the facility. In this study, a 12.4 MPa, 227 liter coolant tank is used to supply deionized water through the RDRE's cooling channels. At the maximum working system pressure of 12.4 MPa, the theoretical facility flow rate is 6 kg/s. The required coolant flow rate is dependent upon the amount of heat flux originating from combustion of the propellants to the combustion chamber wall, as well as the internal geometry of the cooling channels. In order to perform the initial coolant flow rate analysis, wall conduction-based heat flux measurements for a similarly sized 76.2 mm OD design taken by Micka et al. [48] for gaseous methane-oxygen are used. This work reports a maximum heat flux closest to the injector face of 23.6 MW/m^2 for a total propellant mass flow of $\dot{m} = 0.34$ kg/s at an equivalence ratio (ϕ) of 1.15. Additionally, for a larger engine (OD = 100 mm), Aliakbara et al. [54] shows heat flux approaching 8.25 MW/m^2 for a total propellant mass flow of $\dot{m} = 0.5$ kg/s at an equivalence ratio of $\phi = 1.2$. Assuming an equivalent heat transfer for a 76.8 mm combustor provides an estimated heat flux of 5 MW/m^2. These heat fluxes are used as bounds to determine the required coolant mass flow rate for the 76.8 mm calorimetry hardware implemented in this study, as the present work has a nominal operating condition of $\dot{m} = 0.33$ kg/s and $\phi = 1.1$.

The total heat flux is assumed to be evenly distributed along the combustion chamber outer wall. The heat transfer rate to the combustion chamber wall, $\dot{q}$, is then determined by multiplying the heat flux, $\dot{q}''$, by the geometry's outer wall surface area, A_{outer}, as

$$\dot{q} = \dot{q}'' A_{\text{outer}}. \tag{3.1}$$

To minimize the uncertainty of the calorimetry measurements, the coolant must be kept below its saturation temperature. This is done to prevent nucleate boiling from occurring within the coolant channels, which can locally alter the heat transfer coefficient, h_c, from the wall to the coolant. This is undesirable for calorimetry applications as the nucleate boiling causes local increased heat transfer into the coolant, leading to high uncertainty heat flux measurements. To avoid this, an initial coolant exit temperature target of $T_{out} = 600$ K is taken as the saturation temperature of the coolant (i.e., deionized water) at the working pressure, $p = 12.4$ MPa. The difference between ambient temperature ($T_{in} = 298$ K) and this outlet temperature is used as the estimated target temperature rise across the hardware. Combining the initial temperature drop through the cooling channels and the experimentally determined value of the heat transfer rate, the mass flow required is given by

$$\dot{m} = \frac{\dot{q}}{c(T_{out} - T_{in})}, \tag{3.2}$$

where T_{in} and T_{out} are the coolant inlet and exit temperatures respectively, $\dot{m}$ is the coolant mass flow rate, and c is the average coolant specific heat capacity.

Next, the total cross-sectional area of the cooling channels, A_{cool}, is sized to determine the flow velocity associated with the required coolant mass flow rate. Kolb et al. [74] showed the limiting diameter for powder removal of a straight internal channel with a circular cross section to be 0.5 mm. Due to the long-curved channels of this calorimeter, an increased cross-sectional area is selected to ensure powder removal. With fixed channel dimensions, the coolant channel

velocity v_{cool} is found to be 21 m/s through mass conservation assuming steady operation. The liquid film coefficient for flow in pipes, h_{c}, is used to model heat transfer in the cooling channels [75] and is determined by

$$h_{\text{c}} = 0.023c\frac{\dot{m}}{A_{\text{cool}}}\left(\frac{D_{\text{h}}v_{\text{cool}}\rho}{\mu}\right)^{-0.2}\left(\frac{\mu c}{\kappa}\right)^{-\frac{2}{3}}, \tag{3.3}$$

where D_{h} is the hydraulic diameter, ρ is the coolant density, κ is the coolant thermal conductivity, and μ is the coolant dynamic viscosity [70]. This parameter is the heat transfer coefficient required to achieve the target temperature rise across the hardware.

Once the coolant side heat transfer coefficient is known, the heat transfer coefficient required by Newton's law of cooling ($h_{\text{c,req}}$) is determined using the anticipated local heat flux as

$$h_{\text{c,req}} = \frac{\dot{q}}{(T_{\text{bulk}} - T_{\text{wall}})}, \tag{3.4}$$

where the coolant channel bulk temperature is assumed to be the outlet temperature ($T_{\text{bulk}} = T_{\text{out}}$) and the hot wall temperature. T_{wall}, is assumed to be the coolant saturation temperature. To ensure that the hot chamber wall is sufficiently cooled, h_{c} must be greater than $h_{\text{c,req}}$. To satisfy this condition, the target temperature drop of coolant in the channels (ΔT) is decreased by lowering T_{out} and iterating until $h_c > h_{\text{c,req}}$.

Overall, the flow rate necessary to cool the higher heat flux of 23.6 MW/m^2 seen in Micka et al. is determined to be 4.5 kg/s, while the necessary flow rate

to cool 8.25 MW/m^2 is found to be 1.36 kg/s. Both of these required flow rates fall within the flow rate capability of the facility. Therefore, this is a conservative required coolant flow rate estimation that is consistent with the experimental coolant mass flow rate.

3.2.2 Internal Channel Geometry

Using this approach, the channel dimensions required to satisfy this cooling requirement at the available flow rate are determined (Fig. 3.8). Using these channel dimensions and the minimum required rib thickness, a total of 18 cooling channels can be fit within the available space. Internally, the cooling channels incorporate a parallelogram cross-sectional profile where the the top of the internal channels are kept within 30° of vertical due to AM overhang angle printing constraints [69].

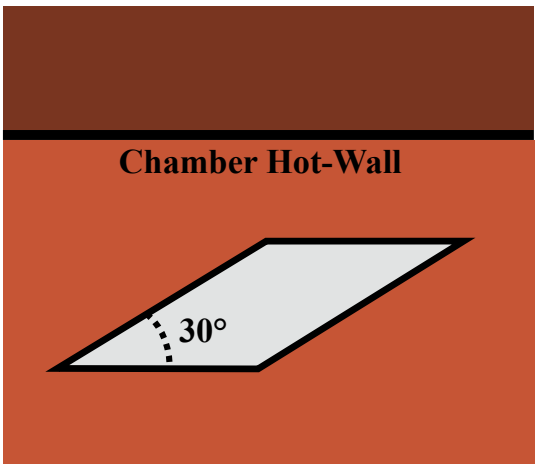


Figure 3.8: Schematic of internal channel dimensions.

3.2.3 CTAP Routing

To allow for the measurement of the chamber pressure through the outer body, the internal geometry is designed such that the cooling channels are locally raised around capillary tube attenuated pressure (CTAP) sensor ports at axial locations $x/L = 0.10$ and 0.86 (Fig. 3.9 (a)). The CTAP port is a straight 0.83 mm teardrop hole normal to the surface of the inner wall. To provide an isolated measurement of the static pressure, the CTAP holes must be normal to the axial flow path to avoid introducing pressure measurement error from angling the CTAP hole [76]. During the calorimetry tests, only p_{c_1} is measured to provide the time-averaged chamber pressure at $x/L = 0.10$. To provide this clearance, one of the channels comprising both stations 1 and 9 are locally raised and extended outward to simultaneously allow clearance for the CTAP hole and avoid interfering with any other cooling channels (Fig. 3.9 (b)-(d)).

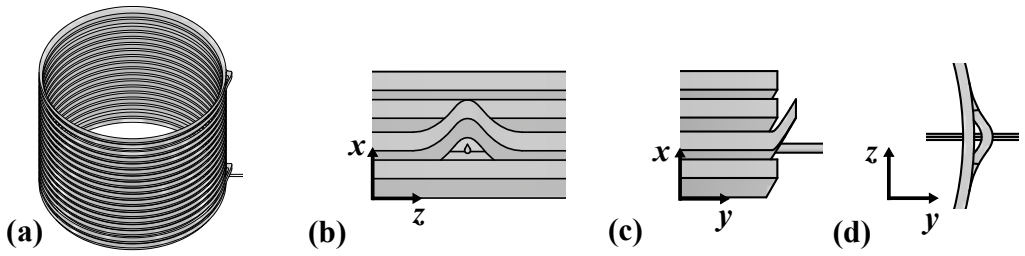


Figure 3.9: Schematic of the internal cooling channels fluid volume for (a) whole device, and (b)-(d) detail view of CTAP channel routing viewed from each plane.

3.3 Flow System Design

To supply the hardware with the necessary cooling water, a flow system is designed and installed. A 227-liter water tank supplies cooling water to the calorimetry outer body. Gaseous nitrogen is used to supply head pressure to the tank. Water supply is initiated before the experiment using a pneumatic ball valve. A manifold splits the water supply into three tubes that enter one side of the calorimeter. Pressure and temperature of the coolant are measured (1) upstream of the coolant manifold, (2) upstream of a calibrated orifice (downstream of the hardware), and (3) assumed to release to atmosphere through stainless-steel orifices. The orifices are machined and calibrated in house.

To keep the downstream pressure measurements (2) within the range of the available instrumentation (0-3.4 MPa), the coolant orifices are sized using a GFSSP [77] model (Fig. 3.10). This initial model covers the entire coolant flow system from the coolant supply tank, through the internal channels to the outlet orifice. The model represents the internal channels as pipes with an internal absolute roughness of 0.15 μm. Each coolant inlet splits into the six channels with both the left and the right length of channel represented. These channels then recombine into the nine outlets each with a 4.37 mm diameter orifice releasing to atmosphere. Figure 3.10 represents a third of the internal channels to save space. This model worked for an initial sizing; however, the internal resistances of the additively manufactured cooling channels were significantly underestimated.

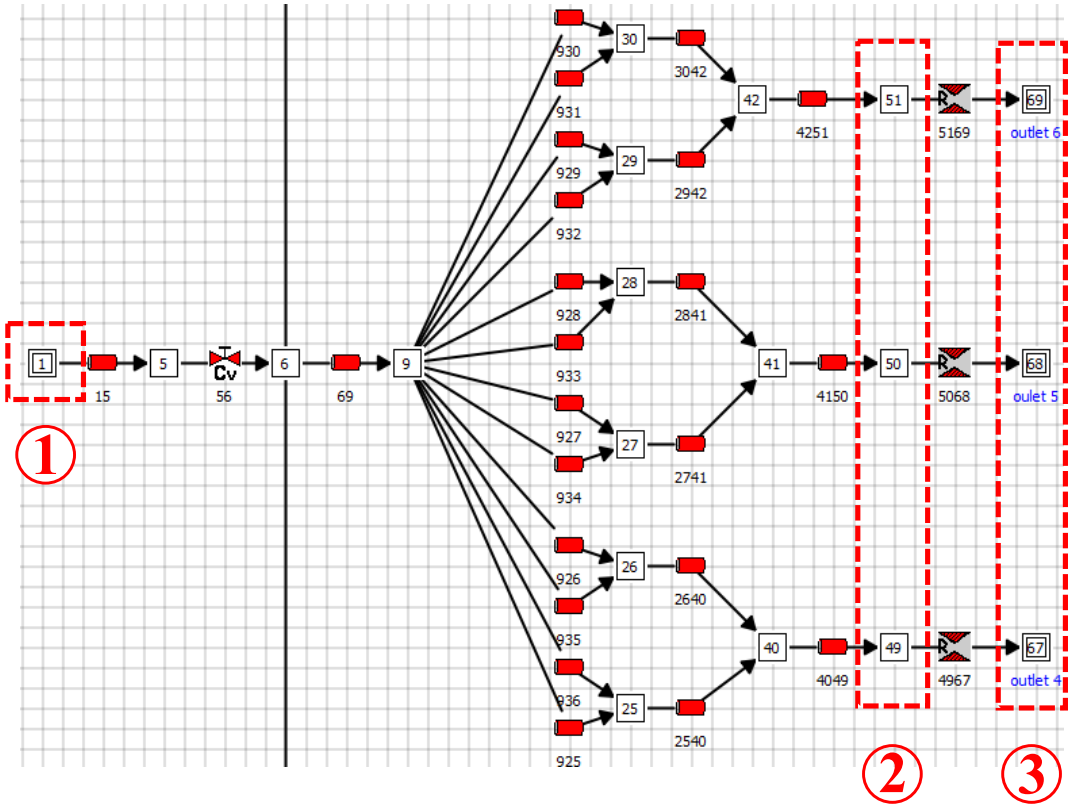


Figure 3.10: Initial GFSSP model of coolant flow path used for initial orifice sizing (Model 1).

This model is used to inform the selection of the diameter of the downstream orifice. These results were compared to the actual channel resistances after performing a water calibration. A second GFSSP model is made to incorporate the measured discharge coefficients of both the internal channels and the downstream orifices. Model 2 (Fig. 3.11) simplified the network from Model 1 by combining the entire channel geometry, modeling the internal channels as a resistance. This results in a simpler model going from (1) the tank set pressure, (2) the downstream pressure, and (3) atmospheric pressure. Discharge coefficients

(C_d) obtained through a catch and weigh experiment are converted into equivalent flow coefficients and used as parameters for the resistances in Model 2.

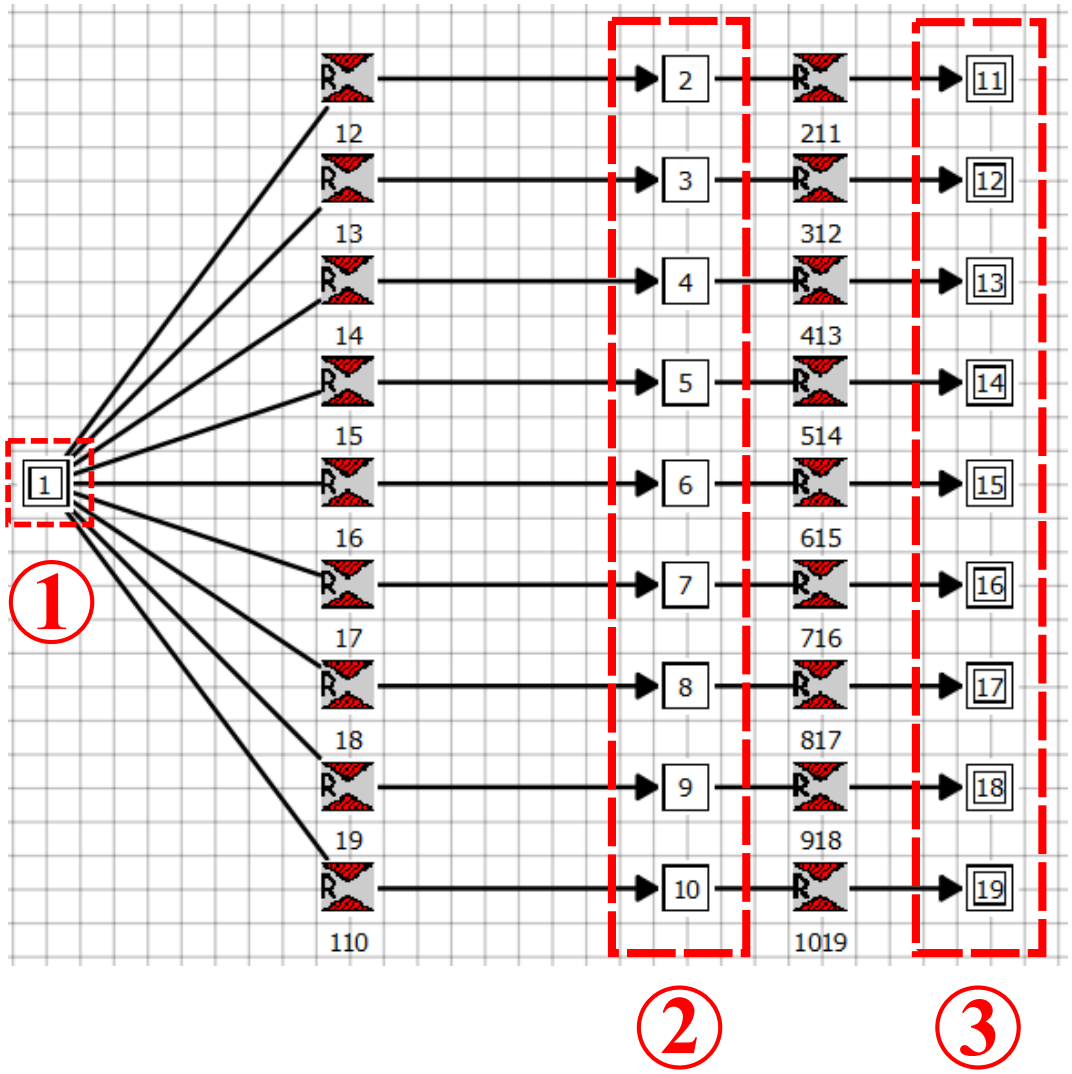


Figure 3.11: Second GFSSP model to incorporate experimentally measured resistances (Model 2).

Both GFSSP models dramatically under-predicted the pressure loss across the additively manufactured hardware. Model 1 does not consider the inter-

nal roughness introduced to the channels from the AM process, representing an idealized version of the system. Model 2 represents accurate channel and orifice discharge coefficients however does not accurately represent the experimental pressure drop across the hardware. The experimental pressures shown are obtained by averaging the pressures taken during all of the hot fire tests performed. The pressure drop across the hardware predicted by Model 1 is an order of magnitude less than the pressure drop that was seen experimentally (Fig. 3.12). This is due most likely to both channel roughness as well as the curvature of the internal channels which contributed to the increased pressure loss across the hardware.

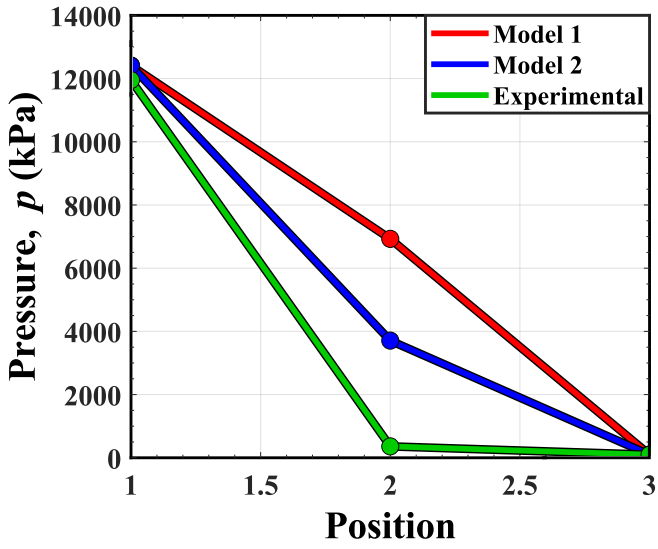


Figure 3.12: Pressure throughout coolant delivery system at (1) tank, (2) downstream of hardware, and (3) atmosphere.

Chapter 4. Experimental Setup and Testing

Water calibration and hot fire testing for this work are performed at the Propulsion Research Center's (PRC) high pressure spray facility and hot-fire test cell, respectively. Water flow calibration of the calorimetry outer body is performed prior to proceeding to the hot fire test of the RDRE with integrated calorimetry outer body.

4.1 Water Calibration

The purpose of the water calibration experiment is two-fold. Firstly, to enable accurate determination of coolant mass flow rate during hot fire testing of the actively cooled RDRE by determining the discharge coefficients (C_{d}) of both the internal channels and the flow metering orifices. Secondly, this testing allows for confirmation that the coolant flowed through the additively manufactured channels, and the brazed outlet tubes, as designed.

4.1.1 Experimental Setup

A catch-and-weigh is performed to determine the actual mass flow rate allowed through the hardware for a given set pressure. Five set pressures ranging from $1.7 - 7.7$ MPa are collected ascending in pressure and then descending in

pressure. For each test, the water supply valve is opened, allowing coolant to flow through the hardware to atmosphere. After sufficient time for the pressure to reach steady state, a bucket is inserted into the water stream. At the same time, a stop watch is started. After sufficient time, the bucket is removed from the flow, the stop watch is stopped, and the mass collected is weighed using a scale. The actual mass flow rate data is recorded and this is repeated for the next set pressure.

4.1.2 Calibration Flow System

Water is provided to the hardware with a 227-liter stainless steel tank. Head pressure is supplied to the tank via pressurized air tanks and the water is filled with filtered city water. The water flow is controlled by a pnuematic ball valve directly downstream of the tank (see Fig. 4.1).

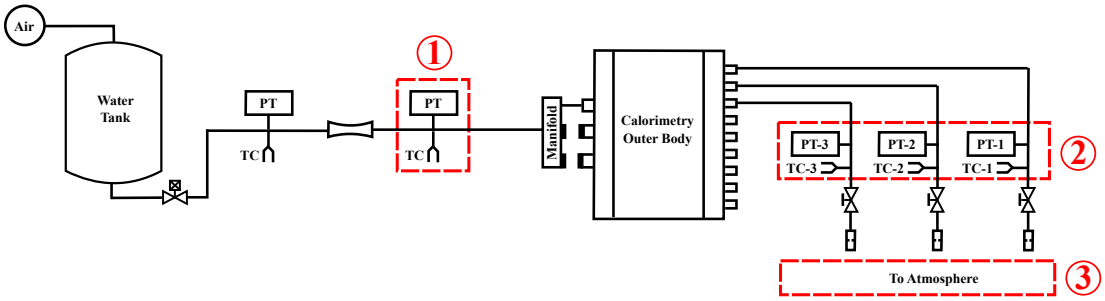


Figure 4.1: Simplified plumbing and instrumentation diagram for the water calibration flow system.

Stainless steel tubing (25.4 mm) runs from the tank to a 9.4 mm venturi before continuing to a manifold block. The manifold splits the 25.4 mm tubing to three 9.5 mm stainless steel tubes feeding into the coolant inlets on the hardware.

The calorimetry outer body is secured to a table by a restraining plate and a bolt that passed through the plate, annulus, and table (see Fig. 4.2). In-line with two of the three outlets not being evaluated are closed hand valves, and a flow metering orifice at the outlet of the channel being evaluated. All of the plumbing is secured to the table using tube tie-downs (see see Fig. 4.2 (a)). Pressures and temperature measurements are taken with static pressure transducers and T-type thermocouples, at three locations, (1) upstream of venturi, (2) downstream of venturi, and (3) at hardware outlet (see Fig. 4.1).

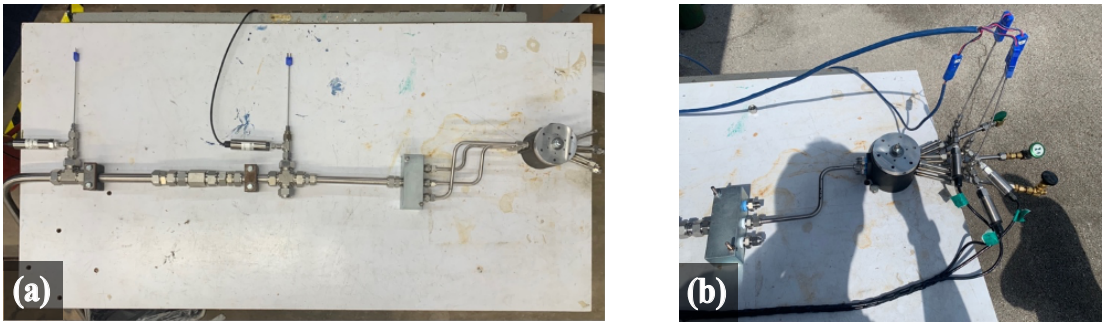


Figure 4.2: Image of (a) calibration water supply plumbing and (b) calibration testing setup.

A catch-and-weigh is performed for each of the channels individually. Flow is isolated for individual channels by attaching a hand valve to the exit of the two channels that are internally connected to the channel that is being tested. Three pressure and temperature measurements are taken at the hardware exit with one at each station in a given group of three. Cooling water is only provided to one third (three stations) of the hardware at a time by capping the other two inlet tubes at the coolant manifold (Fig. 4.2 (b)).

In addition to testing each channel individually, one test is performed flowing three internally connected channels at once (Stations 7-9). These measurements are comparable to the resistances obtained during the individual channel tests. In addition to this, to confirm the all the channels flowed as expected at the same time, a test is carried out allowing all nine of the internal channels to release to atmosphere (Fig. 4.3). Data was not collected for this test due to limitation on the number of available voltage-based pressure transducers.



Figure 4.3: Full flow test of calorimeter during calibration testing.

4.1.3 Flow Calibration Results

From the data collected, the actual mass flow rate ($\dot{m}_{\text{actual}}$) is given by mass divided by time (m/t) and the ideal mass flow rate ($\dot{m}_{\text{ideal}}$) given by Bernoulli's equation

$$\dot{m}_n = A_n \sqrt{\frac{2\rho_n(p_{1_n} - p_{\text{atm}})}{1 - \beta_n^4}}, \tag{4.1}$$

where $\beta_n = D_{2_n}/d_1$, d_1 is the upstream tube diameter, D_{2_n} is the orifice throat diameter, A_n is the orifice throat or cooling channel area, p_{1_n} is the coolant pressure immediately upstream of the orifice, p_{atm} is the atmospheric pressure directly downstream of the outlet orifice, and ρ_n is the density upstream of the orifice for a given cooling channel n. This density is determined by using the CoolProp open-source thermophysical property library [78].

By definition, the discharge coefficient is the slope of the line created by plotting the flow calibration data obtained at varying pressure. The obtained flow calibration data is used to determine the discharge coefficient for both the hardware channels and the mass flow metering orifice, C_{d_n}, given by

$$C_{\text{d}_n} = \frac{\dot{m}_{\text{actual}}}{\dot{m}_{\text{ideal}}}. \tag{4.2}$$

While the data obtained at different set pressures is expected to collapse to the same line, this is not observed across all pressures for the data collected. The flow calibration data (Fig. 4.4) exhibits a bimodal behavior where there exists two distinct lines at lower pressures ($p < 5$ MPa) than at higher pressures ($p > 5$ MPa). The average discharge coefficient of 0.85 is obtained through a least squares regression on the low pressure data, while the high pressure data yields an average discharge coefficient of 0.73 with an intercept closer to zero than the low pressure data. This shift in data is not attributable to a change in the experimental setup between tests, as this behavior is consistently observed for all 9 of the axial stations (see Appendix C). The high pressure data is utilized to determine the discharge coefficient for the mass flow metering orifice. This choice

was made because (1) the pressure range is more representative of the pressure used during hot fire testing, (2) the associated slope is closer 0.7 which is more representative for the discharge coefficient for an orifice with an $L/d \approx 1$ [75], and (3) the intercept is closer to zero which is to be expected from the definition of the discharge coefficient. Due to these reasons, an uncertainty weighted average of the high pressure data is taken to be the discharge coefficient. Details of the uncertainty weighted average are found in section 5.5.6. The discharge coefficients for the hardware as well as the mass flow metering orifices are shown in Table 4.1.

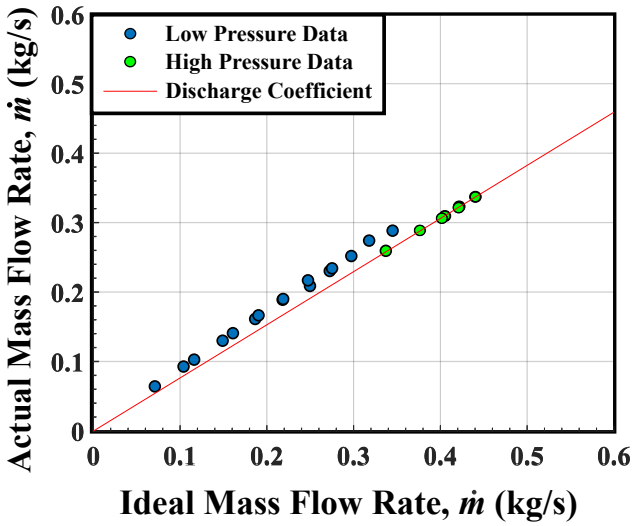


Figure 4.4: Example mass flow rate data for station 1 mass flow metering orifice.

The discharge coefficients for the internal channels are extremely low, with an average of $C_\mathrm{d} = 0.091$. The discharge coefficients of the flow metering orifices have an average of $C_\mathrm{d} = 0.731$. These values are used to calculate the coolant mass flow rate during hot fire operation of the hardware.

In addition to the discharge coefficients, coolant was confirmed to internally flow through the hardware as designed. It was also seen that, due to internal manifolding, some of the cooling channels experienced higher mass flow rate than others. This is discussed in more detail as it relates to the determination of heat flux in section 5.2.

Table 4.1: Calibrated Discharge Coefficients

Station	**1**	**2**	**3**	**4**	**5**	**6**	**7**	**8**	**9**
Axial Location, x/L	0.058	0.166	0.266	0.366	0.466	0.566	0.666	0.766	0.866
Channel C_d	0.088	0.098	0.087	0.089	0.096	0.084	0.098	0.097	0.087
Orifice C_d	0.765	0.765	0.735	0.747	0.740	0.688	0.713	0.719	0.709

4.2 Engine Hot Fire

Engine hot fires of the RDRE are performed for both the uncooled heat-sink and water cooled calorimetry outer bodies. Initial checkout testing with the uncooled hardware is performed to explore the operability of the hardware, ultimately informing the selection of the operational points tested for the calorimetry hardware. The experimental setup presented is for that of the calorimetry testing. The same setup is used for the heat-sink testing excluding the coolant delivery system.

4.2.1 Experimental Setup

The hot-fire testing of the RDRE is performed in the open air test facility at the PRC [79] with the engine mounted horizontally to a 22 kN thrust stand (see Fig. 4.5). Propellant is supplied to the test cell bulkhead by compressed gas cylinders (four fuel and six oxidizer) and is controlled using dome-loaded pressure regulators. The propellants used in this study are gaseous methane (GCH_4) and oxygen (GO_2).

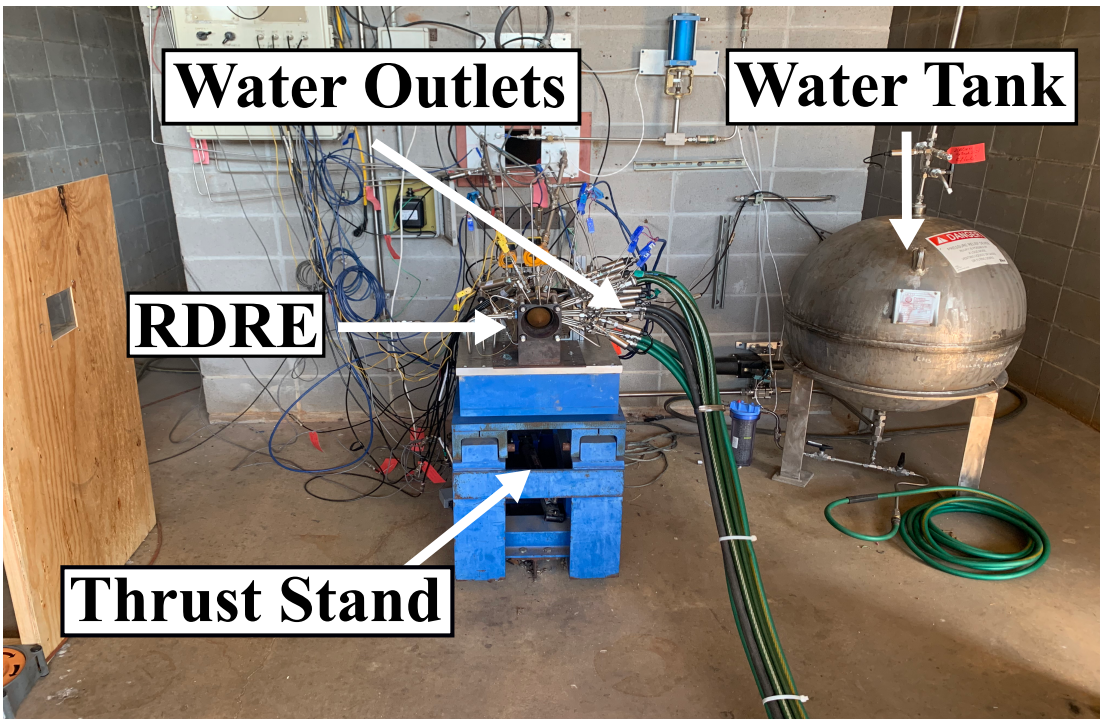


Figure 4.5: Experimental test cell setup with RDRE mounted to thrust stand and coolant water tank.

4.2.2 Propellant Flow System

Propellant mass flow rate is measured using critical flow orifices [80], where pressure and temperature measurements are taken immediately upstream with static pressure transducers and T-type thermocouples, respectively (Fig. 4.6). The mass flow metering plumbing is secured to the test cell bulkhead. Propellant flow past the bulkhead is controlled by two pnuematic ball valves (fire valves) on both the fuel and oxygen lines (Fig. 4.7 (a)). The engine along with propellant plumbing is purged with gaseous nitrogen.

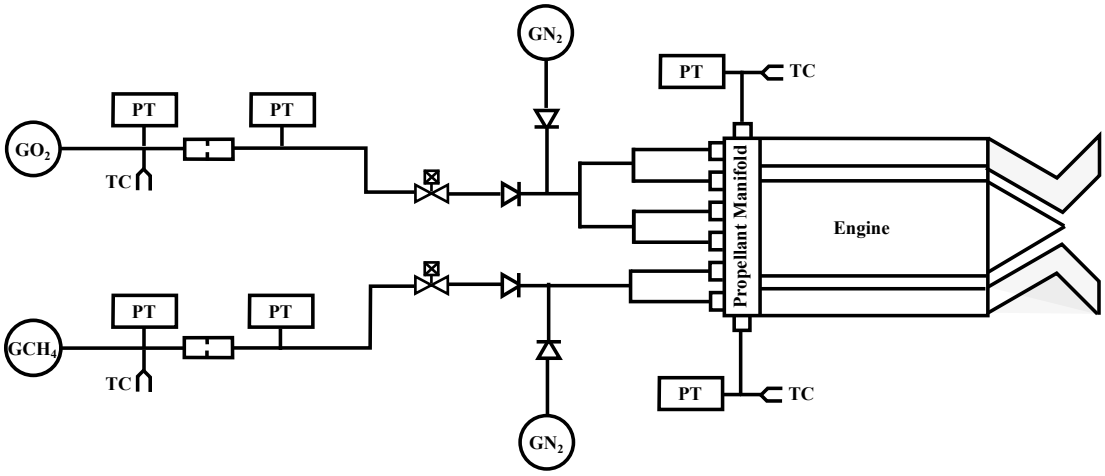


Figure 4.6: Generalized Plumbing and Instrumentation Diagram of propellant flow system.

Downstream of the fire valves, the fuel plumbing branches to two inlet ports supplying gaseous methane to the fuel plenum. The oxygen plumbing separates into four lines providing even flow to the oxidizer manifold (Fig. 4.7 (b)). In the propellant manifold, oxygen and fuel plenum pressures are measured using static pressure transducers and K-type thermocouples. All diagnostics in the ex-

perimental setup are sampled with a National Instruments-based data acquisition system at 1 kHz for all pressures and 90 Hz for all temperatures.

For ignition, the engine is back lit using a GH_2-GO_2 torch. At the beginning of each test, propellants flow through the torch body and are ignited using an automotive spark plug. A 6.35 mm stainless steel tube directs the ignition flame into the aft end of the engine to achieve ignition.

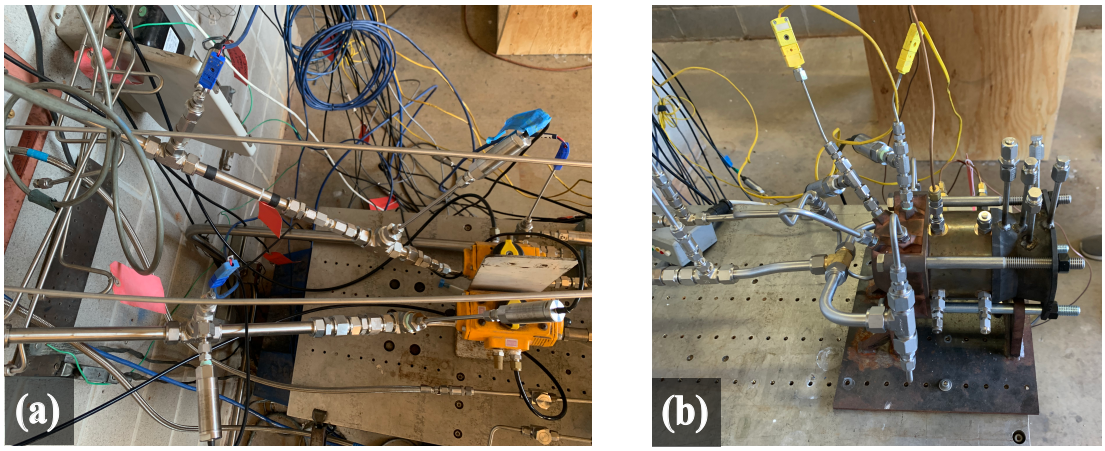


Figure 4.7: Propellant plumbing (a) downstream of fire valves going into hardware and (b) mass flow metering plumbing upstream of fire valves.

4.2.3 Coolant Flow System

The cooling water head pressure is set to 12.4 Mpa, corresponding to a mass flow rate of 2 kg/s, for each test provided by a pressurized tank utilizing gaseous nitrogen (GN_2) as the pressurant. Stainless steel tubing (25.4 mm) runs from the tank to a manifold block that splits the flow of coolant into the three 9.53 mm tubes that provide water to the calorimeter inlets. Inlet pressure and temperature are measured upstream of the manifold block.

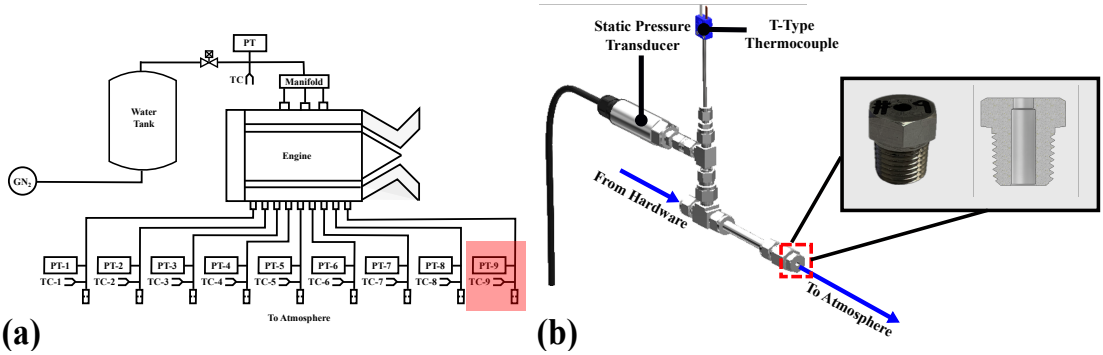


Figure 4.8: Schematic of (a) generalized Plumbing and Instrumentation Diagram of coolant flow system and (b) detailed view of downstream plumbing and instrumentation.

Coolant outlet pressure and temperature are taken 10 mm downstream of the hardware for each of the nine outlets static pressure transducers and T-Type thermocouples. The coolant mass flow rate is measured on a per outlet basis using nine calibrated 4.37 mm orifices immediately downstream of the outlet pressure and temperature measurements (Fig. 4.8 (b)). The cooling water is released through the orifices to garden hoses that direct the cooling water out of the test cell (Fig. 4.9).

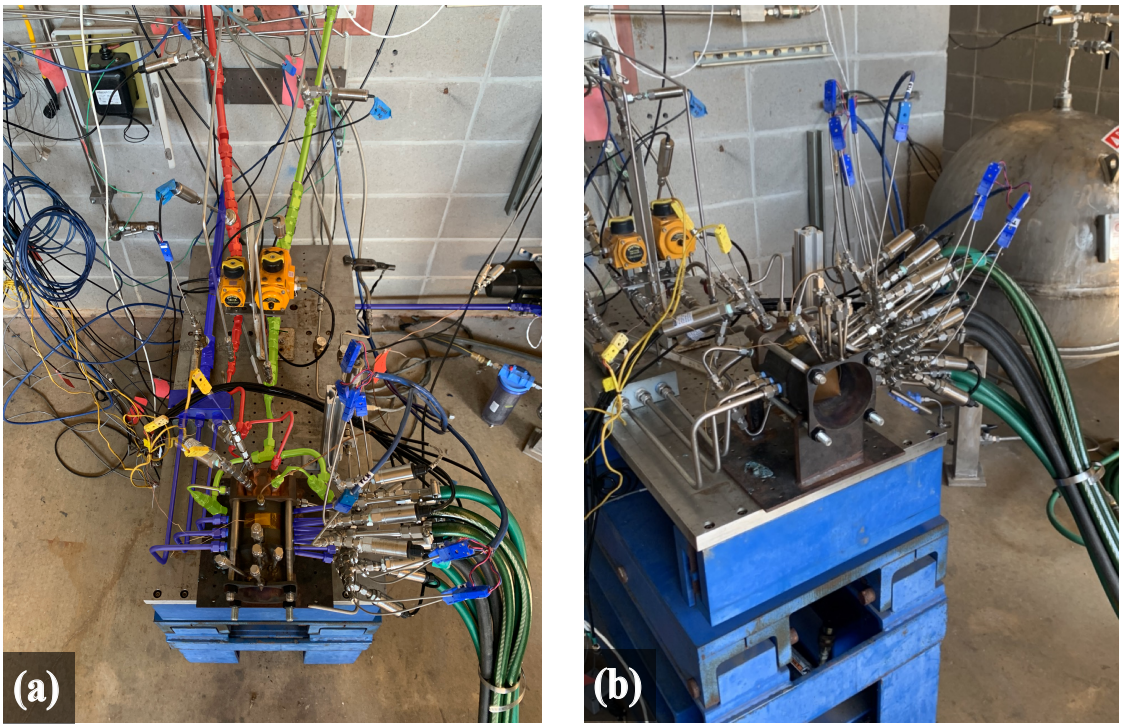


Figure 4.9: RDRE, plumbing, and instrumentation for hot fire testing with (a) top-down view of oxygen (green), fuel (red), and coolant (blue) plumbing and (b) isometric view of hardware on test stand.

4.2.4 Optics

Wave dynamics are identified using high-speed visible luminescent imaging of the detonations provided by a Phantom TMX 5010 and a 200 mm lens (Nikon AF Micro-NIKKOR 200mm f/4.0D IF-ED) directed into the annulus of the engine via a mirror positioned in line with the exit of the combustor (see Fig. 4.10). High-speed imaging is captured at 200 kfps at a resolution of 256x128 px. High-definition low speed video is captured providing both side view and the top-down view of the RDRE hot-fire.

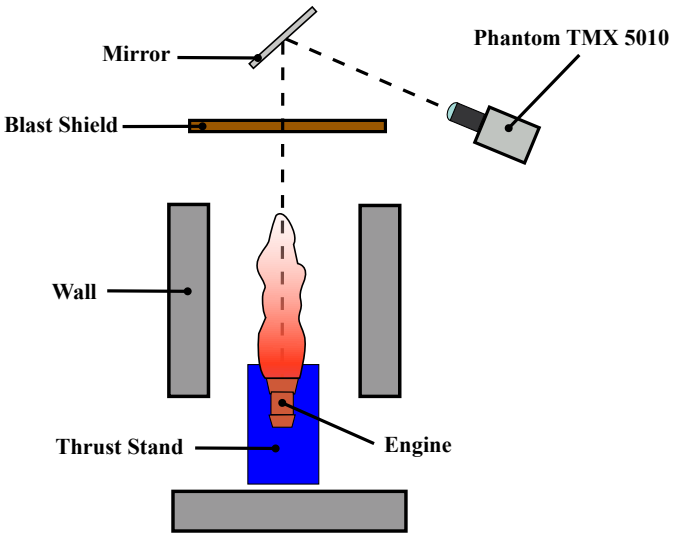


Figure 4.10: Optical diagnostics setup.

Chapter 5. Data Reduction

The experimental data taken for this work consists of pressure and temperature measurements. From this data, (1) propellant mass flow rates, (2) coolant mass flow rate, (3) chamber pressure, (4) and heat flux are derived. High-speed aft end imaging is also analyzed to extract wave dynamics in the combustion chamber.

All pressure and temperature data are taken for the entirety of the hot fire test. To avoid using data during the startup transient and to capture heat flux once thermal steady state has been reached, pressure and temperature data are averaged over the last 200 ms of each test. The end of the test is taken to be the time when the plenum pressures or the chamber pressure begin to drop. The analysis period for each measurement can be found in Appendix A for each test. The pressure and temperature values used in the subsequent calculations use the value averaged across the analysis window.

5.1 Propellant Mass Flow Rate

The mass flow rate of gaseous oxygen and methane is measured utilizing sonic orifices. Namely the pressure and temperature that is taken upstream and the pressure taken downstream of the sonic orifice.

The mass flow rate assuming isentropic, one-dimensional, choked flow, and ideal gas behavior the mass flow rate is given by

$$\dot{m} = \frac{Ap_0}{\sqrt{T_0}}\sqrt{\frac{\gamma}{R}}\frac{\gamma+1}{2}^{\frac{-\gamma-1}{2(\gamma-1)}}, \tag{5.1}$$

where A is the cross-sectional area, p_0 and T_0 are the total pressure and temperature, respectively, γ is the ratio of specific heats ($\gamma = c_\mathrm{p}/c_\mathrm{v}$), and R is the specific gas constant. However, the required pressure ranges of the working fluid dictate that the implementation of real gas effects are necessary. Accounting for real gas effects, the mass flow rate is written as

$$\dot{m} = \frac{C_\mathrm{d}AC^*p_0}{\sqrt{RT_0}}, \tag{5.2}$$

where C_d is the discharge coefficient and the critical flow factor, C^* is defined to be

$$C^* = \frac{\rho V\sqrt{RT_0}}{p_0}, \tag{5.3}$$

where V is the velocity of the gas.

The methodology outlined in [80] is followed to account for real-gas effects. An in-house python solver based on the work in [81, 82] is used to obtain mass flow rates at a given upstream pressure, temperature, throat diameter, and discharge coefficient. The code performs an iterative enthalpy and continuity balance between the upstream and throat locations to determine the throat thermodynamic state for a given upstream state assuming that the flow is sonic at the throat.

Together, the mass flow rates of the fuel and the oxidizer are used to define the equivalence ratio (ϕ) and the total propellant mass flux (ψ). The total mass flux is given as

$$\psi = \frac{(\dot{m}_{\text{fuel}} + \dot{m}_{\text{ox}})}{A_{\text{chamber}}}, \tag{5.4}$$

where $\dot{m}_{\text{fuel}}$ and $\dot{m}_{\text{ox}}$ are the mass flow rates of the fuel and oxidizer, respectively, and A_{chamber} is the cross sectional area of the chamber. The equivalence ratio is given by

$$\phi = \frac{\frac{\dot{m}_{\text{fuel}}}{\dot{m}_{\text{ox}}}}{\left(\frac{\dot{m}_{\text{fuel}}}{\dot{m}_{\text{ox}}}\right)_{\text{stoic}}}. \tag{5.5}$$

5.2 Coolant Mass Flow Rate

To determine the average heat flux distribution along the outer wall of the combustion chamber, the mass flow rate through the cooling channel is first determined. Pressure and temperature at each outlet is used to determine the mass flow rate associated with each of the cooling channels as

$$\dot{m}_n = C_{\text{d}_n} A_n \sqrt{\frac{2\rho_n(p_{1_n} - p_{\text{atm}})}{1 - \beta_n^4}}, \tag{5.6}$$

where $\beta_n = D_{2_n}/d_1$, d_1 is the upstream tube diameter, D_{2_n} is the orifice throat diameter, A_n is the orifice throat area, C_{d_n} is the discharge coefficient of the respective cooling channel from Table 4.1, p_{1_n} is the coolant pressure immediately upstream of the orifice, p_{atm} is the atmospheric pressure directly downstream of the outlet orifice, and ρ_n is the density upstream of the orifice for a given

cooling channel n. This density is determined by using the CoolProp open-source thermophysical property library [78].

5.3 Heat Flux

This mass flow rate is then used to determine the average heat that is convected out of the channels by the cooling water. Using this mass flow rate, the average convected heat flux can be written as

$$\dot{q}'' = \frac{\dot{m}c(T_{\text{out}} - T_{\text{in}})}{A_{\text{hot}}}, \tag{5.7}$$

where the specific heat capacity c is taken at the coolant channel average temperature, T_{in} is the coolant temperature taken immediately upstream of the hardware, and T_{out} is the coolant temperature taken immediately downstream of the hardware. Here, A_{hot} is taken to be the hot side are of the internal cooling channel.

Through the water flow calibration, the internal geometry of the AM channels exhibited adverse effects on the distribution of coolant mass flow through the channels. Particularly, the cooling channels in line with the inlet tubing where the outlet is 180° off of the inlet (stations 2, 5, and 7) provide around twice as much coolant mass flow than the other channels (see Fig. 5.1). This large variation in mass flow rates results in the adiabatic assumption between adjacent channels not being applicable, as this approach neglects the fact that heat is transferred between channels.

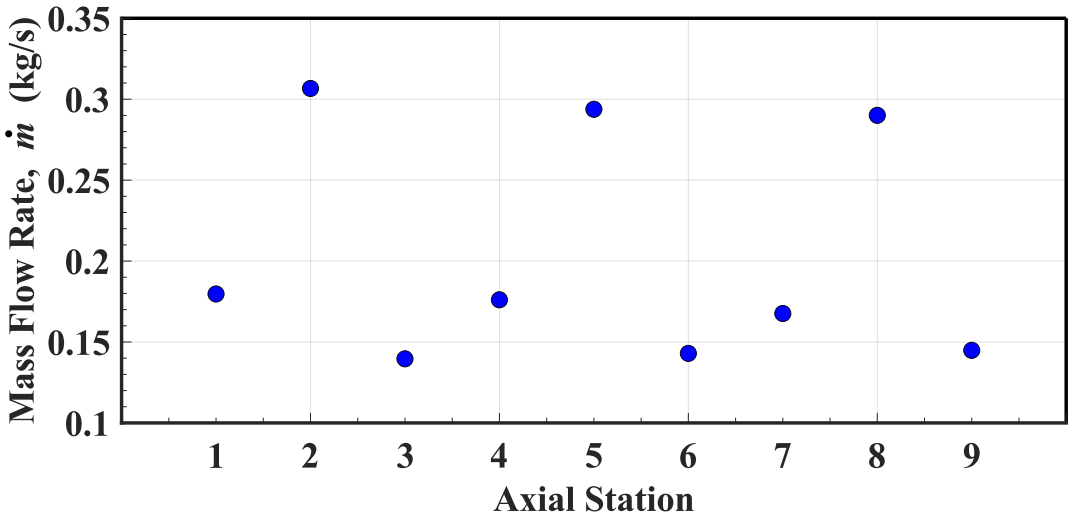


Figure 5.1: Coolant mass flow rate at each of the nine stations.

To better represent the heat flux for this system, $\dot{q}$" is calculated by using an approach that accounts for heat being conducted between channels. In this model, the channel wall facing the ambient environment is taken to be adiabatic, where $(\dot{q}_{\mathrm{h}})_{n-1}$, $\dot{q}_{\mathrm{h}_n}$, and $(\dot{q}_{\mathrm{h}})_{n+1}$ represent the heat flux distribution along the combustor wall (see Fig. 5.2 (b)). Inter-channel heat transfer is then represented via conduction through the wall separating each of the channels. For a given channel, n, the net heat flux into the cooling channel, $\dot{q}_{\mathrm{tot}_n}$, is

$$(\dot{q}_{\mathrm{tot}})_n = \dot{q}_{n,n-1} + (\dot{q}_{\mathrm{h}})_n + \dot{q}_{n,n+1}, \tag{5.8}$$

where $(\dot{q}_{\mathrm{h}})_n$ is the heat transfer rate from the hot wall of the combustion chamber, and $\dot{q}_{n,n+1}$ and $\dot{q}_{n,n-1}$ are the rates of heat transferred by the adjacent channels to the right and left, respectively.

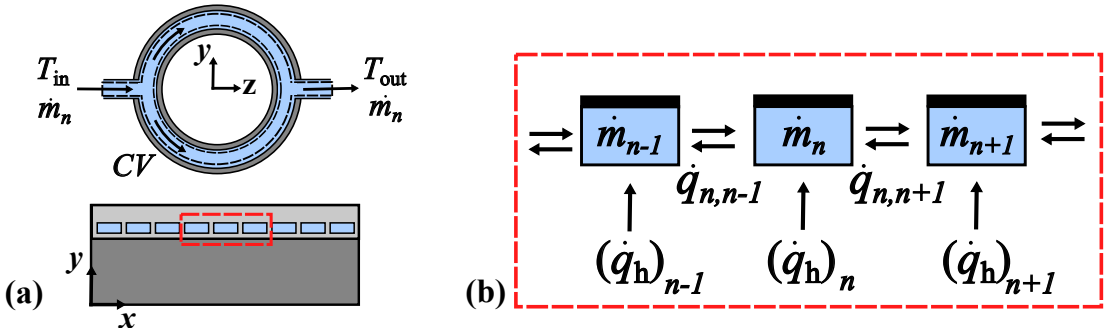


Figure 5.2: Schematic of (a) channel geometry control volume and (b) heat transfer model for determining chamber heat flux.

Rearranging Eq. (5.8) to solve for $(\dot{q}_h)_n$, the heat transferred to the combustor wall becomes

$$(\dot{q}_h)_n = \dot{m}_n c \Delta T_n - \kappa A_{side} \Delta T_{n,n-1}/d - \kappa A_{side} \Delta T_{n,n+1}/d, \tag{5.9}$$

where $\dot{m}_n$ is the mass flow rate calculated using Eq. (2.6), κ is the thermal conductivity of GRCop-42 [70] evaluated at the average temperature between the relevant adjacent channels, ΔT_n is the temperature difference between the inlet and the outlet of a channel n, $\Delta T_{n,n\pm1}$ is the temperature difference between a given channel and its adjacent channels, A_{side} is the side wall area of the cooling channel, and d is the distance between adjacent cooling channels. Finally, the heat flux for a given axial station, $\dot{q}''_n$, is given by

$$\dot{q}''_n = \frac{(\dot{q}_h)_n}{A_{hot}}, \tag{5.10}$$

where A_{hot} is the cooling channel hot wall area. This model is implemented to determine heat flux for axial stations $2 - 8$.

5.4 Wave Dynamics

The wave dynamics for the hot fire testing are determined by performing an automated image processing on the aft-end high speed video data. To do the processing, an in-house python solver is used based on the work of Bennewitz et al. [83]. The high speed video data taken during the same analysis window that the pressure and temperature measurements are taken is used to perform the image analysis. Starting with the raw image (Fig. 5.3 (a)), a background subtraction is initially performed to accentuate the difference between the location of the detonation front and the background (Fig. 5.3 (b)). A cartesian mesh is created to enable the annulus to be located in the field of view (Fig. 5.3 (c)). A Fourier transform is performed on the temporal history of the pixel intensities of each cell, and a circle is fitted to the cells with the top 100 amplitudes (Fig. 5.3 (d)). Once the annulus is located, a new polar mesh is created (Fig. 5.3 (e)). The pixel intensity for each bin for a frame is plotted in a detonation surface for the entirety of the analysis window. The detonation surface (Fig. 5.4) displays the pixel intensity variation with respect to circumferential location in the annulus and time. Finally, a 2-D fast-Fourier transform is performed on the detonation surface to extract the wave speed and operating frequency for each test.

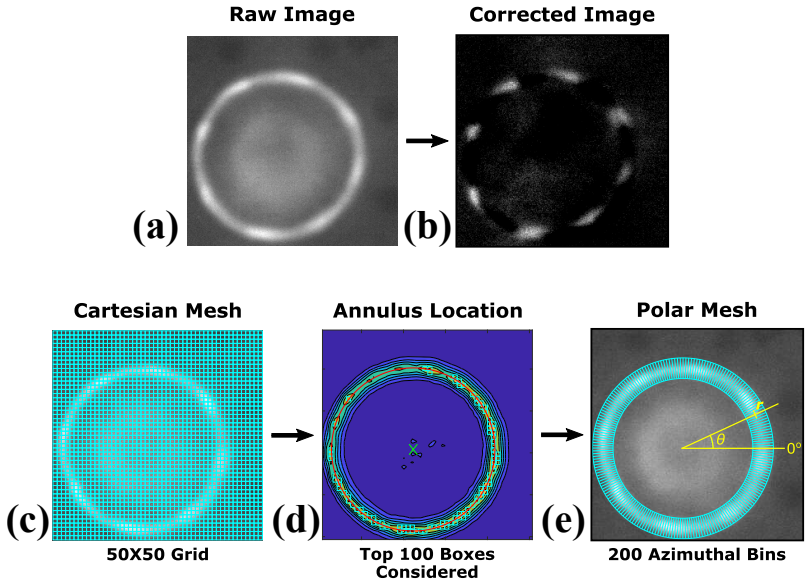


Figure 5.3: Image processing procedure with (a) raw image, (b) background subtraction, (c) cartesian mesh, (d) annulus circle fit, and (e) polar mesh (reproduced and edited from [83]).

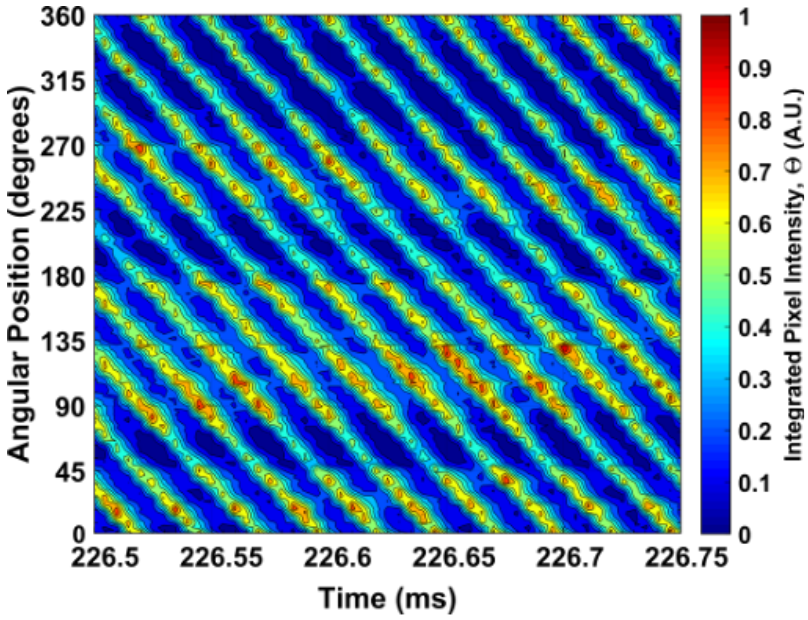


Figure 5.4: Corresponding detonation surface (reproduced and edited from [83]).

5.5 Uncertainty Analysis

The uncertainty analysis for this thesis follows the methodology outlined in the Guide to the Expression of Uncertainty in Measurement [84]. Therein, uncertainty is categorized into two groups: Type A and Type B uncertainty. Type A uncertainty is defined as statistical uncertainty in a measured quantity, while Type B uncertainty is defined as that which is determined by methods other than statistical analysis.

The measurements in this thesis are taken to be an average of a given quantity (e.g., pressure, temperature, or thrust) over the duration of the analysis window. For a given measurement y where N samples are taken, the average is defined as

$$y = \frac{1}{N}\sum_{i=1}^{N} y_i. \tag{5.11}$$

For these measurements, the Type A statistical uncertainty is taken to be the standard deviation of the mean (s_y) over the given analysis window given as

$$s_y^2 = \frac{\sum_{i=1}^{N}(y_i - y)^2}{N(N-1)}, \tag{5.12}$$

and the degrees of freedom is taken to be $N - 1$.

If the determined quantity y is a function of i measurements such that

$$y = f(x_1, x_2, ..., x_i), \tag{5.13}$$

where f is the function used to determine y, then the uncertainty in y is quantified using the law of propagation of uncertainty. With this method, a Taylor series expansion is performed about the input to determine the standardized uncertainty in y. Through this, it can be shown that the general form of the standard uncertainty in y (u_y) is given by

$$u_y^2 = \sum_{i=1}^{N} \frac{\partial f}{\partial x_i} u_{x_i} + 2 \sum_{i=1}^{n-1} \sum_{j=i+1}^{n} \left(\frac{\partial f}{\partial x_i} \right) \left(\frac{\partial f}{\partial x_j} \right) u_{x_i} u_{x_j} r(x_i, x_j), \tag{5.14}$$

where u_{x_i} is the standard uncertainty of input x_i and $r(x_i, x_j)$ is the correlation coefficient between the inputs x_i and x_j. The correlation coefficient $r(x_i, x_j)$ is given by

$$r(a, b) = \frac{\sum_{i=1}^{N} (a_i - \bar{a})(b_i - \bar{b})}{\sqrt{\sum_{i=1}^{N} (a_i - \bar{a})^2 \sum_{i=1}^{N} (b_i - \bar{b})^2}}, \tag{5.15}$$

where $\bar{a}$ and $\bar{b}$ are the average values as defined in Eq. (5.11). This value can represent negative correlation ($r = -1$), no correlation ($r = 0$), or positive correlation ($r = 1$) between a and b. Assuming that the inputs are uncorrelated causes Eq. (5.14) to reduce to

$$u_y^2 = \sum_{i}^{N} \left(\frac{\partial f}{\partial x_i} u_{x_i} \right)^2. \tag{5.16}$$

When using the law of propagation of uncertainty, the effective degrees of freedom of y (ν_{eff}) must be determined using the Welch-Satterthwaite equation, given as

$$\nu_{\text{eff}}(y) = \frac{u_y^4}{\sum_{i=1}^{n} \frac{u_{y,i}^4}{\nu_i}}, \tag{5.17}$$

where $u_{y,i}$ is the partial derivative term and the uncertainty term given in Eq. (5.16) as

$$u_{y,i} = \frac{\partial f}{\partial x_i} u_{x_i}. \tag{5.18}$$

From the standard uncertainty of a given measurement (u_y) and the associated Effective Degrees of Freedom (ν_{eff}), the expanded uncertainty is determined. This is done through the use of the coverage factor (k), as follows

$$U_{95\%} = k_{95\%} u_y, \tag{5.19}$$

where $k_{95\%}$ is determined through the Student's t-distribution table corresponding to the 95% confidence and the Effective Degrees of Freedom of the given measurement. The uncertainty reported in this thesis is this expanded uncertainty ($y \pm U_{95\%}$). All measurements presented are derived from either pressure or temperature and are divided into two main categories: coolant and propellant. Ultimately, the pressure and temperature measurements associated with the cooling water are used to determine heat flux in the engine. Pressure and temperature of the oxygen and the fuel are used to determine the operational condition (i.e., equivalence ratio ϕ and total mass flux, ψ). The uncertainty in the pressure and temperature measurements are propagated through the equations listed in each of the respective sections using the law of propagation of uncertainty.

5.5.1 Pressure Measurement Uncertainty

For the subsequent analysis, absolute pressures are necessary. Due to the fact that the pressures recorded through the pressure transducers are gauge pressures, they first must be converted into absolute pressures. The absolute pressure p_{abs} is given by

$$p_{\text{abs}} = p_{\text{g}} + p_{\text{atm}}, \tag{5.20}$$

where p_{abs} is the recorded gauge pressure and p_{atm} is the atmospheric pressure.

Using Eq. (5.16), the uncertainty in the absolute pressure $u_{p_{\text{abs}}}$ is given by

$$u_{p_{\text{abs}}}^2 = u_{p_{\text{g}}}^2 + u_{p_{\text{atm}}}^2, \tag{5.21}$$

where $u_{p_{\text{g}}}$ is the standard uncertainty of the gauge pressure and $u_{p_{\text{atm}}}$ is the standard uncertainty of the atmospheric pressure.

The atmospheric pressure is measured using a Bosch BMP280 pressure sensor integrated into the iPhone 8+ and recorded using the Barometer & Altimeter application to obtain a time history of atmospheric pressure throughout the day of testing. The accuracy and resolution of the sensor as stated by the manufacturer is 1 hPa and 0.01 hPa, respectively. This implies that the equation used to determine the atmospheric pressure is

$$p_{\text{atm}} = p_{\text{recorded}} + \epsilon_{\text{acc}} + \epsilon_{\text{res}}, \tag{5.22}$$

where p_{recorded} is the pressure recorded by the sensor and ϵ_{acc} and ϵ_{res} are the sensor's accuracy and resolution, respectively. The associated standard uncertainty is given by

$$u_{p_{\text{atm}}} = u_{p_{\text{recorded}}} + u_{\epsilon_{\text{acc}}} + u_{\epsilon_{\text{res}}}, \tag{5.23}$$

where $u_{p_{\text{recorded}}}$ is the time weighted standard deviation, $u_{\epsilon_{\text{acc}}} = 1 \text{ hPa}/\sqrt{3}$, and $u_{\epsilon_{\text{res}}} = 0.01 \text{ hPa}/\sqrt{3}$.

Next, guage pressure uncertainty needs to be quantified. The pressure transducers used in this work are 4-20 mA Druck UNIK 5000 and Sensotec gauge pressure sensors. Calibrations are performed using a Mansfield & Greene Model Type T hydraulic deadweight tester. An unweighted least squares regression is performed on the data obtained through calibration, resulting in the equation of a line for the gauge pressure

$$p_{\text{g}} = mI + b, \tag{5.24}$$

where I is the measured current, m is the slope of the line, and b is the intercept. By performing the law of propagation of uncertainty on Eq. (5.24) and assuming a non-zero covariance between m and b, the standard uncertainty in the gauge pressure measurement is

$$u_{p_{\text{g}}}^2 = (mu_I)^2 + u_b^2 + (Iu_m)^2 + 2Iu_m u_b r(m,b), \tag{5.25}$$

where $r(m,b)$ is the correlation coefficient determined using Eq. (5.15), u_m is the standard uncertainty of the slope, and u_b is the standard uncertainty of the intercept. Because the pressure is recorded using an National Instruments data

acquisition system, the calibration coefficients are applied directly to the measured current. However, to recover the current I, Eq. (5.24) can be rearranged to solve for I.

After having found the standard uncertainties of the atmospheric pressure and the gauge pressure measurements, the uncertainties can be used in Eq. (5.21) to obtain the standard uncertainty of the absolute pressure measurements. This uncertainty is propagated through all subsequent calculations.

5.5.2 Temperature Uncertainty

All temperatures reported in this thesis are recorded with T-Type thermocouples using an NI PXIe-4353 measurement card. The temperature is determined by

$$T = T_{\text{recorded}} + \epsilon_{\text{amp}} + \epsilon_{\text{TC}}, \tag{5.26}$$

where T_{recorded} is the recorded temperature, ϵ_{amp} is the amplification uncertainty, including cold junction compensation, and ϵ_{TC} is the uncertainty intrinsic to the thermocouple itself. Thus, the standard uncertainty of a temperature measurement is given by

$$u_{\text{T}} = s_{T_{\text{recorded}}} + u_{\epsilon_{\text{amp}}} + u_{\epsilon_{\text{TC}}}, \tag{5.27}$$

where $s_{T_{\text{recorded}}}$ is the statistical uncertainty associated with the temperature measurement, $u_{\epsilon_{\text{amp}}}$ is the uncertainty associated with the amplification process, and $u_{\epsilon_{\text{TC}}}$ is the thermocouple inherent uncertainty.

The amplification uncertainty is calculated using the methods defined in the NI PXIe-4353 thermocouple measurement card's application manual [85]. Through instructions in this manual, the amplification uncertainty simultaneously accounts for many sub-components of uncertainty associated with the thermocouple amplification process.

5.5.3 Propellant Discharge Coefficient Uncertainty

The discharge coefficient is once again defined as the ratio of the actual mass flow rate divided by the ideal mass flow rate as in the case of the coolant. However, the methodology to obtain both the actual mass flow rate and the ideal mass flow rate differ. Thus, the discharge coefficient is given by

$$C_{\mathrm{d}} = f\left(\dot{m}_{\mathrm{actual}}, \dot{m}_{\mathrm{ideal}}\right), \tag{5.28}$$

where the ideal mass flow rate is a function of pressure, temperature, upstream and throat diameter, and the mass-specific gas constant of the flowing gas. The ideal mass flow rate is determined using the methodology outlined in Section 5.1 where the discharge coefficient is taken to be 1. Then the uncertainty associated with the discharge coefficient is given by

$$u_{C_{\mathrm{d}}}^2 = \left(\frac{\partial C_{\mathrm{d}_n}}{\partial \dot{m}_{\mathrm{actual}}} u_{\dot{m}_{\mathrm{actual}}}\right)^2 + \left(\frac{\partial C_{\mathrm{d}_n}}{\partial \dot{m}_{\mathrm{ideal}}} u_{\dot{m}_{\mathrm{ideal}}}\right)^2, \tag{5.29}$$

and evaluating the partial derivatives of Eq. (5.28), the standard uncertainty in the propellant mass flow rate is given by

$$u_{C_{\mathrm{d}_n}}^2 = \left(\frac{u_{\dot{m}_{\mathrm{actual}}}}{\dot{m}_{\mathrm{ideal}}}\right)^2 + \left(-\frac{\dot{m}_{\mathrm{actual}}}{\dot{m}_{\mathrm{ideal}}^2} u_{\dot{m}_{\mathrm{actual}}}\right)^2. \tag{5.30}$$

First, the actual mass flow rate $\dot{m}_{\mathrm{actual}}$, is determined through calibration of sonic orifices. The actual mass flow rate is determined by using a Emerson Micro Motion ELITE Coriolis Meter (model CMFS025P) to provide the independent actual mass flow measurement. Using this method, the sonic orifices are calibrated in house by obtaining N calibration points by raising and lowering the pressure upstream of the orifice. Upstream and downstream pressures are measured during the calibration process to confirm that the flow is choked across the orifice. Using this method the uncertainty of the actual mass flow rate $u_{\dot{m}_{\mathrm{actual}}}$ is given by

$$u_{\dot{m}_{\mathrm{actual}}}^2 = u_{\mathrm{bias}}^2 + u_{\mathrm{reading}}^2, \tag{5.31}$$

where u_{bias} is the manufacturer stated bias. Also, u_{reading} is given by

$$u_{\mathrm{reading}}^2 = u_{\mathrm{acc}}^2 + u_{\mathrm{rep}}^2 + u_{\mathrm{res}}^2, \tag{5.32}$$

where u_{acc}, u_{rep}, and u_{res} are the manufacturer stated accuracy, repeatability, and resolution uncertainties, respectively. With this, the actual mass flow rate and associated uncertainty can be used in Eq. (5.30).

The uncertainty in ideal mass flow rate is given by

$$u_{\dot{m}_{\text{ideal}}}^2 = \left(\frac{\partial \dot{m}_{\text{ideal}}}{\partial p} u_p\right)^2 + \left(\frac{\partial \dot{m}_{\text{ideal}}}{\partial T} u_T\right)^2 + u_{\text{num}}^2, \tag{5.33}$$

where the partial derivatives are approximated numerically using a central difference scheme, and u_{num} is the resulting uncertainty due to the numerical tolerance. With these components, the standard uncertainty of the discharge coefficient u_{C_d} can be calculated and propagated through subsequent uncertainty calculations.

5.5.4 Propellant Mass Flow Rate Uncertainty

The propellant mass flow rates determined in Section 5.1 are a function of pressure, temperature, upstream and throat diameters, and the mass-specific gas constant:

$$\dot{m} = f\left(C_\text{d}, p, T, D, d, R_i\right). \tag{5.34}$$

Here, the uncertainty of the mass-specific gas constant R_i is taken to be zero. Additionally, because the discharge coefficient is calibrated in the same flow system setup as is used in testing, the diameters (d and D) are also assumed to have no additional uncertainties. This means the uncertainties left to be accounted for are those associated with the discharge coefficient, pressure, and temperature.

This yields that the uncertainty in the mass flow rate can be found by

$$u_{\dot{m}}^2 = \left(\frac{\partial \dot{m}}{\partial C_\text{d}} u_{C_\text{d}}\right)^2 + \left(\frac{\partial \dot{m}}{\partial p} u_p\right)^2 + \left(\frac{\partial \dot{m}}{\partial T} u_T\right)^2 + u_{\text{num}}^2, \tag{5.35}$$

where the partial derivatives are approximated numerically using a central difference scheme, and u_{num} is the resulting uncertainty due to the numerical tolerance. Also, the uncertainties of pressure and temperature are evaluated using the methodology outlined in the previous sections.

5.5.5 Equivalence Ratio and Total Mass Flux Uncertainty

Uncertainty components for the fuel and oxygen mass flow rates found in the previous two sections culminate in the calculation of the equivalence ratio (ϕ) and the total mass flux (ψ). As discussed in Section 5.1, the equivalence ratio given by

$$\phi = f(\dot{m}_{\text{fuel}}, \dot{m}_{\text{ox}}, s), \tag{5.36}$$

is a function of the fuel mass flow rate $\dot{m}_{\text{fuel}}$, oxygen mass flow rate $\dot{m}_{\text{ox}}$, and s, the stoichiometric coefficient for methane-oxygen combustion. The stoichiometric coefficient is taken as a constant having an uncertainty of zero leaving the two sources of uncertainty as the propellant mass flow rates. The combined uncertainty for equivalence ratio is then given by

$$u_\phi^2 = \left(\frac{u_{\dot{m}_{\text{fuel}}}}{\dot{m}_{\text{ox}} s}\right)^2 + \left(-\frac{\dot{m}_{\text{fuel}}}{\dot{m}_{\text{ox}}^2 s} u_{\dot{m}_{\text{ox}}}\right)^2, \tag{5.37}$$

where the uncertainties associated with the fuel and oxygen mass flow rates are determined through the methodology outlined in the previous sections.

Next, the total mass flux, given by

$$\psi = f(\dot{m}_{\text{fuel}}, \dot{m}_{\text{ox}}, A_{\text{chamber}}), \tag{5.38}$$

is a function of the fuel mass flow rate $\dot{m}_{\text{fuel}}$, oxygen mass flow rate $\dot{m}_{\text{ox}}$, and A_{chamber}, the cross sectional area of the chamber that is taken to be a constant with zero uncertainty. Thus, the standard uncertainty of the total mass flux ψ is given by

$$u_{\psi}^2 = \left(\frac{u_{\dot{m}_{\text{fuel}}}}{A_{\text{chamber}}}\right)^2 + \left(\frac{u_{\dot{m}_{\text{ox}}}}{A_{\text{chamber}}}\right)^2, \tag{5.39}$$

where the uncertainties in mass flow rate are the same as those used in the determination of equivalence ratio.

Finally, the uncertainty reported in the results section is the 95% confidence expanded uncertainty, which is written as the following:

$$U_{95\%,\phi} = k_{95\%} u_{\phi}, \tag{5.40}$$

and

$$U_{95\%,\psi} = k_{95\%} u_{\psi}. \tag{5.41}$$

5.5.6 Coolant Discharge Coefficient Uncertainty

The discharge coefficient is a function of ideal mass flow rate and the theoretical isentropic mass flow rate (Eq. 5.42), which has the form

$$C_{\text{d}_n} = f\left(\dot{m}_{\text{actual}}, \dot{m}_{\text{ideal}}\right). \tag{5.42}$$

Using the Taylor series method of uncertainty propagation, the standard uncertainty of the discharge coefficient can be expressed as

$$u_{C_{\mathrm{d}_n}}^2 = \left(\frac{\partial C_{\mathrm{d}_n}}{\partial \dot{m}_{\mathrm{actual}}} u_{\dot{m}_{\mathrm{actual}}}\right)^2 + \left(\frac{\partial C_{\mathrm{d}_n}}{\partial \dot{m}_{\mathrm{ideal}}} u_{\dot{m}_{\mathrm{ideal}}}\right)^2, \tag{5.43}$$

where evaluation of the partial derivatives yields

$$u_{C_{\mathrm{d}_n}}^2 = \left(\frac{u_{\dot{m}_{\mathrm{actual}}}}{\dot{m}_{\mathrm{ideal}}}\right)^2 + \left(-\frac{\dot{m}_{\mathrm{actual}}}{\dot{m}_{\mathrm{ideal}}^2} u_{\dot{m}_{\mathrm{actual}}}\right)^2. \tag{5.44}$$

In the case of the cooling water, actual mass flow rate is determined through a catch-and-weigh procedure allowing the calculation of actual mass flow rate as the total mass accumulated divided by the allotted test time, i.e., $\dot{m} = \Delta m/\Delta t$. Partial derivatives of this equation give the uncertainty of the actual mass flow rate as

$$m_{\dot{m}_{\mathrm{actual}}}^2 = \left(\frac{\partial \dot{m}_{\mathrm{actual}}}{\partial m} u_m\right)^2 + \left(\frac{\partial \dot{m}_{\mathrm{actual}}}{\partial t} u_t\right)^2, \tag{5.45}$$

where the uncertainty in mass caught u_m and recorded time u_t is taken to be the resolution of the scale and the stopwatch, respectively. Evaluating the partial derivatives yields:

$$u_{\dot{m}_{\mathrm{actual}}}^2 = \left(\frac{u_m}{t}\right)^2 + \left(-\frac{m}{t^2} u_t\right)^2. \tag{5.46}$$

Next, the uncertainty of the ideal mass flow rate is given by equation Eq. (5.6) without the discharge coefficient term. This leaves mass flow rate as a function of density and pressure, which allows the uncertainty to be determined

by

$$u_{\dot{m}_{\text{ideal}}}^2 = \left(\frac{\partial \dot{m}_{\text{ideal}}}{\partial \rho} u_\rho\right)^2 + \left(\frac{\partial \dot{m}_{\text{ideal}}}{\partial p_g} u_{p_g}\right)^2, \tag{5.47}$$

where the partial derivatives of $\dot{m}_{\text{ideal}}$ with respect to density and pressure are given by

$$\frac{\partial \dot{m}_{\text{ideal}}}{\partial \rho} = \frac{\pi\sqrt{2}}{8} \frac{D_2^2 p_g}{(1-\beta_n^4)\sqrt{\frac{\rho_n p_g}{1-\beta_n^4}}}, \tag{5.48}$$

and

$$\frac{\partial \dot{m}_{\text{ideal}}}{\partial p_g} = \frac{\pi\sqrt{2}}{8} \frac{D_2^2 \rho}{(1-\beta_n^4)\sqrt{\frac{\rho_n p_g}{1-\beta_n^4}}}. \tag{5.49}$$

The density ρ, is a function of temperature and absolute pressure. Thus, the uncertainty of density u_ρ is given by

$$u_\rho^2 = \left(\frac{\partial \rho}{\partial T} u_T\right)^2 + \left(\frac{\partial \rho}{\partial p_{\text{abs}}} u_{p_{\text{abs}}}\right)^2, \tag{5.50}$$

where the partial derivative of density with respect to pressure and temperature are evaluated using CoolProp [78] and the uncertainties of pressure and temperature are evaluated as outlined in previous sections.

The pressure uncertainty in Eq. (5.47) are gauge pressure measurements. This is due to the fact that the pressure differential in Eq. (5.6) is between an absolute pressure and the atmospheric pressure. By the definition of absolute pressure, this reduces to the gauge pressure measurement:

$$p_{abs} - p_{atm} = (p_g + p_{atm}) - p_{atm} = p_g. \tag{5.51}$$

As a result, the atmospheric uncertainty component would also cancel out, meaning the pressure uncertainty in Eq. (5.47) can be determined through Eq. (5.25).

With the uncertainties of the discharge coefficients $u_{C_{\mathrm{d}_n}}$, an uncertainty weighted average ($\widehat{\mu}_y$) is performed across the range of calibration set pressures given by

$$\widehat{\mu}_{C_{\mathrm{d}}} = \frac{\sum_i \frac{C_{\mathrm{d}_i}}{u^2_{C_{\mathrm{d}_i}}}}{\sum_j \frac{1}{u^2_{C_{\mathrm{d}_j}}}}. \tag{5.52}$$

The uncertainty associated with each of the nine uncertainty-weighted average discharge coefficients can be found by:

$$u_{\widehat{\mu}_{C_{\mathrm{d}}}} = \sqrt{\frac{1}{\sum_i \frac{1}{U^2_{C_{\mathrm{d}_j}}}}} \tag{5.53}$$

This is taken to be the discharge coefficient and its associated uncertainty value to be carried through the subsequent calculations.

5.5.7 Coolant Mass Flow Rate Uncertainty

The coolant mass flow rate is calculated through the methodology outlined in Section 5.2 using Eq. (5.6), which is a function of the following:

$$\dot{m} = f\left(C_{\mathrm{d}}, D_2, D_1, \rho, p_1, p_2\right). \tag{5.54}$$

Assuming that the diameters are constant with zero uncertainty and that the two pressure terms reduce to the gauge pressure as outlined in the previous section, the equation for the uncertainty in coolant mass flow rate is

$$u_{\dot{m}}^2 = \left(\frac{\partial \dot{m}_n}{\partial C_{\mathrm{d}_n}} u_{C_{\mathrm{d}_n}}\right)^2 + \left(\frac{\partial \dot{m}_n}{\partial \rho_n} u_{\rho_n}\right)^2 + \left(\frac{\partial \dot{m}_n}{\partial p_1} u_{p_g}\right)^2. \tag{5.55}$$

Evaluating the partial derivatives yields:

$$\frac{\partial \dot{m}_n}{\partial C_{\mathrm{d}_n}} = \frac{\pi}{4} D^2 \sqrt{\frac{2\rho_n p_g}{1-\beta_n^4}}, \tag{5.56}$$

$$\frac{\partial \dot{m}_n}{\partial \rho_n} = \frac{\pi\sqrt{2}}{8} \frac{C_{\mathrm{d}} D^2 p_g}{(1-\beta_n^4)\sqrt{\frac{\rho_n p_g}{1-\beta_n^4}}}, \tag{5.57}$$

and

$$\frac{\partial \dot{m}_n}{\partial p_1} = \frac{\pi\sqrt{2}}{8} \frac{C_{\mathrm{d}} D^2 \rho_n}{(1-\beta_n^4)\sqrt{\frac{\rho_n p_g}{1-\beta_n^4}}}. \tag{5.58}$$

The methodology for obtaining the uncertainties associated with the discharge coefficient $u_{C_{\mathrm{d}_n}}$, the density u_{ρ_n}, and the gauge pressures u_{p_g} are outlined in previous sections.

5.5.8 Heat Flux Uncertainty

Finally, given the standard uncertainty components outlined in Sections 5.5.6 and 5.5.7, the uncertainty associated with the heat flux is determined. The uncertainty in heat flux $u_{\dot{q}''_n}$ is simply the uncertainty in the heat transfer rate for a given axial station $u_{(\dot{q}_\mathrm{h})_n}$ divided by the hot side channel area A_hot. The heat transfer rate, given by

$$(\dot{q}_\mathrm{h})_n = f(\dot{m}, c, \Delta T_n, \Delta T_{n,n-1}, \Delta T_{n,n-1}), \tag{5.59}$$

is a function of coolant mass flow rate $\dot{m}$, coolant heat capacity c, and three temperature deltas $(\Delta T_n, \Delta T_{n,n-1}, \Delta T_{n,n-1})$. Once again, applying the law of propagation of uncertainty on Eq. (5.9) yields the following,

$$\begin{aligned} u^2_{(\dot{q}_\mathrm{h})_n} = &\left(\frac{\partial(\dot{q}_\mathrm{h})_n}{\partial \dot{m}} u_{\dot{m}}\right)^2 + \left(\frac{\partial(\dot{q}_\mathrm{h})_n}{\partial c} u_c\right)^2 + \left(\frac{\partial(\dot{q}_\mathrm{h})_n}{\partial \Delta T_n} u_{\Delta T_n}\right)^2 \\ &+ \left(\frac{\partial(\dot{q}_\mathrm{h})_n}{\partial \Delta T_{n,n-1}} u_{\Delta T_{n,n-1}}\right)^2 + \left(\frac{\partial(\dot{q}_\mathrm{h})_n}{\partial \Delta T_{n,n+1}} u_{\Delta T_{n,n+1}}\right)^2, \end{aligned} \tag{5.60}$$

and evaluation of the partial derivatives simplifies Eq. (5.60) to

$$\begin{aligned} u^2_{(\dot{q}_\mathrm{h})_n} = &\left(c \Delta T_n u_{\dot{m}}\right)^2 + \left(\dot{m} \Delta T_n u_c\right)^2 + \left(\dot{m} c u_{\Delta T_n}\right)^2 \\ &+ \left(\frac{\kappa A_\mathrm{side}}{d} u_{\Delta T_{n,n-1}}\right)^2 + \left(\frac{\kappa A_\mathrm{side}}{d} u_{\Delta T_{n,n+1}}\right)^2, \end{aligned} \tag{5.61}$$

where the uncertainties in the temperature differentials are given by summing and squaring the respective temperatures ($u^2_{\Delta T_n} = u^2_{\Delta T_n} + u^2_{\Delta T_o ut}$).

Lastly, upon determination of the standard uncertainty of heat flux $u_{\dot{q}''_n}$, the 95% expanded uncertainty of heat flux for a given channel n is given by

$$U_{95\%,\dot{q}''_n} = k_{95\%} u_{\dot{q}''_n}. \tag{5.62}$$

Chapter 6. Results

Hot fire tests are performed with both the straight centerbody and constricted centerbody configurations (Fig. 6.1).

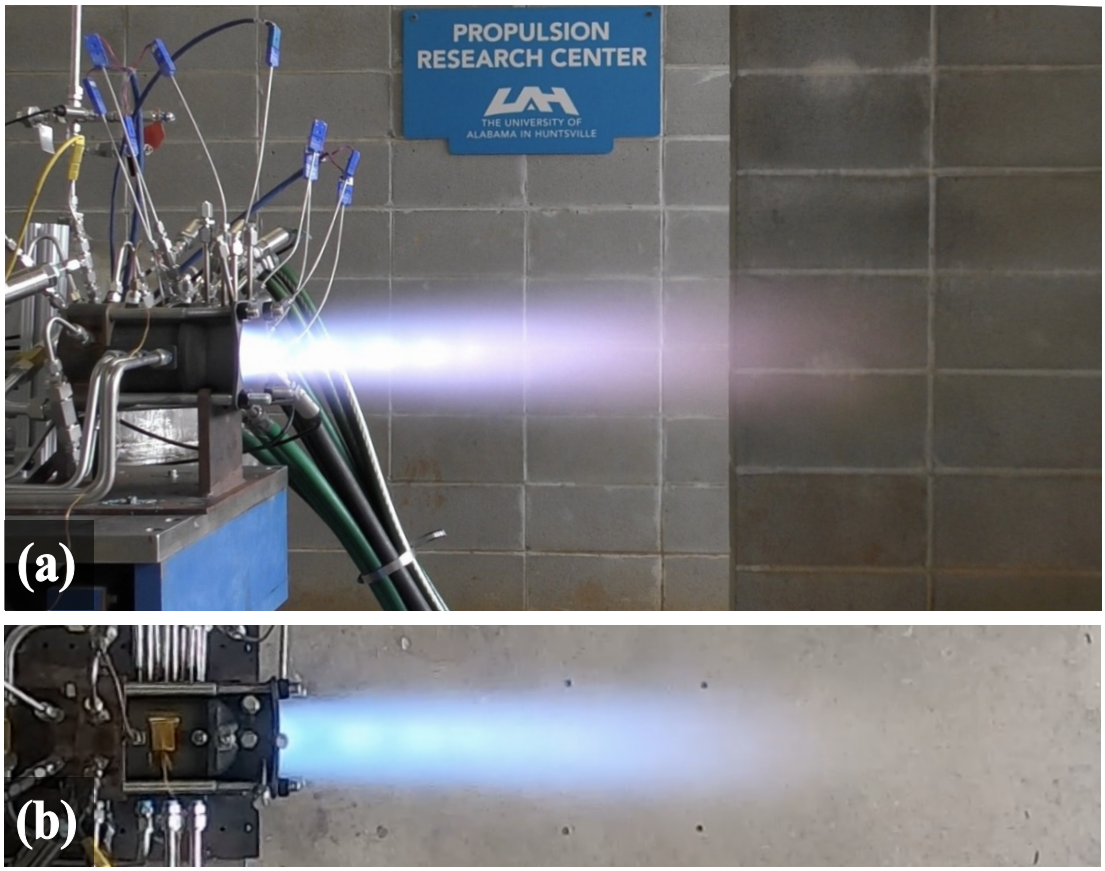


Figure 6.1: Images of (a) RDRE hot-fire side view and (b) RDRE hot-fire top-down view.

A mass flux sensitivity study is carried out by increasing the total propellant mass flux from $\psi = 103 - 310$ kg/m^2-s for a fixed equivalence ratio of $\phi = 1.1$ varying the propellant mass flux (Fig. 6.2 (a)). Overall, the axial heat flux distribution is determined for a total of ten cases. Six set conditions are investigated with the water-cooled straight channel configuration with the total mass flux ranging from $\psi = 103 - 310$ kg/m^2-s. Four equivalent conditions are tested from $\psi = 103 - 240$ kg/m^2-s with the water-cooled constricted geometry configuration. A firing time of $t_b = 3.5$ s is considered for the water-cooled straight channel cases and a firing time of $t_b = 4.5$ s is considered for the water-cooled constricted geometry tests.

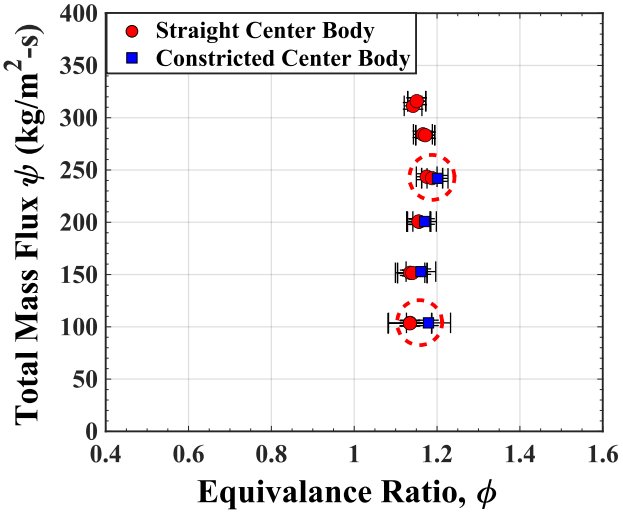


Figure 6.2: Operational map for hot fire testing.

Increased firing time allows for the engine hardware to reach thermal steady-state. Thermal steady-state of the hardware is assessed through the outlet coolant temperatures of the different axial stations (Fig. 6.3 (b)). Data from the

steady-state portion for each test (highlighted red in Fig. 6.3 (b)) is averaged over a 200 ms window that is used for the heat flux determination. As an example, during the $\psi = 241$ kg/m^2-s straight center body case, stations $2-8$ reach thermal steady-state after $t = 2.5$ s (Fig. 6.2 (b)). The first and last stations (1 and 9) adjacent wall temperatures are unknown, lack of adjacent cooling channels caused outlet temperatures to not reach thermal steady state, and contain the locally raised CTAP feature. Due to these reasons, the heat flux is not reported for stations 1 and 9.

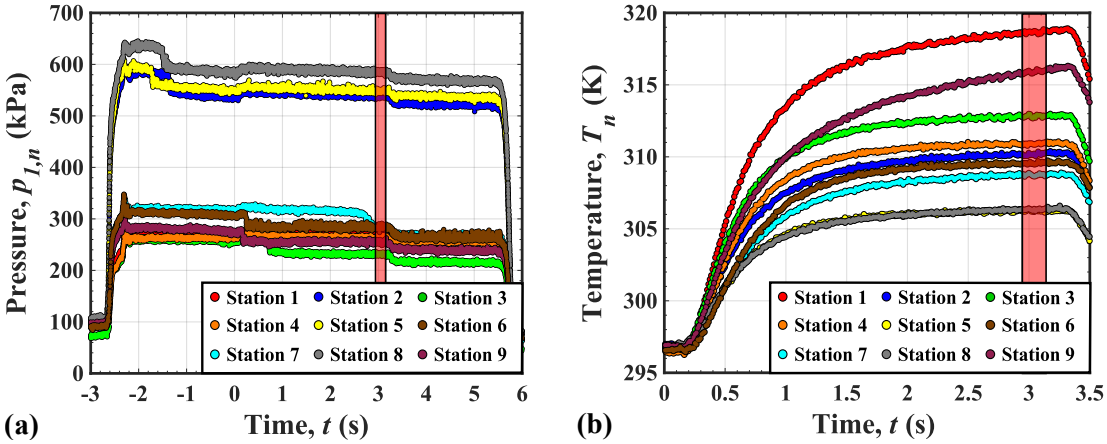


Figure 6.3: Coolant outlet (a) pressure response and (b) temperature response for $\psi = 241$ kg/m^2-s, $\phi = 1.1$ test.

To avoid transient responses in the cooling water mass flow rate, flow begins at $t =$ -3.0 s. For the duration of the analysis window, the cooling channel outlet pressure remains constant, implying a steady mass flow rate (Fig. 6.3 (a)). The temporal history of outlet pressure and temperature for each hot fire test can be found in Appendix A.

6.1 Heat Flux

For each hot fire test, heat flux is determined for 7 axial locations (x/L = 0.17-0.77). For comparison between the straight center body and the constricted center body configurations, a low mass flux ($\psi = 103$ kg/m^2-s) and high mass flux ($\psi = 240$ kg/m^2-s) case (circled in Fig. 6.2 (a)) are highlighted. The low mass flux case at $\psi = 103$ kg/m^2-s (Fig. 6.4 (a)), and the high mass flux case at $\psi = 240$ kg/m^2-s (Fig. 6.4 (b)), demonstrate an increase in heat flux loading as a function of total mass flow rate.

For the $\psi = 103$ kg/m^2-s case, heat flux ranges from $6.6 - 11.2$ MW/m^2 for the straight center body case and $11.7 - 15.3$ MW/m^2 for the constricted center body case. For both configurations, the heat flux at the station closest to the injector face is around 11 MW/m^2. Further downstream, the heat flux values for the two configurations diverge. There is a slight increase in spatial heat flux from $x/L = 0.2 - 0.6$ for the constricted center body case, most likely corresponding to the axial location of the detonation zone, with a maximum heat flux of 12.1 MW/m^2 for the low mass flux case. For the straight center body case the heat flux decreases with increasing axial length, where the maximum of 11.7 MW/m^2 occurring closest to the injector face. From $x/L = 0.55 - 0.80$, heat flux increases to 15.3 MW/m^2, corresponding to the axial location of the throat for the constricted center body case.

Similar trends are observed in the high mass flux case at $\psi = 240$ kg/m^2-s, where the heat flux ranges from $11.0 - 16.2$ MW/m^2 for the straight configuration

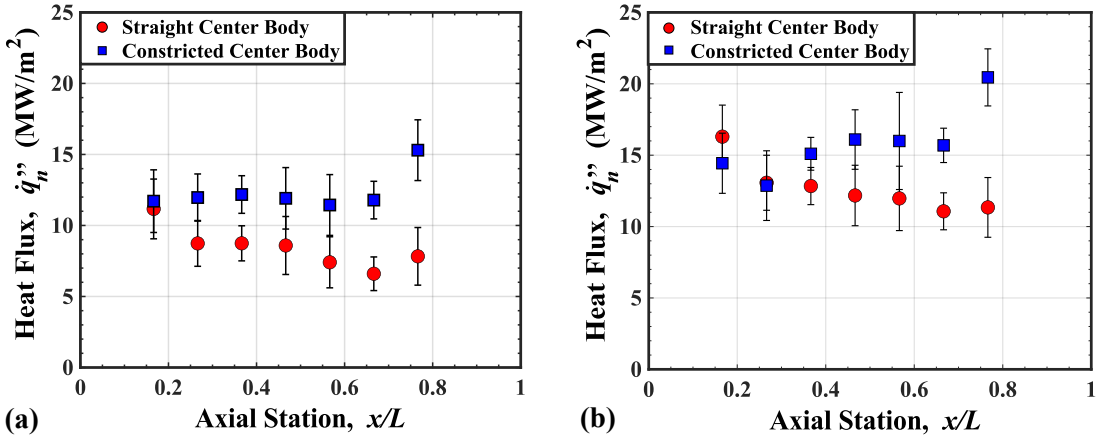


Figure 6.4: Axial heat flux distribution for (a) $\phi = 1.1$ and $\psi = 103$ kg/m^2-s and (b) $\phi = 1.1$ and $\psi = 240$ kg/m^2-s for both straight and constricted center bodies.

and $11.8 - 20.5$ MW/m^2 with the constricted geometry. Similarly to the low flux case, the heat flux at the two stations closest to the injector face are comparable before differing in behavior further downstream. The heat flux reaches a maximum of 16.2 MW/m^2 at $x/L = 0.27$ for the straight channel, a comparable trend to the low flux case. For the constricted geometry, the area of increased heat flux most likely corresponding to the detonation plane appears to be pushed further downstream ($x/L = 0.37 - 0.67$). This is likely due to an increased propellant mass flow rate. The heat flux increases to a local maximum of 16.0 MW/m^2 at $x/L = 0.57$. Once again, the heat flux increases as the combustion chamber area is decreases approaching the geometric throat.

6.1.1 Straight Center Body Configuration

As expected, the straight center body configuration results in lower heat flux overall compared to the constricted center body configuration for comparable

propellant mass flux in the straight chamber geometry, ranging from $6.6 - 16.3$ MW/m^2 (Fig. 6.5). Overall, the heat flux decreases with axial length for the straight center body cases, however, most cases experience a slight increase in heat flux between $x/L = 0.27 - 0.47$. Also, all cases (except for the highest flux case of $\psi = 310$ kg/m^2-s) exhibit an increase in heat flux at $x/L = 0.77$ despite the absence of a constriction. Additionally, the heat flux increases with mass flux such that the peak heat flux for the $\psi = 310$ kg/m^2-s case is 46% greater than the maximum heat flux of the $\psi = 103$ kg/m^2-s case. Finally, the heat flux at $x/L = 0.37$ for the straight center body is approximately 28% lower than the average heat flux of the constricted center body at the same location.

6.1.2 Constricted Center Body Configuration

Overall, the constricted center body geometry results in higher maximum heat flux loadings for all cases tested (Fig. 6.6). Across the four conditions, the heat flux varied from $11.4 - 20.5$ MW/m^2. For the $\psi = 240$ kg/m^2-s case, the maximum heat flux is 32% higher than the $\psi = 103$ kg/m^2-s case. Upon observing the general trend of the spatial heat flux distribution across mass flux cases, there is a sharp decrease and subsequent increase in $\dot{q}''_n$ around $x/L = 0.27$. This is followed by an area of increased heat flux from $x/L = 0.37 - 0.47$ before decreasing slightly at $x/L = 0.57$. This area most likely corresponds to the axial location of the detonation zone. Lastly, the heat flux begins to increase as the geometry constricts from $x/L = 0.67 - 0.77$ ending at a maximum of 20.5 MW/m^2 at the throat ($x/L = 0.77$). As mass flux is increased, the area of increased mass flux

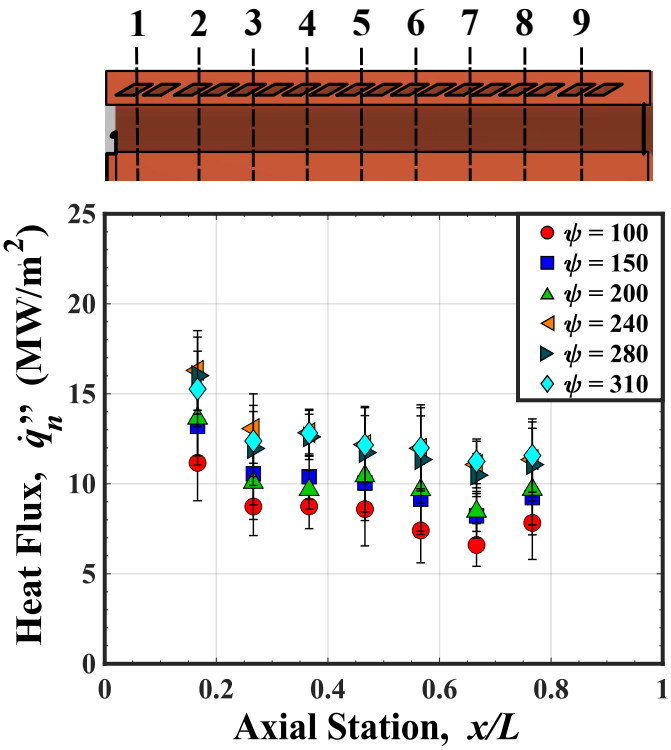


Figure 6.5: Axial heat flux distributions for the mass flux sensitivity study using the straight center body geometry.

increases in heat flux loading. For the constricted geometry cases, there is less variation between heat flux loads near the injection plane, where the heat flux variation between different mass flux conditions from $x/L = 0.17 - 0.27$ is nearly twice as much as the variation in heat flux after $x/L = 0.37$ for each condition. This is consistent with results seen by Micka et al. [48], demonstrating a difference in heat flux scaling near the injector compared to the flow expansion further downstream.

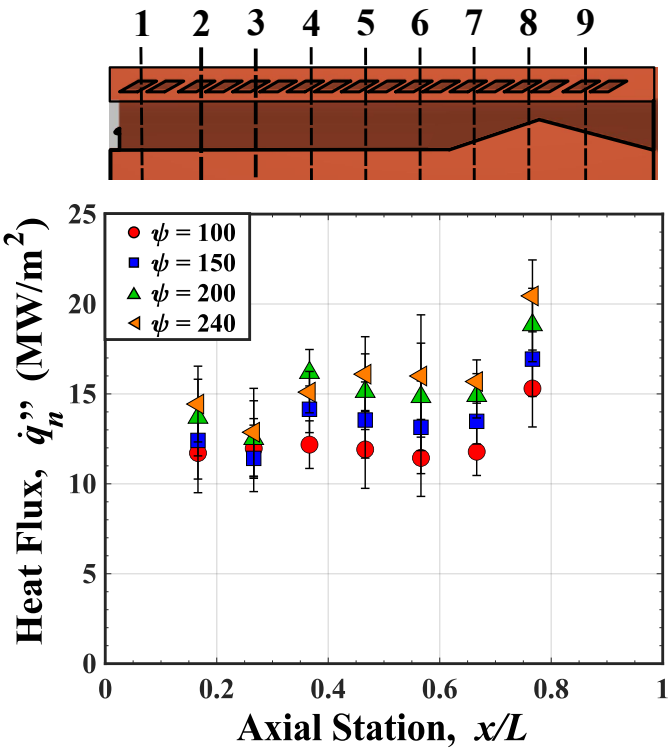


Figure 6.6: Axial heat flux distributions for the mass flux sensitivity study using the constricted center body geometries.

6.1.3 Heat Flux Scaling

For the straight and constricted center body configurations, sensitivity of heat flux to increasing mass flux at each axial station is investigated. For most axial locations, the heat flux increases linearly as total mass flux increases. At the station closest to the injector at $x/L = 0.17$, the heat flux for the constricted center body configuration follows closely with the trends observed for the straight center body configuration (Fig. 6.7 (a)). For the station located at $x/L = 0.47$ the combustor experiences higher heat flux overall. For the high mass flux ($\psi = 280 - 310$ kg/m^2-s) straight center body cases at both axial locations

the heat flux begins to decrease. Plots of heat flux with varying mass flux for each of the 7 stations reported can be found in Appendix B.

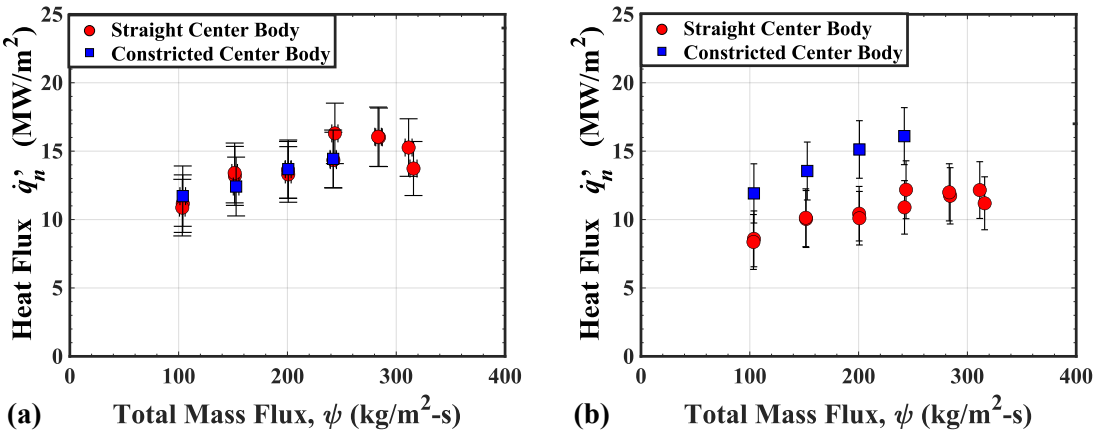


Figure 6.7: Heat flux with varying total mass flux for axial stations (a) two and (b) five.

To investigate how the heat flux scales with total mass flow rate, the results are compared ato the Bartz correlation (2.1). The driving scaling relationship in this correlation is that of local mass flux through the combustor which scales to the power of 0.8. Through methodology laid out by Micka et. al [48], a scaling study is performed using this relationship with total mass flow rate. Scaling with mass flux is equivalent to scaling with chamber pressure, or total mass flow rate, for the same combustor and propellants. To determine if the heat transfer data obtained scales with total mass flux, the local heat flux at a given station is normalized as

$$\dot{q}''_{n,s} = \frac{\dot{q}''_n}{\left(\frac{\dot{m}}{\dot{m}_{\text{ref}}}\right)^{\alpha}}, \tag{6.1}$$

to define the scaled heat flux ($\dot{q}''_{n,s}$) where $\dot{m}$ is the total mass flow rate for a given test, $\dot{m}_{\text{ref}}$ is taken to be the mass flow rate of the nominal mass flux case ($\psi = 100$ kg/m^2-s, $\dot{m}_{\text{ref}} = 0.145$ kg/s), $\dot{q}''_n$ is the heat flux for an axial station n, and α is a scaling factor ($\alpha = 0.8$ for Bartz correlation). If the Bartz correlation is applicable to this set of data, then the normalized data given by Eq. (6.1) should collapse on the same line. This is investigated using only the data from the straight center body configuration tests. Interestingly, when $\alpha = 0.8$, the heat flux data does not indicate that it scales with total mass flow rate to the 0.8 power (Fig. 6.8 (a)). However, the heat flux data collapses on itself when a value of $\alpha = 0.38$ is selected (Fig. 6.8 (b)). This implies that in this particular RDRE hardware the local heat flux scales with mass flux to the power of 0.38.

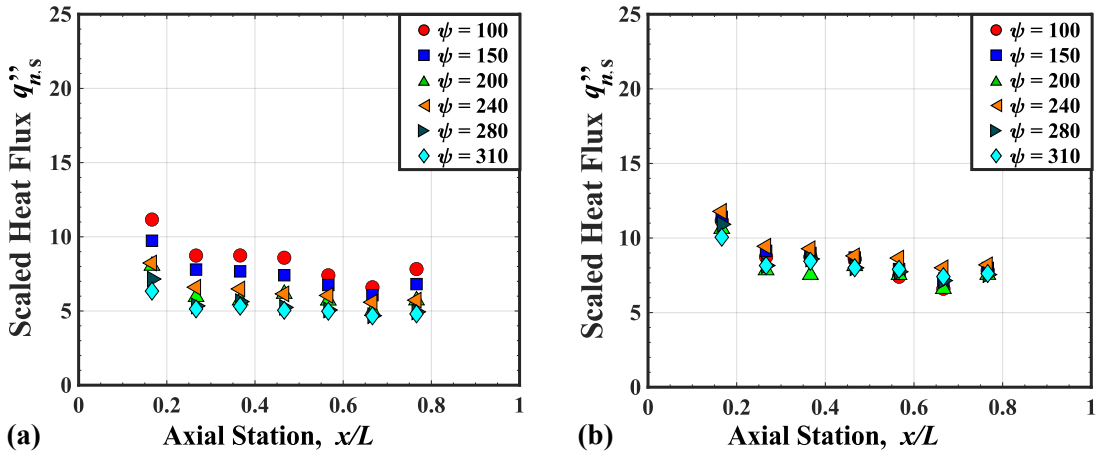


Figure 6.8: Heat scaled by total mass flow rate for (a) $\alpha = 0.8$ and (b) $\alpha = 0.38$.

6.2 Chamber Pressure

A total mass flux sensitivity study is performed for capillary tube attenuated pressure (CTAP). The CTAP pressure is recorded for the straight center body configuration hot fire tests (see Fig. 6.9 (a)) at the axial location of $x/L = 0.10$. The recorded pressures ranges from $p_c = 125 - 465$ kPa increasing linearly with the variation of total mass flux.

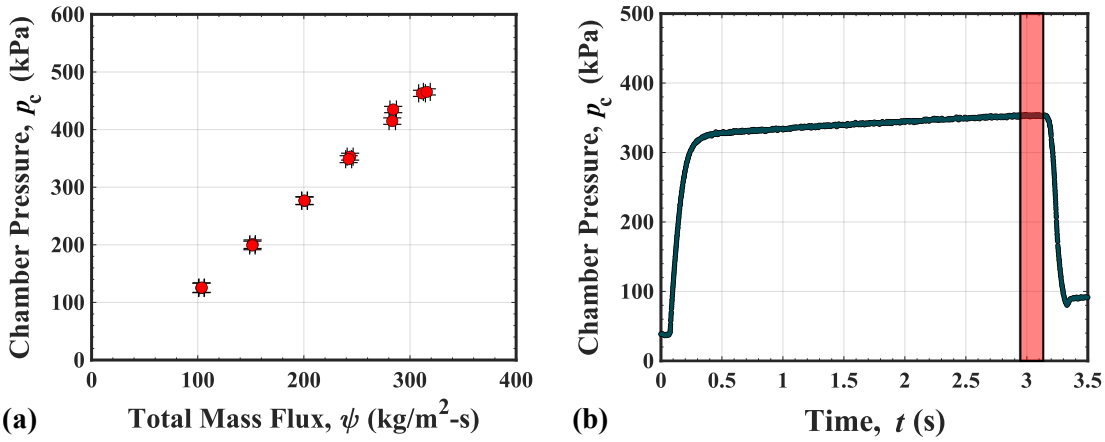


Figure 6.9: CTAP pressures for (a) all straight center body configuration tests at varying total mass flux, and (b) a $\boldsymbol{\psi}$ = 241 kg/m^2-s, $\boldsymbol{\phi}$ = 1.1 test.

6.3 Wave Dynamics

The wave dynamics for both the straight and constricted center body are analyzed using the methods outlined in section 5.4. In this RDRE, the wave dynamics are shown to be sensitive to the change in total mass flux for the straight center body configuration. Beginning at the low mass flux conditions between $\psi = 100 - 150$ kg/m^2-s, a two wave counter-rotating mode (+2/-2) is consistently

observed (Fig. 6.10 (a)). However, with total mass flux of $\psi = 200 - 240$ kg/m^2-s, a three wave counter-rotating mode (+3/-3) is observed (Fig. 6.10 (b)). For the straight center body at the higher mass flux cases ($\psi = 280 - 310$ kg/m^2-s), there is no observable trend.

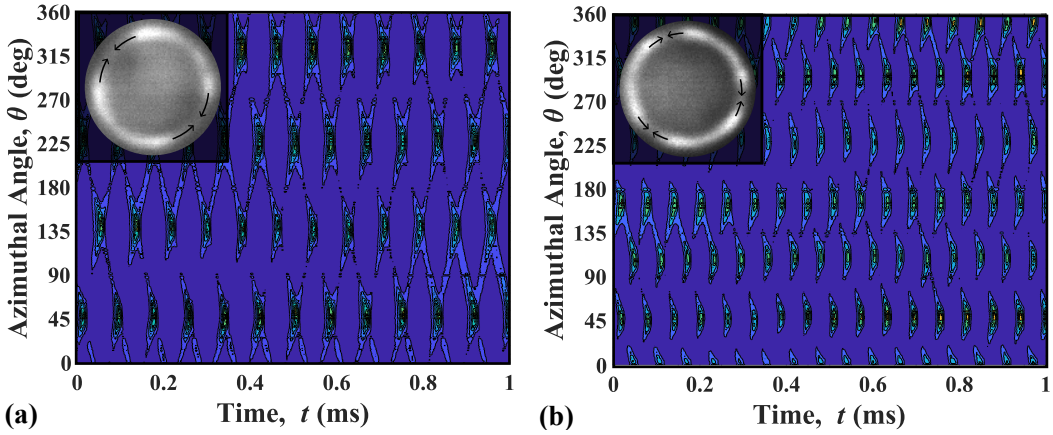


Figure 6.10: Detonation surface plots for (a) +2/-2 wave mode observed at $\psi = 100 - 150$ kg/m^2-s and (b) +3/-3 wave mode observed at $\psi = 200 - 240$ kg/m^2-s.

For the constricted center body configuration, the wave dynamics are less sensitive to total mass flux, however, the observed wave mode differs from that of the straight center body cases. Across all tested values of total mass flux ($\psi = 100 - 150$ kg/m^2-s)) a single wave rotating mode propagating counter-clockwise (-1) is observed (Fig. 6.12). All results from the image processing for each set condition can be found in Appendix A.

Additional testing is performed to evaluate the influence of operating mode on heat flux levels. In one $t_b = 4.5$ s test at $\phi = 1.1$, $\psi = 279$ kg/m^2-s, the operating mode dynamics are shown to influence the heat flux experienced by the combustor. For a total mass flux of $\psi = 279$ kg/m^2-s, the station 1 outlet tem-

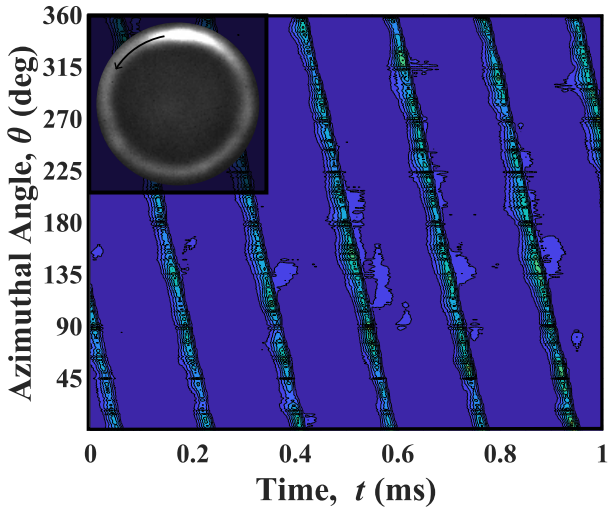


Figure 6.11: Detonation surface plots for the -1 wave mode observed at $\psi = 100 - 240$ kg/m^2-s with the constricted center body geometry.

perature appears to reach a steady-state temperature of $T_{\text{out}} = 320$ K, however, there is a sudden increase in the slope of the temperature measurement occurring at $t = 3.2$ s (see Fig. 6.12 (a)). From the beginning of the test, a single counter-clockwise rotating wave is seen until $t = 3.2$ s when the observed wave mode begins to transition from a (1) one wave rotating mode to a (2) counter-rotating wave mode with a single wave traveling in each direction (Fig. 6.12 (b)). During this transition period, from $t = 3.2 - 3.4$ s, a second wave traveling in the opposite begins to develop. At $t = 3.4$ s the wave dynamic fully transitions to a counter-rotating mode with a singular opposing wave pair. This closely corresponds with the sudden jump in coolant outlet temperature. This rise in temperature is observed across the first four stations ($x/L = 0.06 - 0.37$), most

likely corresponding to the axial location of the detonation zone. However, this is not observed for stations further downstream of $x/L = 0.37$.

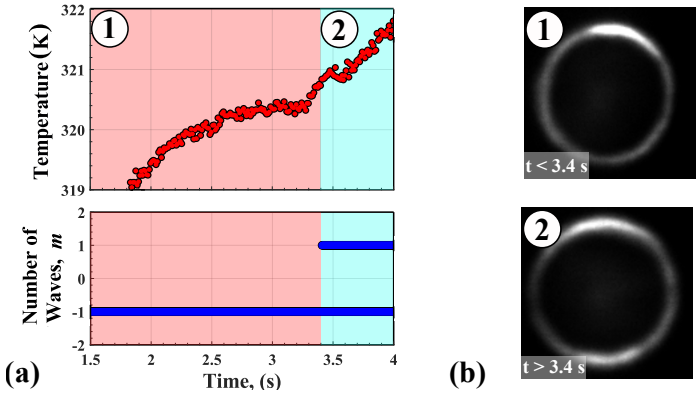


Figure 6.12: Constricted geometry test case at $\psi = 279$ kg/m^2-s, exhibiting (a) temperature rise associated with a change in engine operating mode and (b) accompanying high speed images of wave dynamics.

Chapter 7. Conclusions

Experimentally measured heat flux data is presented for a 76.8 mm additively manufactured water-based calorimetry RDRE outer body operating with gaseous methane (GCH_4) and oxygen (GO_2). The hardware is tested with both a straight and constricted center body configuration at an equivalence ratio of $\phi = 1.1$ and total mass flux ranging from $\psi = 103 - 310$ kg/m^2-s. Average heat flux is determined to be between $6.6 - 16.3$ MW/m^2 for the straight center body tests and $11.4 - 20.5$ MW/m^2 for the constricted center body tests. Maximum heat flux occurs at $x/L = 0.17$ for the straight chamber tests and $x/L = 0.77$ for the constricted geometry cases; these two maximum heat flux regions correspond to the likely detonation zone and throat location for the straight and constricted geometries, respectively. These average heat flux measurements serve to increase the understanding of the thermal loads found in rotating detonation engines. The average heat flux measurements captured in this study help enhance the understanding for the heat flux loadings in detonation-based engines to ultimately help develop thermal management strategies enabling long duration operation.

References

[1] Berthelot, V. P., M., "Sur la force des matieres explosives," *Annales de Chimie et de Physique*, 1882.

[2] Mallard, and Chatelier, L., "Recherches sur la Combustion des Melanges Gazeux Explosifs," *Journal de Physique Théorique et Appliquée*, Vol. 4, No. 1, 1885, p. 59–84. https://doi.org/10.1051/jphystap:01885004005901, URL http://dx.doi.org/10.1051/jphystap:01885004005901.

[3] Chapman, D. L., "On the Rate of Explosion in Gases," *The London, Edinburgh, and Dublin Philosophical Magazine and Journal of Science*, Vol. 47, No. 284, 1899, p. 90–104. https://doi.org/10.1080/14786449908621243, URL http://dx.doi.org/10.1080/14786449908621243.

[4] Jouguet, E., "On the Propagation of Chemical Reactions in Gases," *Journal de Mathematiques Pures et Appliquees*, Vol. 6, 1905, pp. 347–425.

[5] Berets, D. J., Greene, E. F., and Kistiakowsky, G. B., "Gaseous Detonations. I. Stationary Waves in Hydrogen—Oxygen Mixtures," *Journal of the American Chemical Society*, Vol. 72, No. 3, 1950, p. 1080–1086. https://doi.org/10.1021/ja01159a008, URL http://dx.doi.org/10.1021/ja01159a008.

[6] Wolański, P., "Detonative propulsion," *Proceedings of the Combustion Institute*, Vol. 34, No. 1, 2013, p. 125–158. https://doi.org/10.1016/j.proci.2012.10.005, URL http://dx.doi.org/10.1016/j.proci.2012.10.005.

[7] Kailasanath, K., "Research on Pulse Detonation Combustion Systems: A Status Report," *47th AIAA Aerospace Sciences Meeting including The New Horizons Forum and Aerospace Exposition*, American Institute of Aeronautics and Astronautics, 2009. https://doi.org/10.2514/6.2009-631, URL http://dx.doi.org/10.2514/6.2009-631.

[8] Nicholls, J., Dabora, E., and Gealer, R., "Studies in Connection With Stabilized Gaseous Detonation Waves," *Symposium (International) on Combustion*, Vol. 7, No. 1, 1958, p. 766–772. https://doi.org/10.1016/s0082-0784(58)80118-6, URL http://dx.doi.org/10.1016/s0082-0784(58)80118-6.

[9] Rosato, D. A., Thornton, M., Sosa, J., Bachman, C., Goodwin, G. B., and Ahmed, K. A., "Stabilized Detonation for Hypersonic Propulsion," *Proceedings of the National Academy of Sciences*, Vol. 118, No. 20, 2021. https://doi.org/10.1073/pnas.2102244118, URL http://dx.doi.org/10.1073/pnas.2102244118.

[10] Dunlap, R., Brehm, R. L., and Nicholls, J. A., "A Preliminary Study of the Application of Steady-State Detonative Combustion to a Reaction Engine," *Journal of Jet Propulsion*, Vol. 28, No. 7, 1958, p. 451–456. https://doi.org/10.2514/8.7347, URL http://dx.doi.org/10.2514/8.7347.

[11] Nicholls, J. A., Wilkinson, H. R., and Morrison, R. B., "Intermittent Detonation as a Thrust-Producing Mechanism," *Journal of Jet Propulsion*, Vol. 27, No. 5, 1957, p. 534–541. https://doi.org/10.2514/8.12851, URL http://dx.doi.org/10.2514/8.12851.

[12] Roy, G., Frolov, S., Borisov, A., and Netzer, D., "Pulse Detonation Propulsion: Challenges, Current Status, and Future Perspective," *Progress in Energy and Com-*

bustion Science, Vol. 30, No. 6, 2004, p. 545–672. https://doi.org/10.1016/j.pecs.2004.05.001, URL http://dx.doi.org/10.1016/j.pecs.2004.05.001.

[13] Buyakofu, V., Matsuoka, K., Matsuyama, K., Goto, K., Kawasaki, A., Watanabe, H., Itouyama, N., Ishihara, K., Noda, T., Kasahara, J., Matsuo, A., Funaki, I., Nakata, D., Uchiumi, M., Habu, H., Takeuchi, S., Arakawa, S., Masuda, J., Maehara, K., Nakao, T., and Yamada, K., "Flight Demonstration of Detonation Engine System Using Sounding Rocket S-520-31: Performance of Pulse Detonation Engine," *AIAA SCITECH 2022 Forum*, American Institute of Aeronautics and Astronautics, 2022. https://doi.org/10.2514/6.2022-0233, URL http://dx.doi.org/10.2514/6.2022-0233.

[14] Bussing, T., and Pappas, G., "An Introduction to Pulse Detonation Engines," *32nd Aerospace Sciences Meeting and Exhibit*, American Institute of Aeronautics and Astronautics, 1994. https://doi.org/10.2514/6.1994-263, URL http://dx.doi.org/10.2514/6.1994-263.

[15] Voitsekhovskii, B. V., "Stationary Spin Detonation," *Soviet Journal of Applied Mechanics and Technical Physics*, Vol. 3, 1960, pp. 156–164.

[16] Nicholls, J. A., Cullen, R. E., and Ragland, K. W., "Feasibility Studies of a Rotating Detonation Wave Rocket Motor." *Journal of Spacecraft and Rockets*, Vol. 3, No. 6, 1966, p. 893–898. https://doi.org/10.2514/3.28557, URL http://dx.doi.org/10.2514/3.28557.

[17] Oefelein, J. C., and Yang, V., "Comprehensive Review of Liquid-Propellant Combustion Instabilities in F-1 Engines," *Journal of Propulsion and Power*, Vol. 9,

No. 5, 1993, p. 657–677. https://doi.org/10.2514/3.23674, URL http://dx.doi.org/10.2514/3.23674.

[18] Lu, F. K., and Braun, E. M., "Rotating Detonation Wave Propulsion: Experimental Challenges, Modeling, and Engine Concepts," *Journal of Propulsion and Power*, Vol. 30, No. 5, 2014, p. 1125–1142. https://doi.org/10.2514/1.b34802, URL http://dx.doi.org/10.2514/1.b34802.

[19] Rankin, B. A., Fotia, M. L., Naples, A. G., Stevens, C. A., Hoke, J. L., Kaemming, T. A., Theuerkauf, S. W., and Schauer, F. R., "Overview of Performance, Application, and Analysis of Rotating Detonation Engine Technologies," *Journal of Propulsion and Power*, Vol. 33, No. 1, 2017, p. 131–143. https://doi.org/10.2514/1.b36303, URL http://dx.doi.org/10.2514/1.b36303.

[20] Fotia, M., Hoke, J., and Schauer, F., "Study of the Ignition Process in a Laboratory Scale Rotating Detonation Engine," *Experimental Thermal and Fluid Science*, Vol. 94, 2018, p. 34–354. https://doi.org/10.1016/j.expthermflusci.2017.11.002, URL http://dx.doi.org/10.1016/j.expthermflusci.2017.11.002.

[21] Boening, J. A., Wheeler, E. A., Heath, J. D., Koch, J. V., Mattick, A. T., Breidenthal, R. E., Knowlen, C., and Kurosaka, M., "Rotating Detonation Engine Using a Wave Generator and Controlled Mixing," *Journal of Propulsion and Power*, Vol. 34, No. 6, 2018, p. 1364–1375. https://doi.org/10.2514/1.b36603, URL http://dx.doi.org/10.2514/1.b36603.

[22] Sosa, J., Burke, R., Ahmed, K. A., Micka, D. J., Bennewitz, J. W., Danczyk, S. A., Paulson, E. J., and Hargus, W. A., "Experimental Evidence of H2/O2 Propellants Powered Rotating Detonation Waves," *Combustion and Flame*, Vol. 214, 2020, p.

136–138. https://doi.org/10.1016/j.combustflame.2019.12.031, URL http://dx.doi.org/10.1016/j.combustflame.2019.12.031.

[23] Bennewitz, J. W., Bigler, B. R., Ross, M. C., Danczyk, S. A., Hargus, W. A., and Smith, R. D., "Performance of a Rotating Detonation Rocket Engine with Various Convergent Nozzles and Chamber Lengths," *Energies*, Vol. 14, No. 8, 2021, p. 2037. https://doi.org/10.3390/en14082037, URL http://dx.doi.org/10.3390/en14082037.

[24] Kawasaki, A., Inakawa, T., Kasahara, J., Goto, K., Matsuoka, K., Matsuo, A., and Funaki, I., "Critical Condition of Inner Cylinder Radius for Sustaining Rotating Detonation Waves in Rotating Detonation Engine Thruster," *Proceedings of the Combustion Institute*, Vol. 37, No. 3, 2019, p. 3461–3469. https://doi.org/10.1016/j.proci.2018.07.070, URL http://dx.doi.org/10.1016/j.proci.2018.07.070.

[25] Unruh, E., "Development and Testing of a Rotating Detonation Rocket Engine with a Racetrack Combustor and Shear-Coaxial Injectors," Master's thesis, The University of Alabama in Huntsville, 2021.

[26] Bennewitz, J. W., Bigler, B., Danczyk, S., Hargus, W. A., and Smith, R. D., "Performance of a Rotating Detonation Rocket Engine with Various Convergent Nozzles," *AIAA Propulsion and Energy 2019 Forum*, American Institute of Aeronautics and Astronautics, 2019. https://doi.org/10.2514/6.2019-4299, URL http://dx.doi.org/10.2514/6.2019-4299.

[27] Fotia, M. L., Schauer, F., Kaemming, T., and Hoke, J., "Experimental Study of the Performance of a Rotating Detonation Engine with Nozzle," *Journal of Propulsion and Power*, Vol. 32, No. 3, 2016, p. 674–681. https://doi.org/10.2514/1.b35913, URL http://dx.doi.org/10.2514/1.b35913.

[28] Goto, K., Nishimura, J., Kawasaki, A., Matsuoka, K., Kasahara, J., Matsuo, A., Funaki, I., Nakata, D., Uchiumi, M., and Higashino, K., "Propulsive Performance and Heating Environment of Rotating Detonation Engine with Various Nozzles," *Journal of Propulsion and Power*, Vol. 35, No. 1, 2019, p. 213–223. https://doi.org/10.2514/1.b37196, URL http://dx.doi.org/10.2514/1.b37196.

[29] Smith, R. D., and Stanley, S. B., "Experimental Investigation of Rotating Detonation Rocket Engines for Space Propulsion," *Journal of Propulsion and Power*, Vol. 37, No. 3, 2021, p. 463–473. https://doi.org/10.2514/1.b37959, URL http://dx.doi.org/10.2514/1.b37959.

[30] Bigler, B. R., Bennewitz, J. W., Danczyk, S. A., and Hargus, W. A., "Rotating Detonation Rocket Engine Operability Under Varied Pressure Drop Injection," *Journal of Spacecraft and Rockets*, Vol. 58, No. 2, 2021, p. 316–325. https://doi.org/10.2514/1.a34763, URL http://dx.doi.org/10.2514/1.a34763.

[31] Fotia, M. L., Hoke, J., and Schauer, F., *Performance of Rotating Detonation Engines for Air Breathing Applications*, Springer International Publishing, 2017, p. 1–21. https://doi.org/10.1007/978-3-319-68906-7_1, URL http://dx.doi.org/10.1007/978-3-319-68906-7_1.

[32] Goto, K., Kato, Y., Ishihara, K., Matsuoka, K., Kasahara, J., Matsuo, A., Funaki, I., Nakata, D., Higashino, K., and Tanatsugu, N., "Thrust Validation of Rotating Detonation Engine System by Moving Rocket Sled Test," *Journal of Propulsion and Power*, Vol. 37, No. 3, 2021, p. 419–425. https://doi.org/10.2514/1.b38037, URL http://dx.doi.org/10.2514/1.b38037.

[33] Bedick, C., Ferguson, D. H., Billups, D., O'Meara, B., Strakey, P., and Nix, A. C., "Characterization of Rotating Detonation Engine Injector Response using Acetone PLIF in a Lab-Scale Experimental Testing Platform," *2018 Joint Propulsion Conference*, American Institute of Aeronautics and Astronautics, 2018. https://doi.org/10.2514/6.2018-4481, URL http://dx.doi.org/10.2514/6.2018-4481.

[34] Bigler, B. R., Bennewitz, J. W., Schumaker, S. A., Danczyk, S. A., and Hargus, W. A., "Injector Alignment Study for Variable Mixing in Rotating Detonation Rocket Engines," *AIAA Scitech 2019 Forum*, American Institute of Aeronautics and Astronautics, 2019. https://doi.org/10.2514/6.2019-2019, URL http://dx.doi.org/10.2514/6.2019-2019.

[35] Bennewitz, J. W., Burr, J. R., Bigler, B. R., Burke, R. F., Lemcherfi, A., Mundt, T., Rezzag, T., Plaehn, E. W., Sosa, J., Walters, I. V., Schumaker, S. A., Ahmed, K. A., Slabaugh, C. D., Knowlen, C., and Jr., W. A. H., "Experimental Validation of Rotating Detonation for Rocket Propulsion," *Scientific Reports*, Vol. 13, No. 1, 2023, p. 14204. https://doi.org/10.1038/s41598-023-40156-y, URL https://doi.org/10.1038/s41598-023-40156-y.

[36] Knowlen, C., Mundt, T. J., Roberts, Q., Hamza, A., Menn, D., and Kurosaka, M., "Operating Characteristics of a 10-mm Rotating Detonation Rocket Engine," *AIAA SCITECH 2024 Forum*, American Institute of Aeronautics and Astronautics, 2024. https://doi.org/10.2514/6.2024-2610, URL http://dx.doi.org/10.2514/6.2024-2610.

[37] Knowlen, C., Mundt, T., and Kurosaka, M., "Experimental results for 25-mm and 51-mm rotating detonation rocket engine combustors," *Shock Waves*, Vol. 33, No. 3,

2023, p. 237–252. https://doi.org/10.1007/s00193-023-01120-x, URL http://dx.doi.org/10.1007/s00193-023-01120-x.

[38] Mundt, T., Knowlen, C., and Kurosaka, M., "Scale Effects on Rotating Detonation Rocket Engine Operation," *Applications in Energy and Combustion Science*, Vol. 19, 2024, p. 100282. https://doi.org/10.1016/j.jaecs.2024.100282, URL http://dx.doi.org/10.1016/j.jaecs.2024.100282.

[39] Fiorino, N. T., Snow, N. J., Schauer, F. R., Polanka, M. D., Alexander Schumaker, S., and Sell, B. C., "Improving Detonability in a Small-Scale Rotating Detonation Engine Using Partial Premixing," *Journal of Propulsion and Power*, 2022, p. 1–10. https://doi.org/10.2514/1.b38668, URL http://dx.doi.org/10.2514/1.b38668.

[40] Yokoo, R., Goto, K., Kawasaki, A., Matsuoka, K., Kasahara, J., Matsuo, A., and Funaki, I., "Combustion Pressure Distributions and Thrust Performances in Small Cylindrical Rotating Detonation Engines," *AIAA Scitech 2020 Forum*, American Institute of Aeronautics and Astronautics, 2020. https://doi.org/10.2514/6.2020-0202, URL http://dx.doi.org/10.2514/6.2020-0202.

[41] Durkee, K. J., Dave, R. T., Maybee, M. A., Cobb, G. R., Burr, J. R., and Bennewitz, J. W., "Performance Comparison of Variable Center Body Configurations for a 25 mm Rotating Detonation Rocket Engine," , 2025.

[42] Dave, R. T., Durkee, K. J., Cobb, G. R., Maybee, M. A., Burr, J. R., and Bennewitz, J. W., "Experimental Testing of a 25 mm Rotating Detonation Rocket Engine With Methane and Hydrogen," , 2025.

[43] Durkee, K. J., Dave, R. T., Maybee, M. A., Cobb, G. R., Burr, J. R., and Bennewitz, J. W., "Performance Measurements of a 25 mm Rotating Detonation Rocket Engine," 2024.

[44] Teasley, T. W., Petty, D. M., Hemming, M. R., Scarborough, D., and Heister, S. D., "Heat Transfer Measurements of NASA Liquid Kerosene/Oxygen Rotating Detonation Rocket Engine," , 2025.

[45] et al., T. S., "Flight Demonstration of Detonation Engine System Using Sounding Rocket S-520-34: Performance of Rotating Detonation Engine Using Liquid Propellants," , 2025.

[46] Kawalec, M., Perkowski, W., Lukasik, B., Bilar, A., and Wolański, P., "Applications of The Continuously Rotating Detonation to Combustion Engines at the Lukasiewicz - Institute of Aviation," *Combustion Engines*, 2022. https://doi.org/10.19206/ce-145409, URL http://dx.doi.org/10.19206/ce-145409.

[47] Knowlen, C., Mundt, T., and Kurosaka, M., "Experimental Results for 25-mm and 51-mm Rotating Detonation Rocket Engine Combustors," *Shock Waves*, Vol. 33, No. 3, 2023, p. 237–252. https://doi.org/10.1007/s00193-023-01120-x, URL http://dx.doi.org/10.1007/s00193-023-01120-x.

[48] Micka, D. J., Daines, G., Sosa, J., Burke, R. F., Ahmed, K. A., Paulson, E., Bennewitz, J. W., Danczyk, S., and Hargus, W. A., "Heat Transfer Measurements in an Elevated Pressure RDRE Combustor," *AIAA Propulsion and Energy 2021 Forum*, American Institute of Aeronautics and Astronautics, 2021. https://doi.org/10.2514/6.2021-3685, URL http://dx.doi.org/10.2514/6.2021-3685.

[49] Bartz, D. R., "Survey of Relationships between Theory and Experiment for Convective Heat Transfer in Rocket Combustion Gases," *Advances in Rocket Propulsion*, 1968.

[50] Theuerkauf, S. W., Schauer, F., Anthony, R., and Hoke, J., "Experimental Characterization of High-Frequency Heat Flux in a Rotating Detonation Engine," *53rd AIAA Aerospace Sciences Meeting*, American Institute of Aeronautics and Astronautics, 2015. https://doi.org/10.2514/6.2015-1603, URL http://dx.doi.org/10.2514/6.2015-1603.

[51] Theuerkauf, S., King, P., Schauer, F., and Hoke, J., "Thermal Management for a Modular Rotating Detonation Engine," *51st AIAA Aerospace Sciences Meeting including the New Horizons Forum and Aerospace Exposition*, American Institute of Aeronautics and Astronautics, 2013. https://doi.org/10.2514/6.2013-1176, URL http://dx.doi.org/10.2514/6.2013-1176.

[52] Hernandez-McCloskey, J., Pineda, D. I., Bennewitz, J. W., Bigler, B. R., Burr, J. R., Danczyk, S. A., Paulson, E. J., and Hargus, W. A., "Design and Analysis of an Additively Manufactured Rotating Detonation Rocket Engine Chamber for Calorimetry and Thermal Management Assessment," *AIAA SCITECH 2023 Forum*, American Institute of Aeronautics and Astronautics, 2023. https://doi.org/10.2514/6.2023-0355, URL http://dx.doi.org/10.2514/6.2023-0355.

[53] Smallwood, J. S., and Heister, S. D., "Thermal and Structural Characterization of a Rotating Detonation Rocket Engine," *AIAA SCITECH 2024 Forum*, American Institute of Aeronautics and Astronautics, 2024. https://doi.org/10.2514/6.2024-0816, URL http://dx.doi.org/10.2514/6.2024-0816.

[54] Aliakbari, R., Michalski, Q., Mason-Smith, N., Pudsey, A., Wenzel, M., and Paull, N., "Heat Flux Measurements of a Methane-Oxygen Rotating Detonation Rocket Engine," *12th International Workshop on Detonation Propulsion*, 2022.

[55] HernandezMcCloskey, J., Teasley, T. W., Petty, D. M., Reutlinger, S. A., and Pineda, D. I., "Calorimeter Heat Flux Trends in NASA's Subscale Rotating Detonation Rocket Engine," , 2025.

[56] Fickett, D. W. C., W., *Detonation: Theory and Experiment*, Dover Publications inc., 2001.

[57] Turns, S., *An Introduction to Combustion: Concepts and Applications*, McGraw-Hill Book Co., 2000.

[58] Zeldovich, Y. B., "On the theory of the propagation of detonation in gaseous systems," 1940. URL https://api.semanticscholar.org/CorpusID:91326618.

[59] P., H., and Taub, A. H., "John von Neumann, Collected Works, Volume VI," *Mathematics of Computation*, Vol. 19, No. 90, 1965, p. 346. https://doi.org/10.2307/2003380, URL http://dx.doi.org/10.2307/2003380.

[60] Doring, W., "On Detonation Processes in Gases," *Annalen der physik*, Vol. 43, 1943, pp. 421–436.

[61] Lee, J. H. S., *The Detonation Phenomenon*, Cambridge University Press, 2008.

[62] Wintenberger, E., and Shepherd, J. E., "Thermodynamic Cycle Analysis for Propagating Detonations," *Journal of Propulsion and Power*, Vol. 22, No. 3, 2006, p. 694–698. https://doi.org/10.2514/1.12775, URL http://dx.doi.org/10.2514/1.12775.

[63] Wintenberger, E., "Application of Steady and Unsteady Detonation Waves to Propulsion," Ph.D. thesis, California Institute of Technology, 2004. https://doi.org/doi:10.7907/2NXT-SE76, URL https://resolver.caltech.edu/CaltechETD:etd-04222004-121013.

[64] Namkoung, H.-J., Han, P.-G., Lee, K.-H., Kim, Y.-S., Kim, C., and Yoon, Y.-B., "Study on Heat Transfer Characteristics of Small Liquid Rocket Engine with Calorimeter," *42nd AIAA/ASME/SAE/ASEE Joint Propulsion Conference & Exhibit*, American Institute of Aeronautics and Astronautics, 2006. https://doi.org/10.2514/6.2006-5195, URL http://dx.doi.org/10.2514/6.2006-5195.

[65] Masters, P. A., Armstrong, E. S., and Price, H. G., "High Pressure Calorimeter Chamber Tests for LIquid Oxygen/Kerosene (LOX/RP-1) Rocket Combustion," Technical Paper NASA/TP-1988-2862, NASA, Lewis Research Center, Cleveland, Ohio, USA, 1988.

[66] Rose, R. K., "Experimental Determination of the Heat Flux Distribution In a Rocket Nozzle," Final Report 58-1, Purdue University Rocket Laboratory, Lafayette, Indiana, USA, January 1958.

[67] Huzel, D., and Huang, D., *Modern Engineering for Design of Liquid Propellant Rocket Engines*, American Institute of Aeronautics and Astronautics, 1992.

[68] Vafadar, A., Guzzomi, F., Rassau, A., and Hayward, K., "Advances in Metal Additive Manufacturing: A Review of Common Processes, Industrial Applications, and Current Challenges," *Applied Sciences*, Vol. 11, No. 3, 2021, p. 1213. https://doi.org/10.3390/app11031213, URL http://dx.doi.org/10.3390/app11031213.

[69] Gradl, P., *Metal Additive Manufacturing for Propulsion Applications*, American Institute of Aeronautics and Astronautics, Inc., 2022. https://doi.org/10.2514/4.106279, URL http://dx.doi.org/10.2514/4.106279.

[70] Gradl, P. R., Protz, C. S., Cooper, K., Ellis, D., Evans, L. J., and Garcia, C., "GRCop-42 Development and Hot-fire Testing Using Additive Manufacturing Powder Bed Fusion for Channel-cooled Combustion Chambers," *AIAA Propulsion and Energy 2019 Forum*, American Institute of Aeronautics and Astronautics, 2019. https://doi.org/10.2514/6.2019-4228, URL http://dx.doi.org/10.2514/6.2019-4228.

[71] Cobb, G., Durkee, K., Burr, J., and Bennewitz, J., "Thermodynamic Power Cycle Analysis in Actively Cooled Rotating Detonation Rocket Engines," *AIAA Scitech 2025 Forum*, American Institute of Aeronautics and Astronautics, 2025.

[72] Burr, J. R., and Paulson, E., "Thermodynamic Performance Results for Rotating Detonation Rocket Engine with Distributed Heat Addition using Cantera," *AIAA Propulsion and Energy 2021 Forum*, American Institute of Aeronautics and Astronautics, 2021. https://doi.org/10.2514/6.2021-3682, URL http://dx.doi.org/10.2514/6.2021-3682.

[73] Teasley, T. W., Protz, C. S., Larkey, A. P., Williams, B. B., and Gradl, P. R., "A Review Towards the Design Optimization of High Performance Additively Manufactured Rotating Detonation Rocket Engine Injectors," *AIAA Propulsion and Energy 2021 Forum*, American Institute of Aeronautics and Astronautics, 2021. https://doi.org/10.2514/6.2021-3655, URL http://dx.doi.org/10.2514/6.2021-3655.

[74] Kolb, T., Mahr, A., Huber, F., Tremel, J., and Schmidt, M., "Qualification of Channels Produced by Laser Powder Bed Fusion: Analysis of Cleaning Methods, Flow Rate and Melt Pool Monitoring Data," *Additive Manufacturing*, Vol. 25, 2019, p. 430–436. https://doi.org/10.1016/j.addma.2018.11.026, URL http://dx.doi.org/10.1016/j.addma.2018.11.026.

[75] Sutton, G., and Biblarz, O., *Rocket Propulsion Elements*, 2nd ed., John Wiley & Sons, Inc., 1956.

[76] Rayle Jr., R. E., "An Investigation of the Influence of Orifice Geometry on Static Pressure Measurements," 1949.

[77] Majumdar, A. K., Leclair, A., Moore, R., and Schallhorn, P. A., "Generalized Fluid System Simulation Program (GFSSP) - Version 6," *51st AIAA/SAE/ASEE Joint Propulsion Conference*, American Institute of Aeronautics and Astronautics, 2015. https://doi.org/10.2514/6.2015-3850, URL http://dx.doi.org/10.2514/6.2015-3850.

[78] Bell, I. H., Wronski, J., Quoilin, S., and Lemort, V., "Pure and Pseudo-pure Fluid Thermophysical Property Evaluation and the Open-Source Thermophysical Property Library CoolProp," *Industrial & Engineering Chemistry Research*, Vol. 53, No. 6, 2014, pp. 2498–2508. https://doi.org/10.1021/ie4033999, URL http://pubs.acs.org/doi/abs/10.1021/ie4033999.

[79] Jones, D. A., Braswell, V., Lineberry, D. M., and Frederick, R. A., "UAH Propulsion Research Center Rocket Test Upgrade," *2018 Joint Propulsion Conference*, American Institute of Aeronautics and Astronautics, 2018. https://doi.org/10.2514/6.2018-4408, URL http://dx.doi.org/10.2514/6.2018-4408.

[80] Rathsack, T., Bigler, B. R., Bennewitz, J. W., Danczyk, S. A., and Hargus, W. A., "Laboratory Flow Measurement in Rotating Detonation Rocket Engines," *AIAA Scitech 2020 Forum*, American Institute of Aeronautics and Astronautics, Orlando, FL, 2020. https://doi.org/10.2514/6.2020-0194, URL https://arc.aiaa.org/doi/10.2514/6.2020-0194.

[81] Johnson, R. C., "Real-Gas Effects In Critical Flow Through Nozzles and Tabulated Thermodynamic Properties," Tech. Rep. TN D-2565, NASA, 1965. URL https://ntrs.nasa.gov/api/citations/19690006766/downloads/19690006766.pdf.

[82] Stewart, D., Watson, J., and Vaidya, A., "Improved Critical Flow Factors and Representative Equations for Four Calibration Gases," *Flow Measurement and Instrumentation*, Vol. 10, No. 1, 1999, pp. 27–34. https://doi.org/https://doi.org/10.1016/S0955-5986(98)00036-3, URL https://www.sciencedirect.com/science/article/pii/S0955598698000363.

[83] Bennewitz, J. W., Bigler, B. R., Schumaker, S. A., and Hargus, J., W. A., "Automated Image Processing Method to Quantify Rotating Detonation Wave Behavior," *Review of Scientific Instruments*, Vol. 90, No. 6, 2019, p. 065106. https://doi.org/10.1063/1.5067256, URL https://doi.org/10.1063/1.5067256.

[84] BIPM, IEC, IFCC, ILAC, ISO, IUPAC, IUPAP, and OIML, "Evaluation of measurement data — Guide to the expression of uncertainty in measurement," Joint Committee for Guides in Metrology, JCGM 100:2008, 2008. URL https://www.bipm.org/documents/20126/2071204/JCGM_100_2008_E.pdf/cb0ef43f-baa5-11cf-3f85-4dcd86f77bd6.

[85] Burns, G. W., Scroger, M. G., Strouse, G. F., Croarkin, M. C., and Guthrie, W. F., *Temperature-electromotive force reference functions and tables for the letter-designated thermocouple types based on the ITS-90*, NIST Monograph 175, National Institute of Standards and Technology, Gaithersburg, MD, USA, 1993. https://doi.org/10.6028/NIST.MONO.175.

Appendix A: Test Data

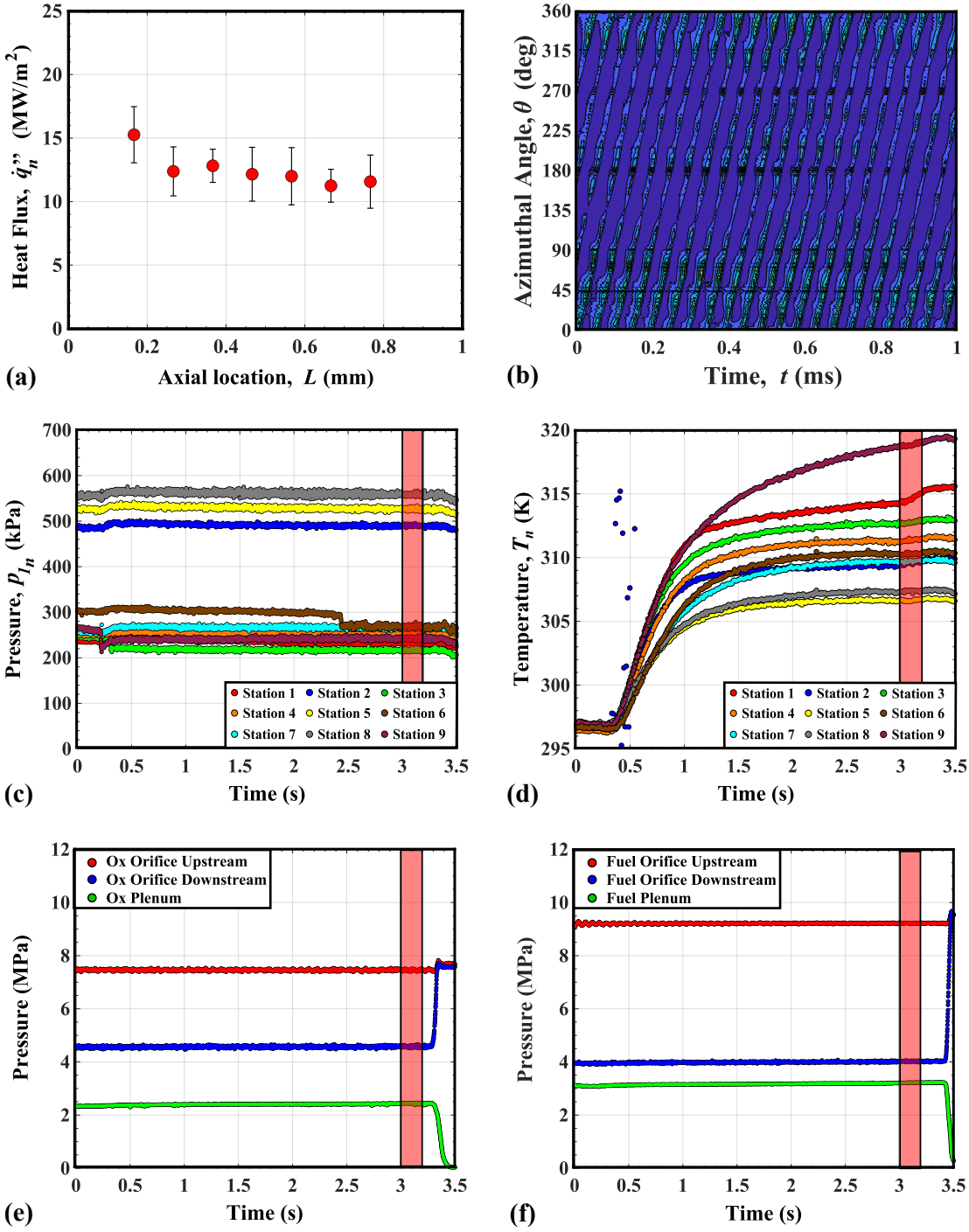


Figure A.1: Test 20241025-012 (a) axial heat flux, (b) thrust, (c) outlet pressure, (d) outlet temperature, (e) oxygen pressures, and (f) fuel pressures.

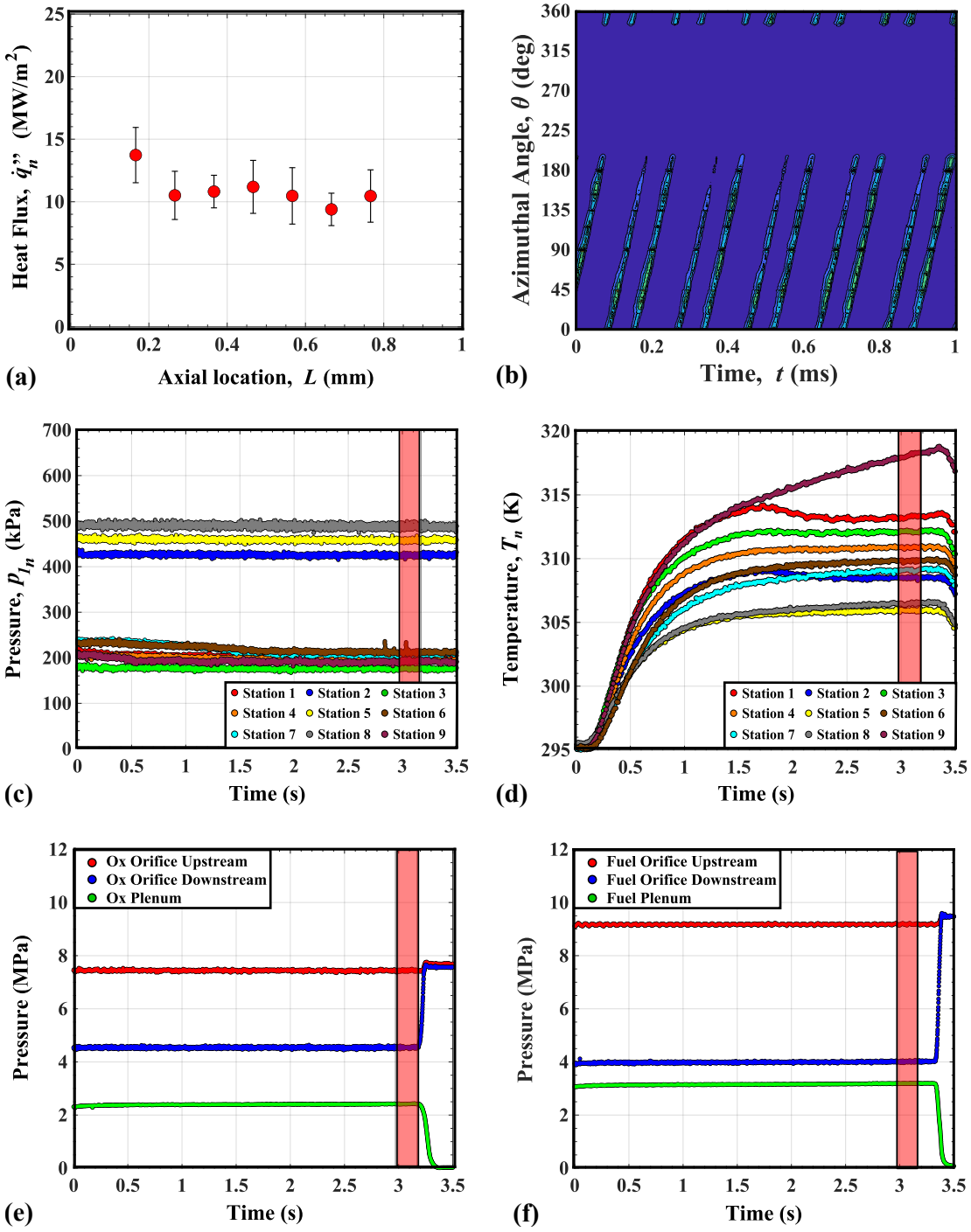


Figure A.2: Test 20241028-006 (a) axial heat flux, (b) thrust, (c) outlet pressure, (d) outlet temperature, (e) oxygen pressures, and (f) fuel pressures.

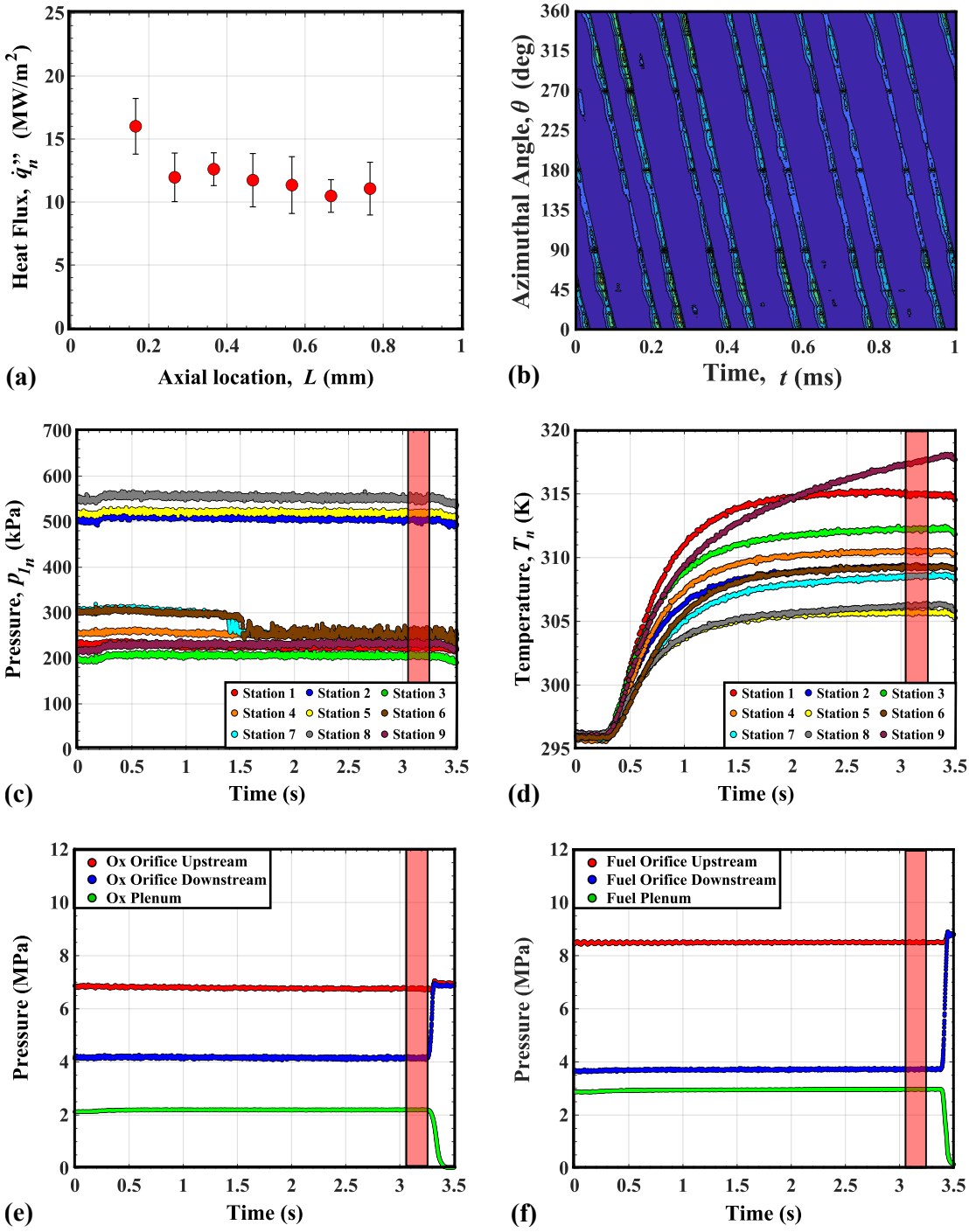


Figure A.3: Test 20241028-009 (a) axial heat flux, (b) thrust, (c) outlet pressure, (d) outlet temperature, (e) oxygen pressures, and (f) fuel pressures.

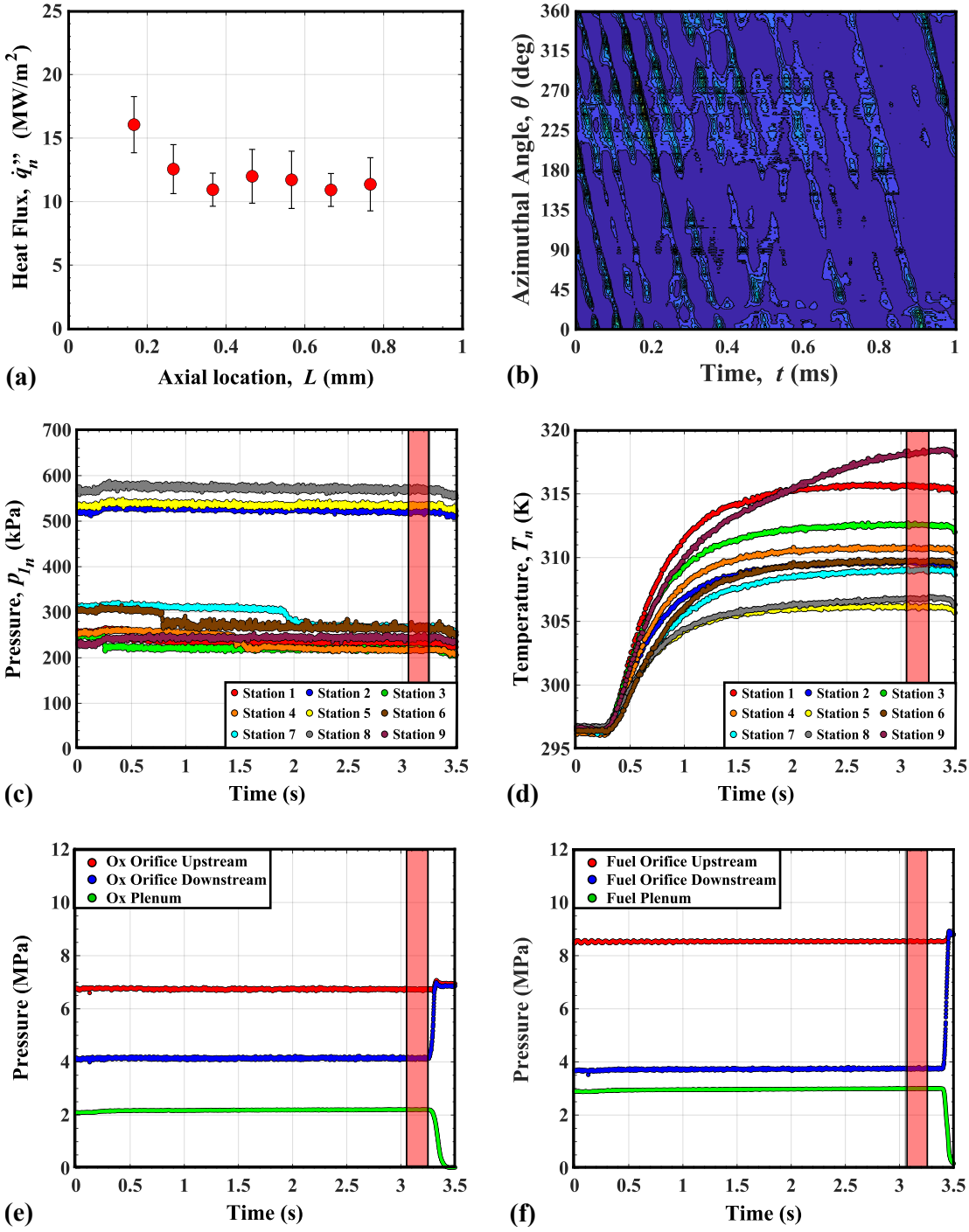


Figure A.4: Test 20241028-010 (a) axial heat flux, (b) thrust, (c) outlet pressure, (d) outlet temperature, (e) oxygen pressures, and (f) fuel pressures.

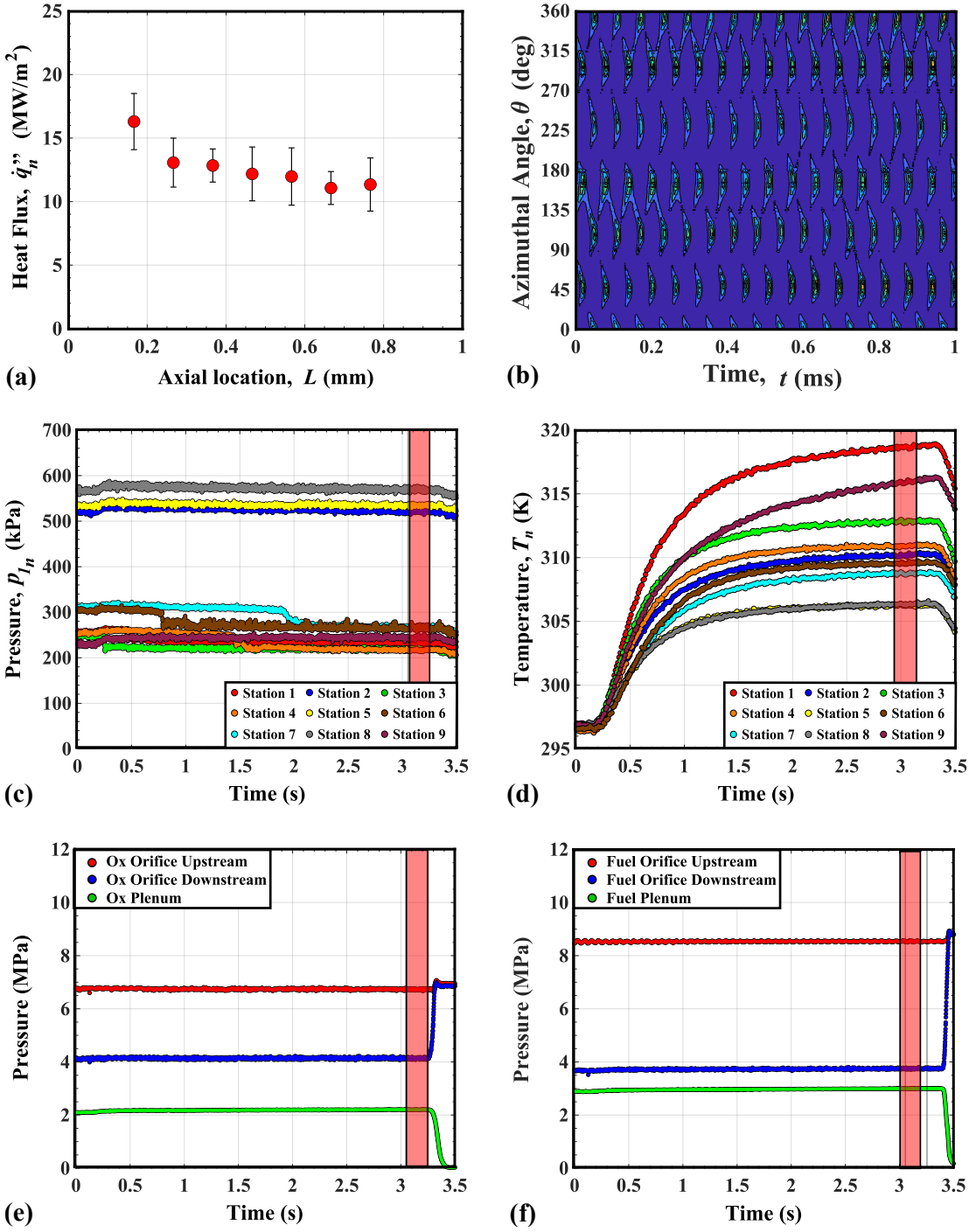


Figure A.5: Test 20241028-011 (a) axial heat flux, (b) thrust, (c) outlet pressure, (d) outlet temperature, (e) oxygen pressures, and (f) fuel pressures.

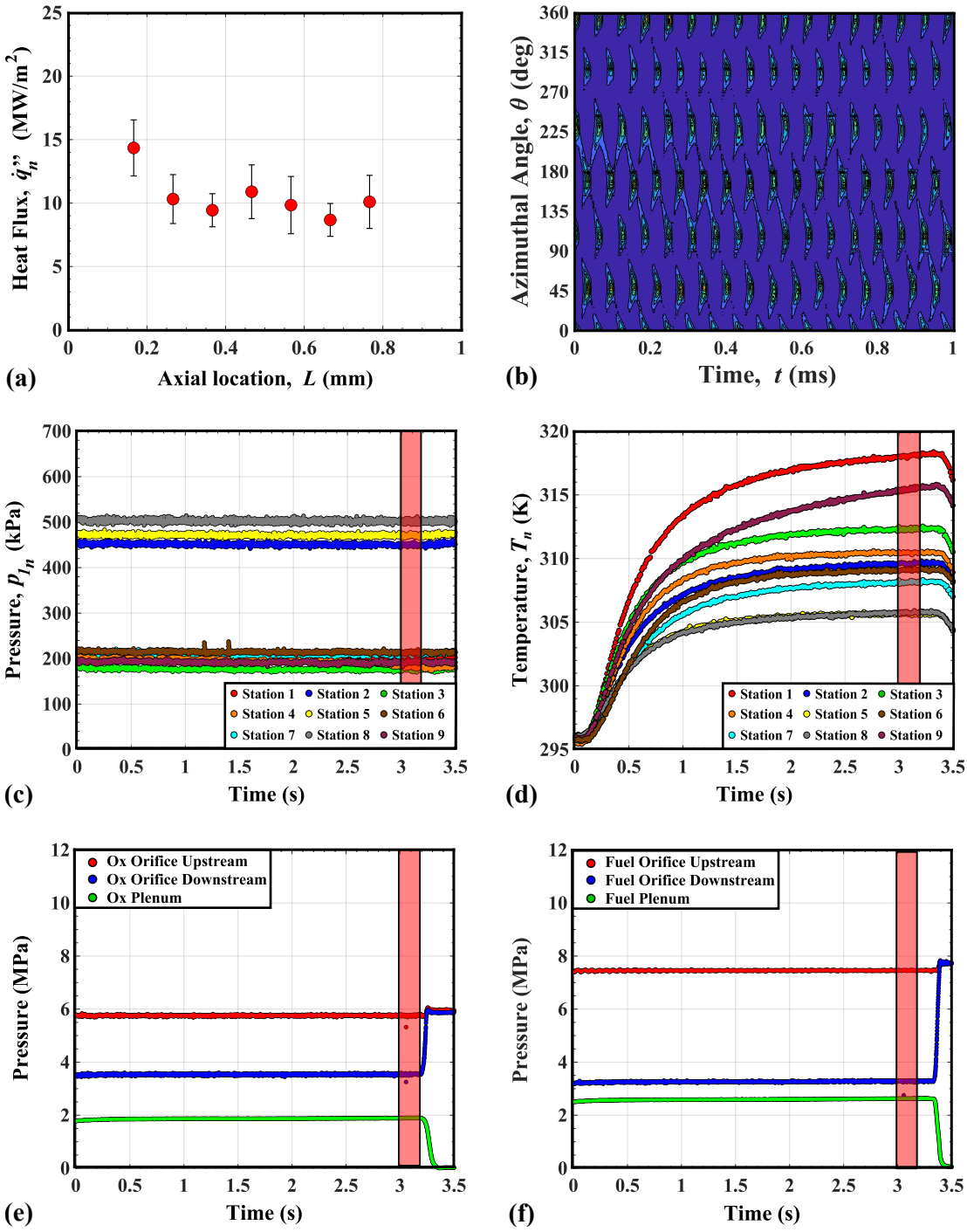


Figure A.6: Test 20241029-015 (a) axial heat flux, (b) thrust, (c) outlet pressure, (d) outlet temperature, (e) oxygen pressures, and (f) fuel pressures.

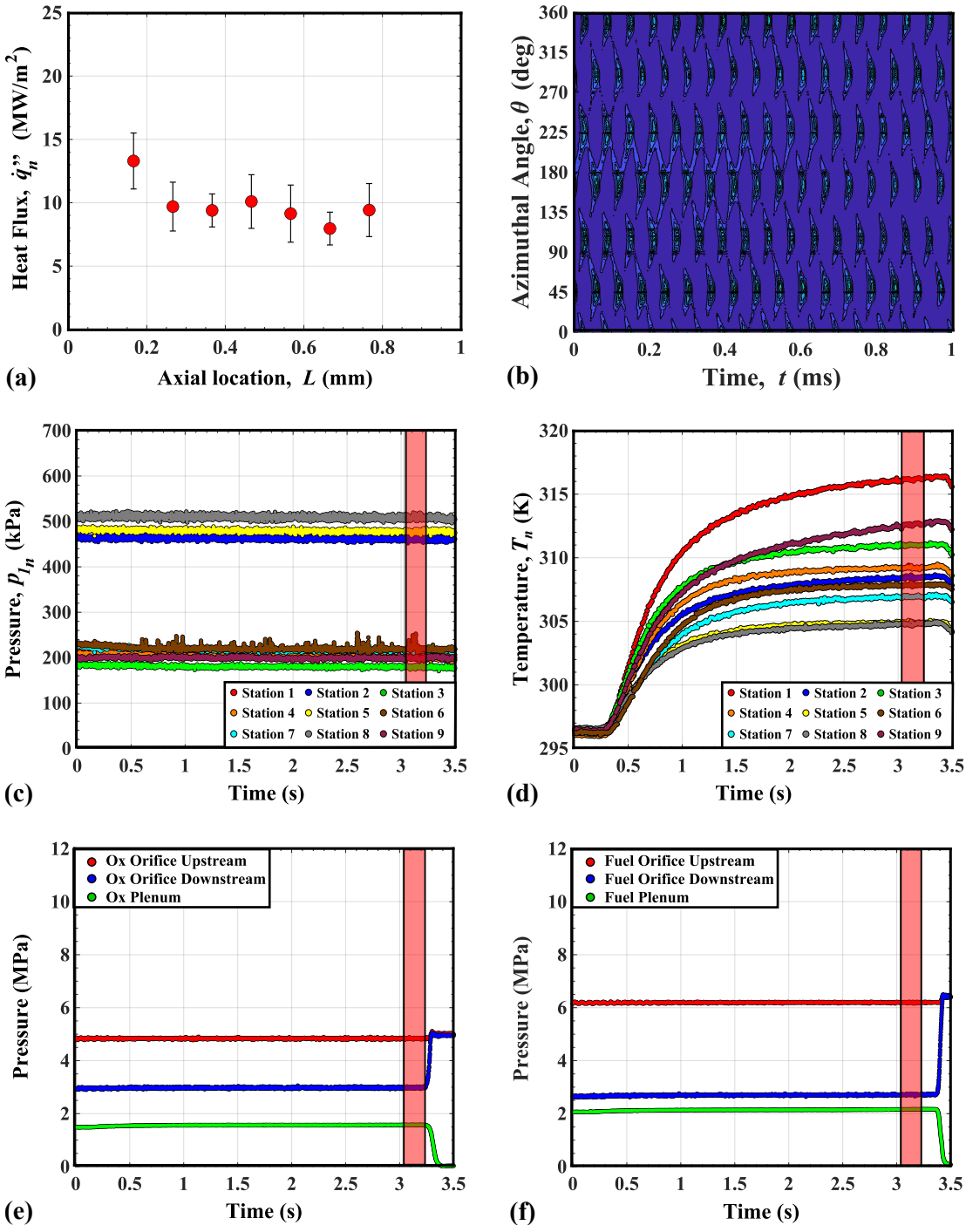


Figure A.7: Test 20241029-016 (a) axial heat flux, (b) thrust, (c) outlet pressure, (d) outlet temperature, (e) oxygen pressures, and (f) fuel pressures.

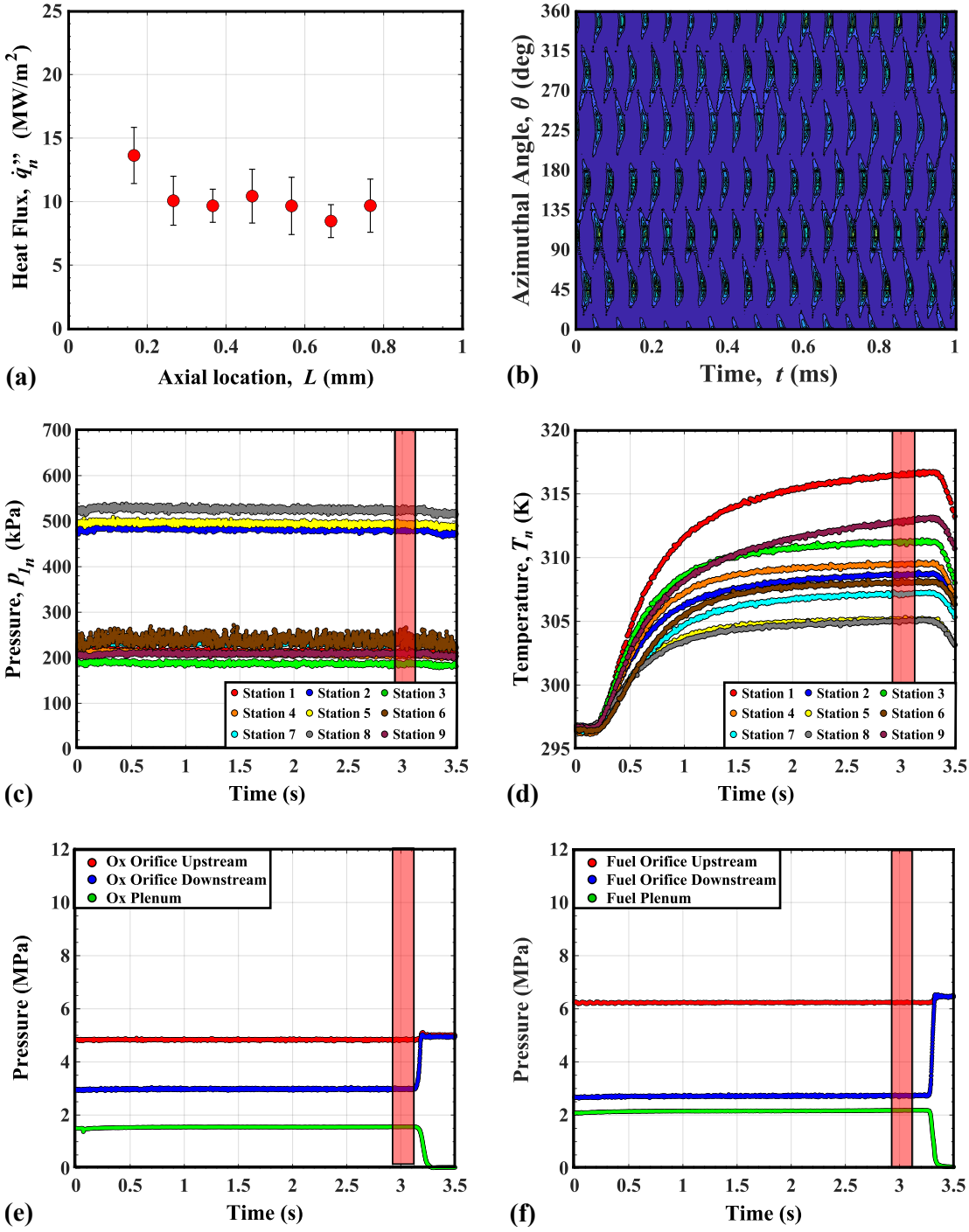


Figure A.8: Test 20241029-017 (a) axial heat flux, (b) thrust, (c) outlet pressure, (d) outlet temperature, (e) oxygen pressures, and (f) fuel pressures.

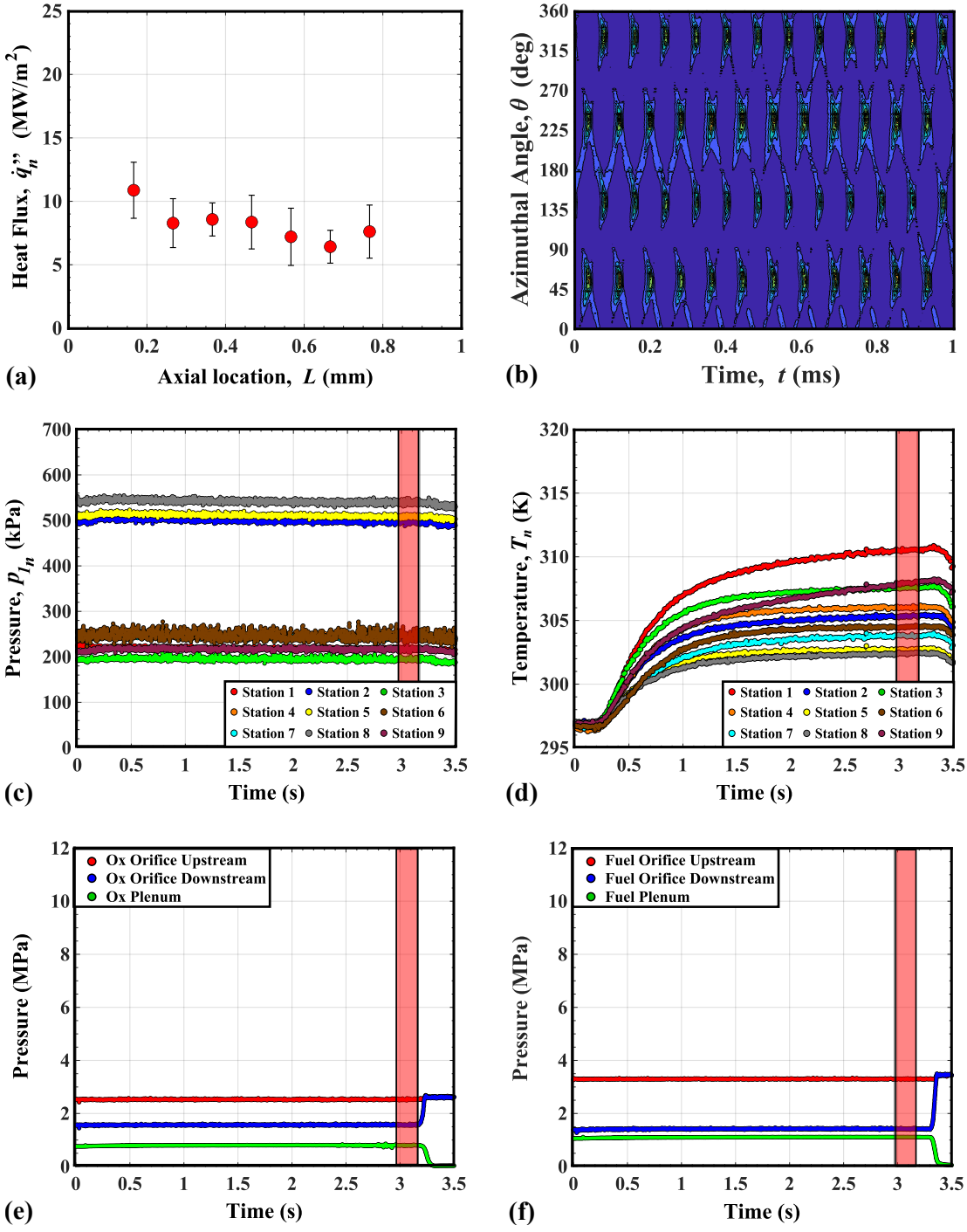


Figure A.9: Test 20241029-018 (a) axial heat flux, (b) thrust, (c) outlet pressure, (d) outlet temperature, (e) oxygen pressures, and (f) fuel pressures.

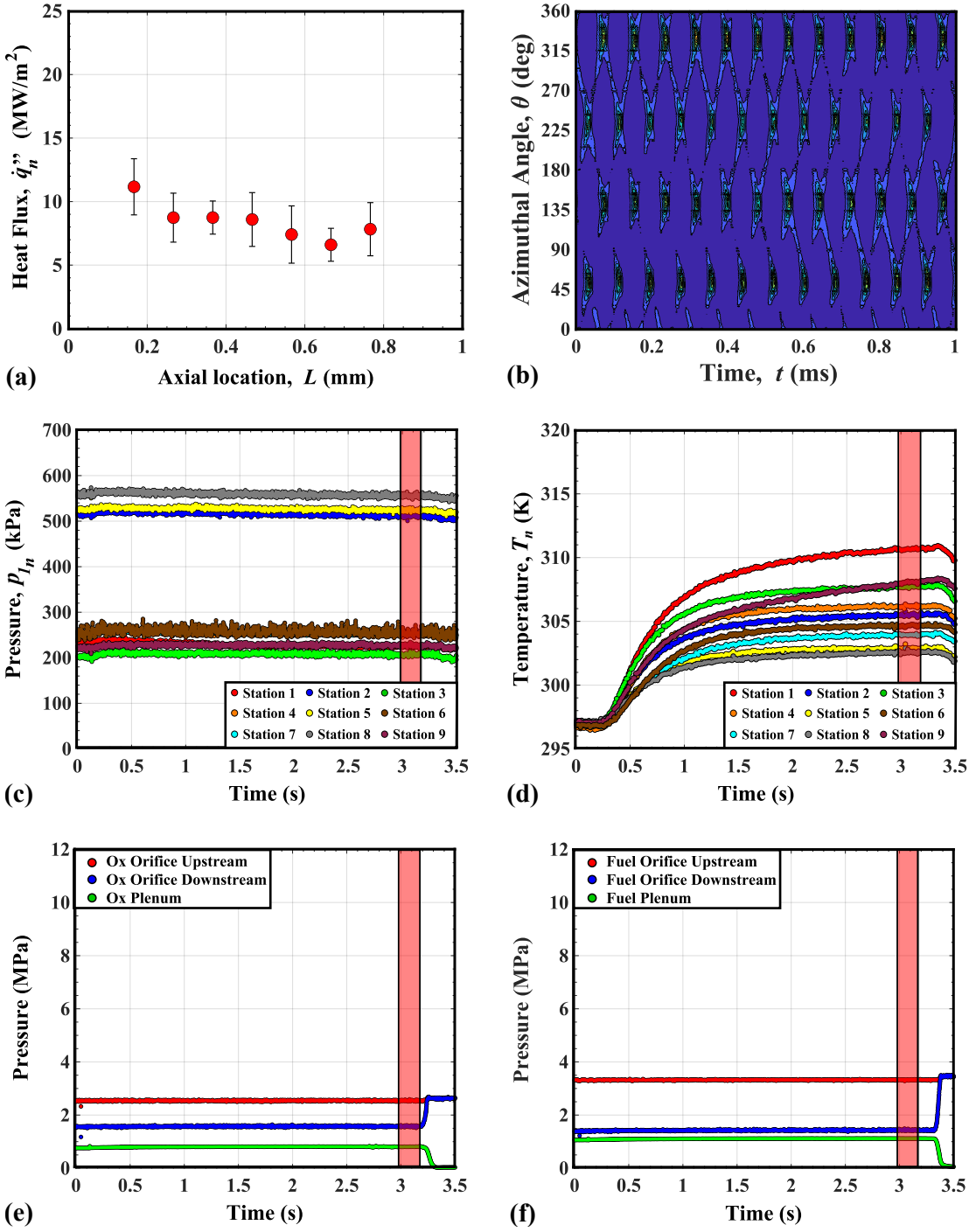


Figure A.10: Test 20241029-019 (a) axial heat flux, (b) thrust, (c) outlet pressure, (d) outlet temperature, (e) oxygen pressures, and (f) fuel pressures.

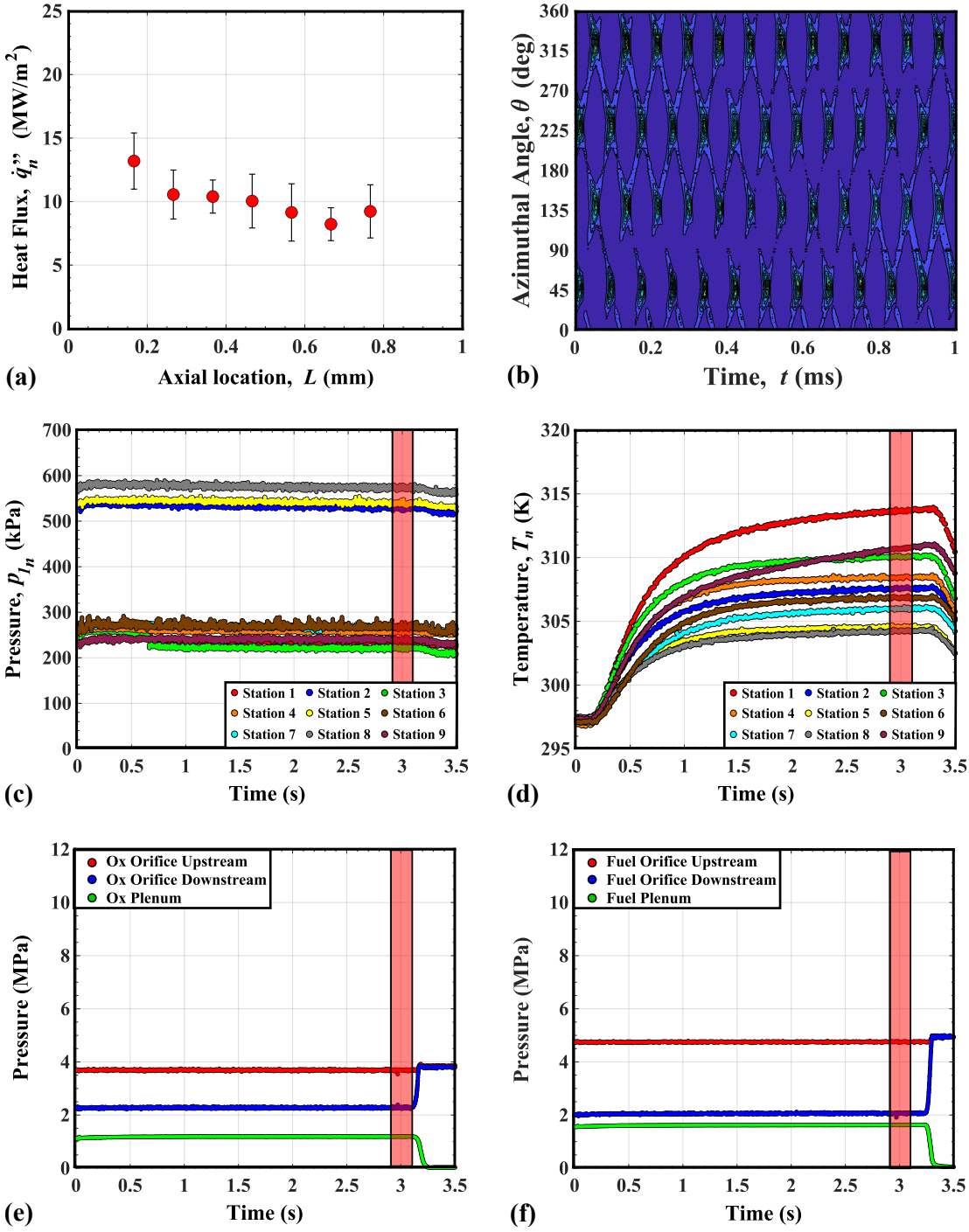


Figure A.11: Test 20241029-020 (a) axial heat flux, (b) thrust, (c) outlet pressure, (d) outlet temperature, (e) oxygen pressures, and (f) fuel pressures.

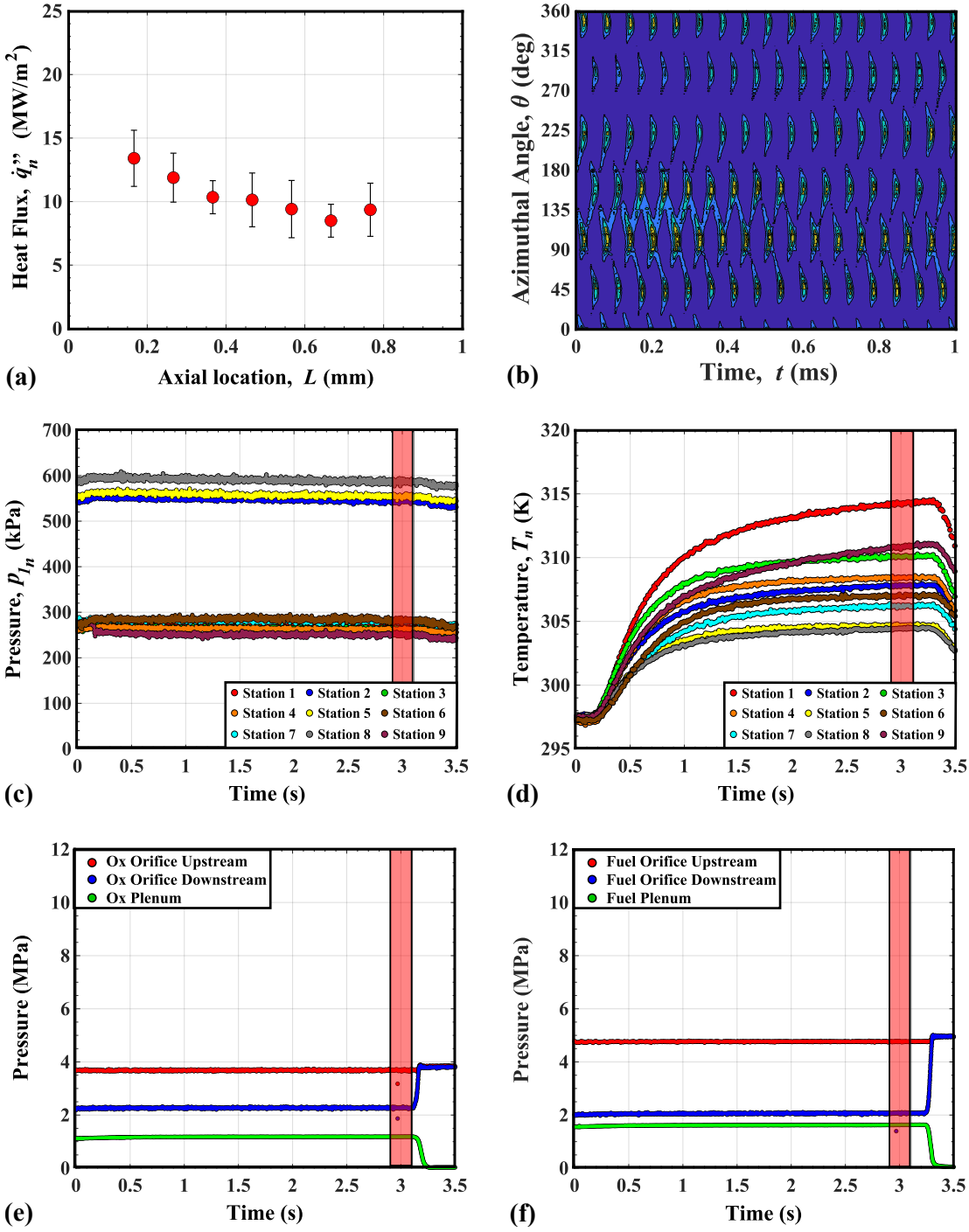


Figure A.12: Test 20241029-021 (a) axial heat flux, (b) thrust, (c) outlet pressure, (d) outlet temperature, (e) oxygen pressures, and (f) fuel pressures.

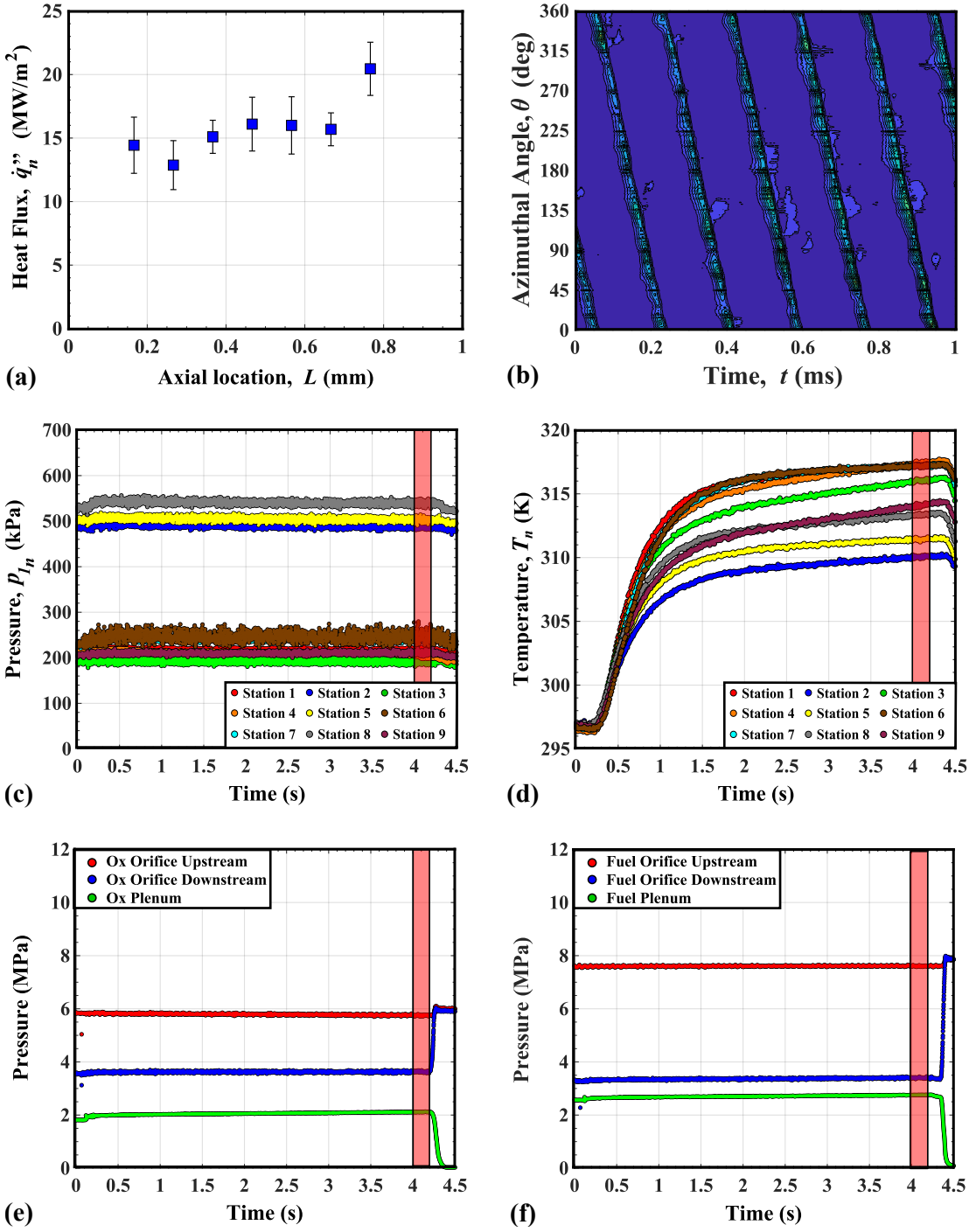


Figure A.13: Test 20241031-005 (a) axial heat flux, (b) thrust, (c) outlet pressure, (d) outlet temperature, (e) oxygen pressures, and (f) fuel pressures.

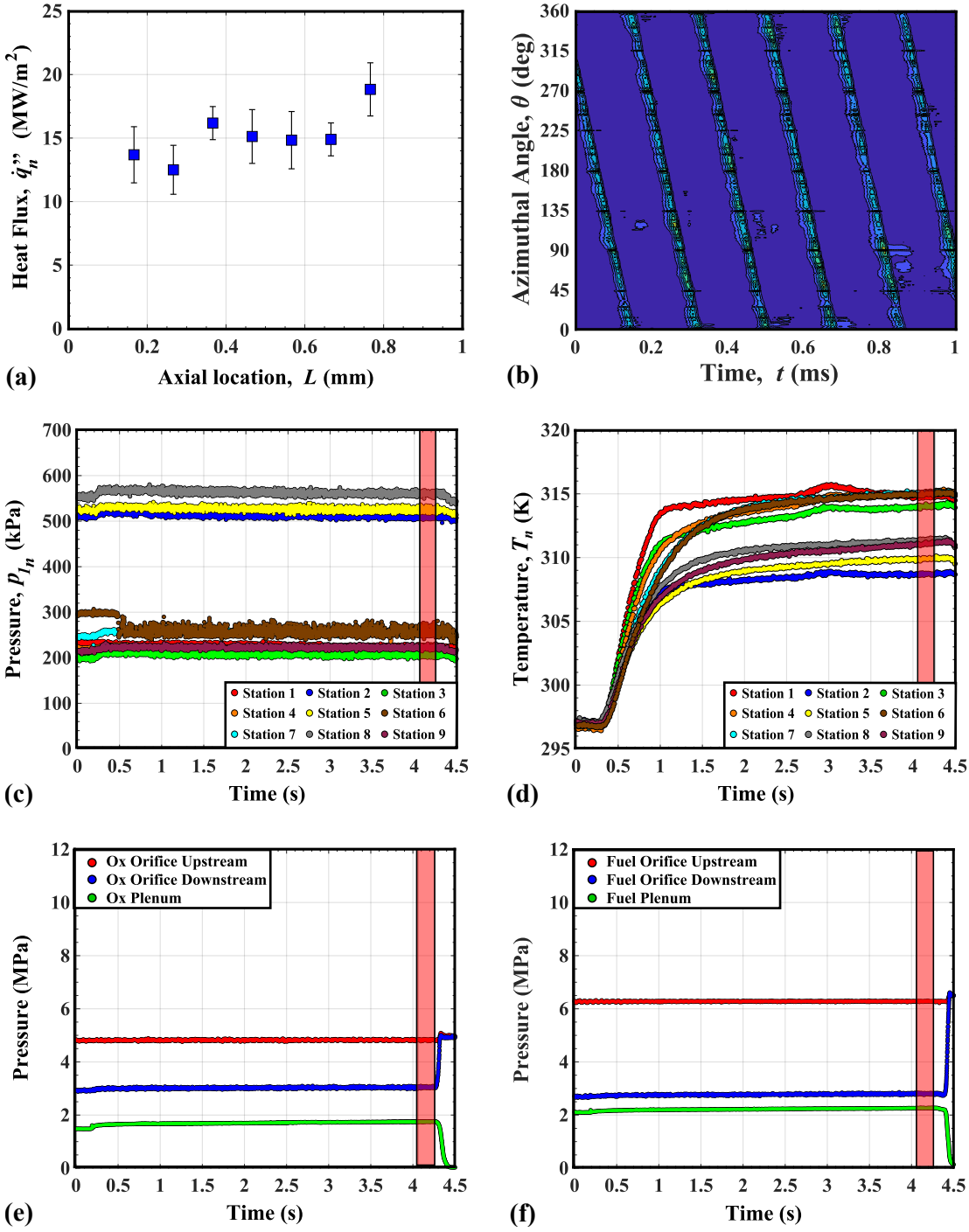


Figure A.14: Test 20241031-006 (a) axial heat flux, (b) thrust, (c) outlet pressure, (d) outlet temperature, (e) oxygen pressures, and (f) fuel pressures.

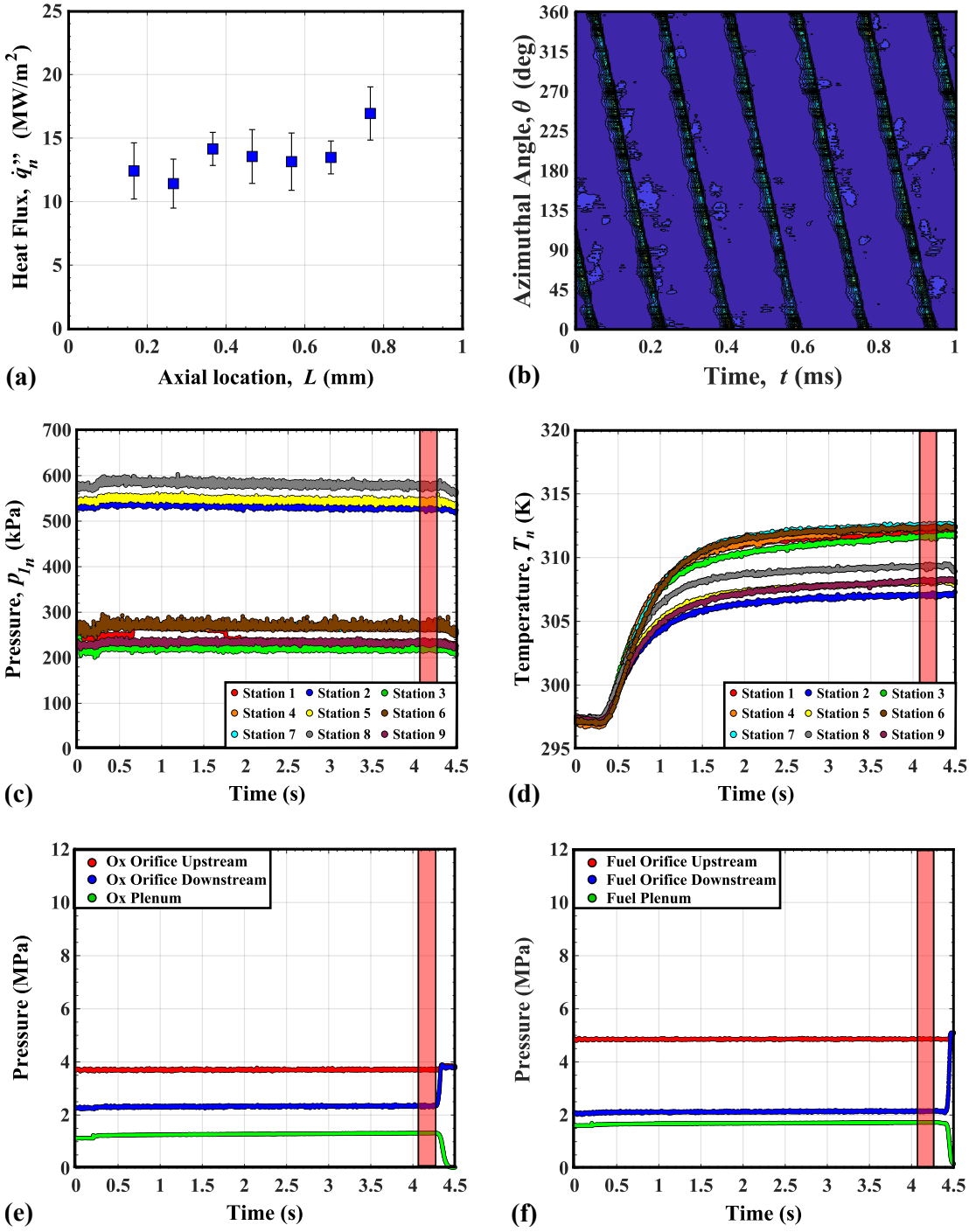


Figure A.15: Test 20241031-007 (a) axial heat flux, (b) thrust, (c) outlet pressure, (d) outlet temperature, (e) oxygen pressures, and (f) fuel pressures.

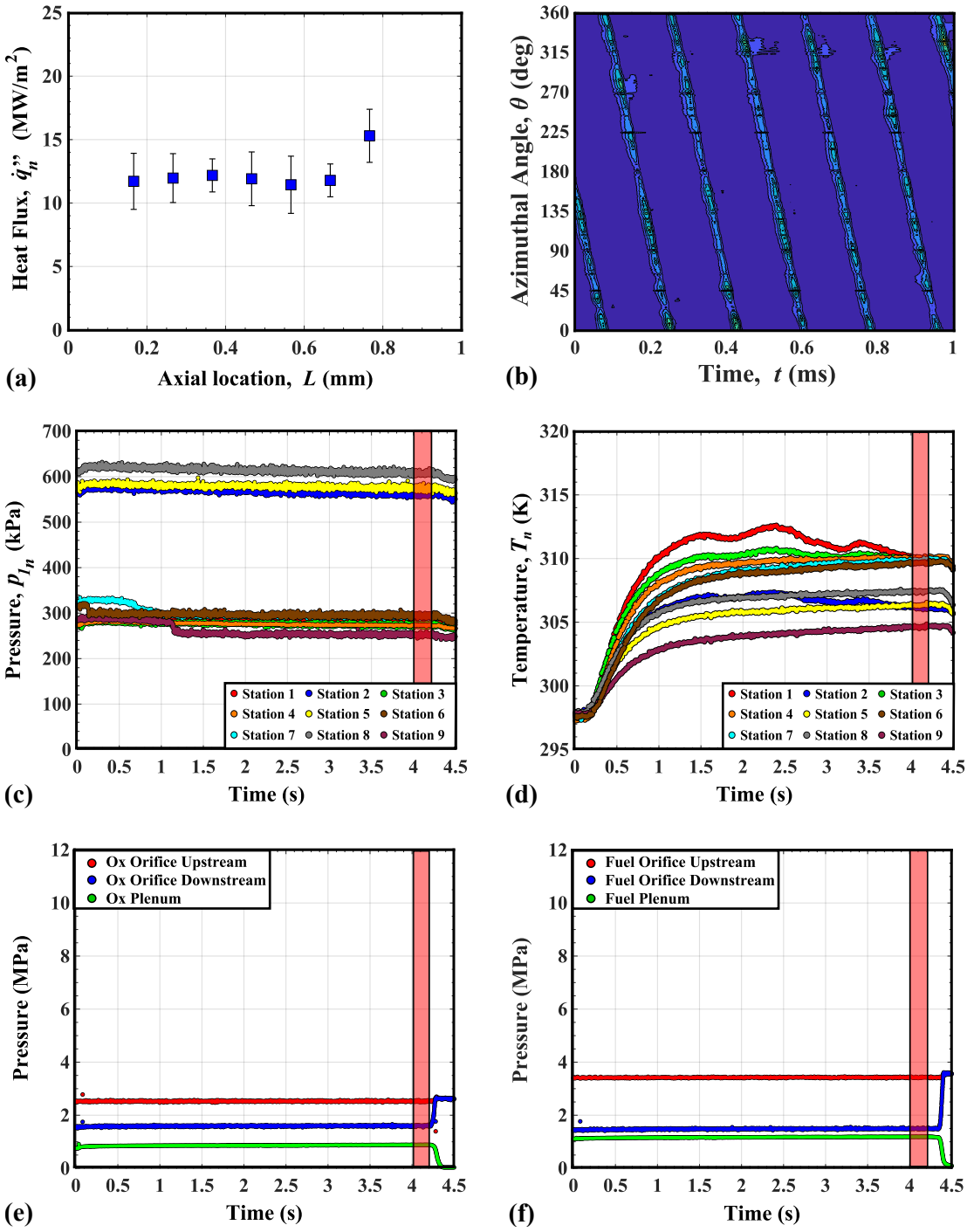


Figure A.16: Test 20241031-009 (a) axial heat flux, (b) thrust, (c) outlet pressure, (d) outlet temperature, (e) oxygen pressures, and (f) fuel pressures.

Appendix B: Heat Flux Varying Mass Flux

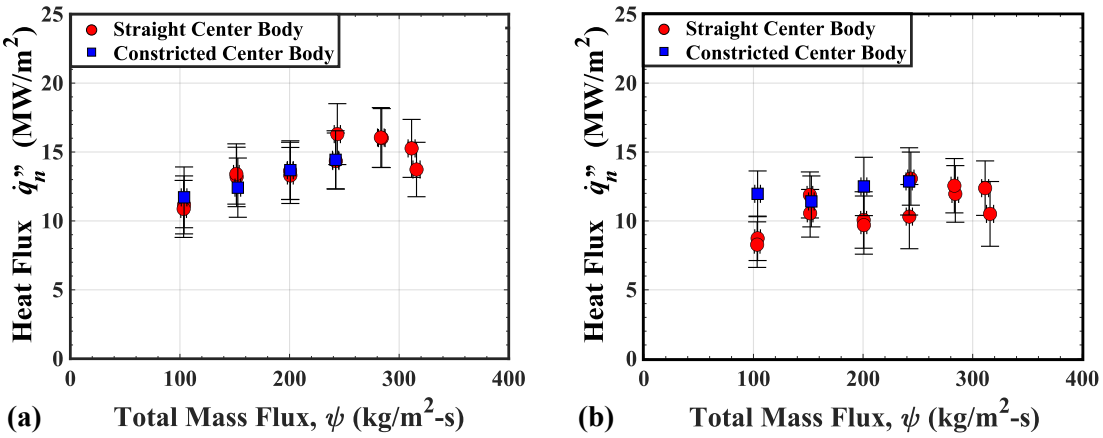


Figure B.17: Heat flux varying mass flux for (a) station 2 and (b) station 3

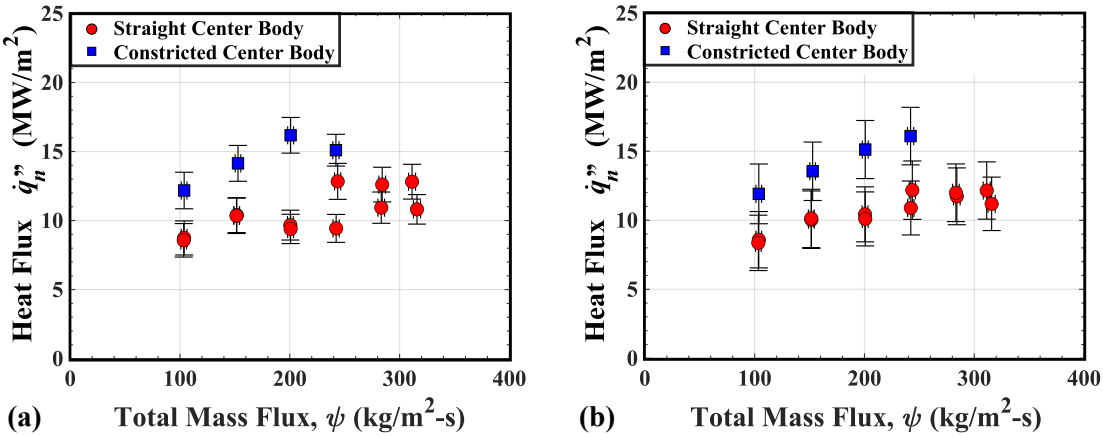


Figure B.18: Heat flux varying mass flux for (a) station 4 and (b) station 5

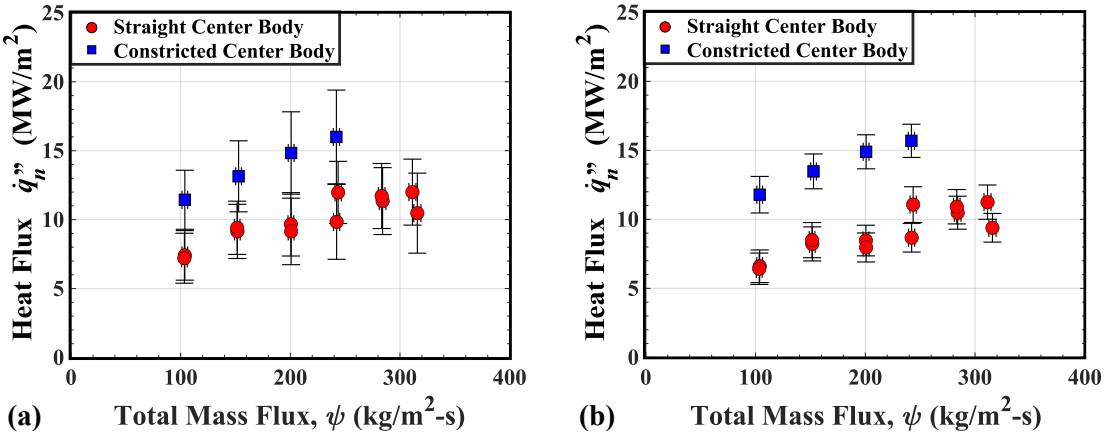


Figure B.19: Heat flux varying mass flux for (a) station 6 and (b) station 7

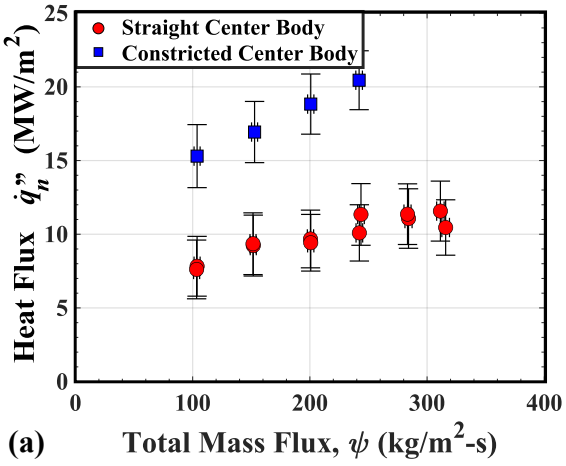


Figure B.20: Heat flux varying mass flux for (a) station 8

Appendix C: Water Flow Calibration Data

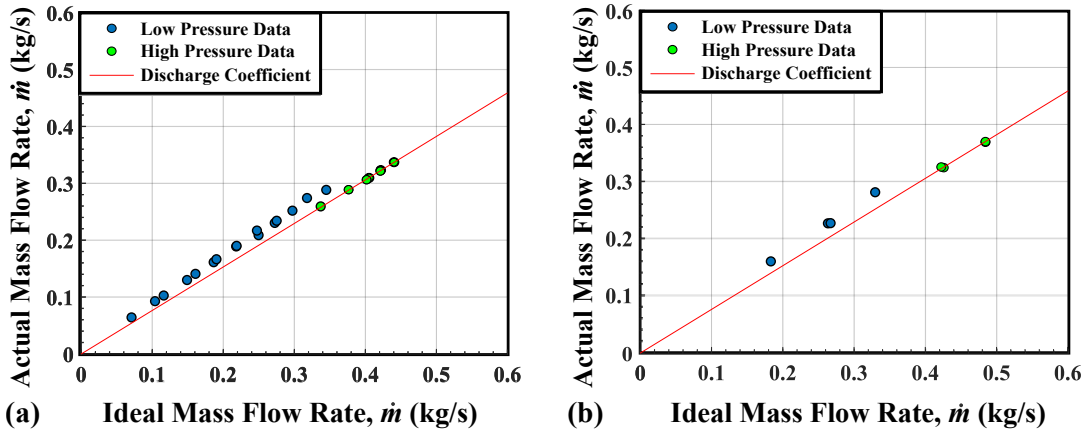


Figure C.21: Water flow calibration data for (a) station 1 and (b) station 2.

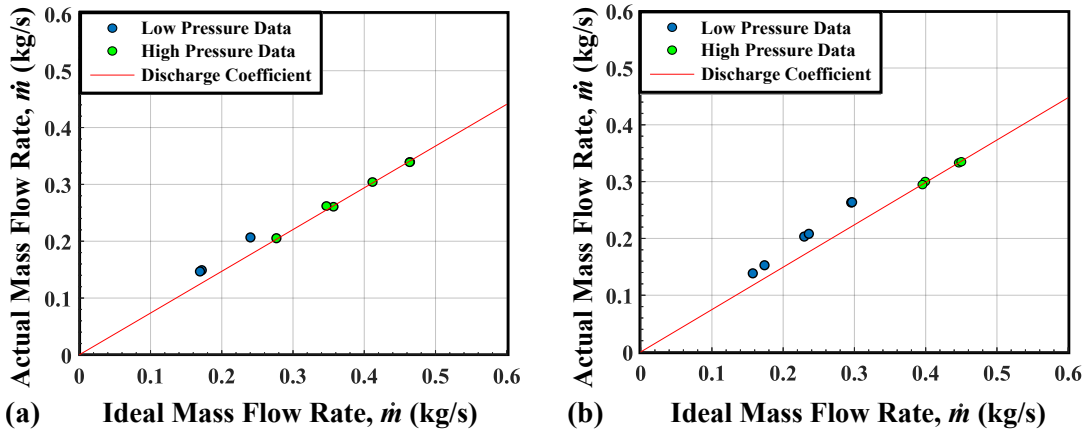


Figure C.22: Water flow calibration data for (a) station 3 and (b) station 4.

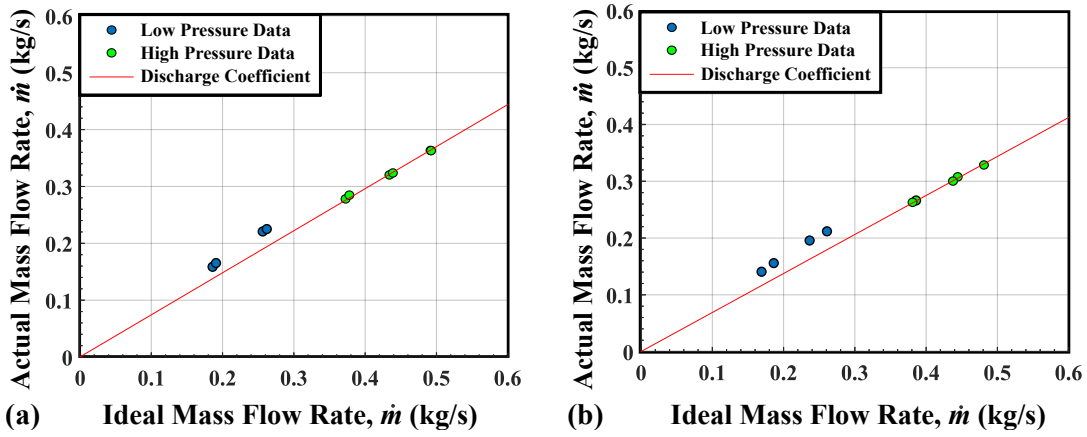


Figure C.23: Water flow calibration data for (a) station 5 and (b) station 6.

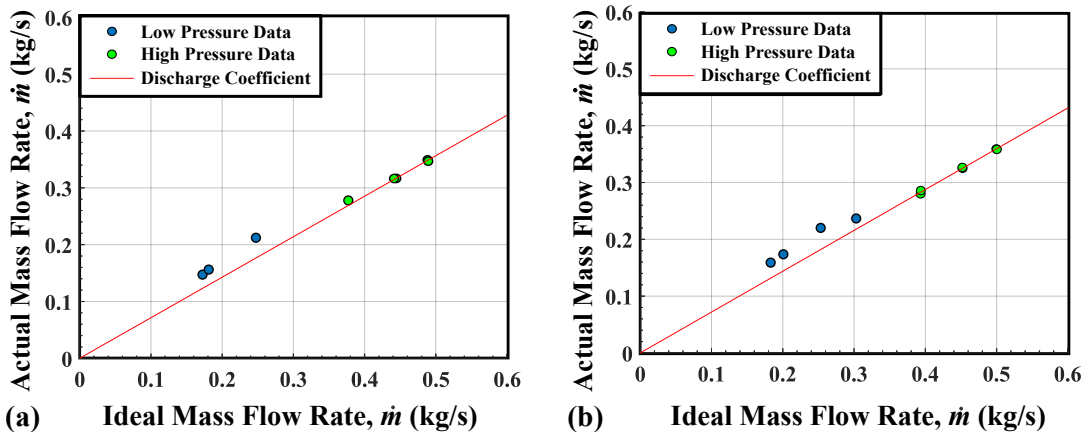


Figure C.24: Water flow calibration data for (a) station 7 and (b) station 8.

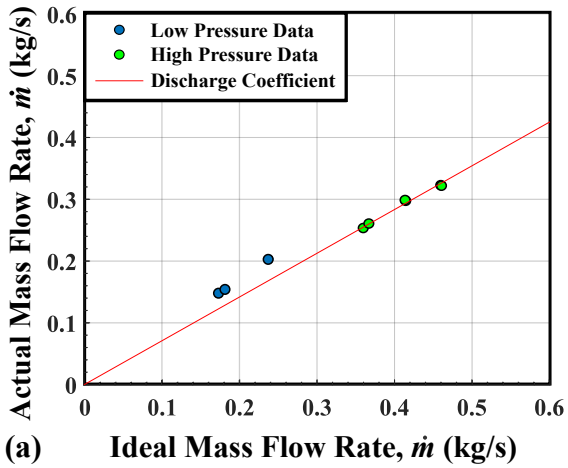


Figure C.25: Water flow calibration data for (a) station 9.

Appendix D: Test Conditions Summary

Table 1: Experimentally Tested Set Conditions

Date	**Test**	**Center Body**	**Ox. $\dot{m}$ (kg/s)**	**Fuel $\dot{m}$ (kg/s)**	**Equivalence Ratio ϕ**	**Total Mass Flux, ψ (kg/s-m^2)**
20241025	012	straight	0.339	0.094	1.105	310.348
20241028	006	straight	0.338	0.093	1.102	309.437
20241028	009	straight	0.306	0.086	1.117	281.017
20241028	010	straight	0.305	0.086	1.127	280.465
20241028	011	straight	0.262	0.074	1.128	241.012
20241029	015	straight	0.259	0.074	1.143	239.278
20241029	016	straight	0.217	0.061	1.118	199.213
20241029	017	straight	0.217	0.061	1.126	199.440
20241029	018	straight	0.112	0.031	1.117	103.073
20241029	019	straight	0.113	0.032	1.120	103.560
20241029	020	straight	0.165	0.046	1.112	151.067
20241029	021	straight	0.164	0.046	1.118	150.805
20241031	005	constricted	0.259	0.076	1.169	240.387
20241031	006	constricted	0.216	0.062	1.138	199.548
20241031	007	constricted	0.165	0.047	1.134	152.373
20241031	009	constricted	0.112	0.033	1.162	103.758